Colossal magnetoresistive manganites for sensing applications

Paolo Perna

Paolo Perna. Colossal magnetoresistive manganites for sensing applications. Condensed Matter [cond-mat]. Université de Caen; Università degli studi di Cassino, 2008. English. NNT : . tel-00262254

HAL Id: tel-00262254
https://theses.hal.science/tel-00262254
Submitted on 11 Mar 2008

Université de Caen / Basse-Normandie
U.F.R. : Sciences Caen
Ecole Doctorale S.I.M.E.M.

Co-tutelle de Thèse
entre
l'Universitè de Caen Basse-Normandie (France)
et
l'Université de Cassino (Italie)
Arrêté du 6 janvier 2005

Thèse
présentée par

Paolo PERNA

le 27 Février 2008
en vue de l'obtention du titre de
Doctorat de l'Université de Caen
Spécialité : Milieux denses, matériaux et composants
Arrêté du 7 août 2006

Colossal magnetoresistive manganites for sensing applications

Manganites à magnétorésistance colossale pour la réalisation de capteurs

MEMBRES du JURY :

M. **Umberto SCOTTI DI UCCIO**, Professeur à l'Université de Cassino (*directeur de thèse*)

Mme **Laurence MECHIN**, Chargée de Recherche CNRS (HDR) à l'Université de Caen (*directrice de thèse*)

M. **Antonello ANDREONE**, Professeur à l'Université Federico II de Naples (*rapporteur*)

M. **Marino MARSI**, Professeur à l'Université Paris-Sud (*rapporteur*)

Università degli Studi di Cassino
Di.M.S.A.T. – Facoltà di Ingegneria
Dottorato di Ricerca in Ingegneria Meccanica
XX ciclo

Université de Caen / Basse-Normandie
U.F.R. de Sciences
Ecole Doctorale S.I.M.E.M.
Laboratoire GREYC - ENSICAEN

Colossal magnetoresistive manganites for sensing applications

Doctoral Thesis

by

Paolo PERNA

October 2007

Introduction

The 2007 Nobel Prize in Physics was awarded to A. Fert and P. Grünberg, who discovered in 1988 the giant magnetoresisance effect in ferromagnetic multilayers (A. Fert *et al.*, *Phys. Rev. Lett.* 61, 2472 (1988), P. Grünberg *et al.*, *Phys. Rev. B* 39, 4828 (1989)), opening the way to a new technology, that is *spintronics*, i.e. spin-electronics. As the name indicates, the spintronics is based on the concept that information can be carried not only by the charge, that is by electric current, but also by the spins of electrons.

While spintronics devices are currently employed in conventional electronics (magnetoresistive heads readers of hard disks, magnetic random access memories, etc.), the potentiality of the field is not yet fully exploited and there is room for both fundamental and applicative investigation. In this context, one of the main fields of activity is the search for new materials with smart properties. Together with a few other compounds, the ferromagnetic perovskitic manganites appear as promising candidates.

The perovskitic manganites raised the interest of the scientific community when the colossal magnetoresistance was discovered in thin films. This effect consists in a spectacular reduction of the electric resistance when a magnetic field is applied. Unfortunately, this only happens at high fields, so that the hope to take advantage of the colossal magnetoresistance in devices was soon frustrated. However, the manganites possess other interesting features. In this thesis, I mainly focused on the following:

1. the possible integration of perovskites both in conventional Si-based electronics, and in innovative full-oxide electronics, resorting to the technology of epitaxial film growth
2. the manganites have a steep variation of resistivity at the Curie temperature. This may point to possible applications as temperature sensors or bolometers;
3. the manganites are excellent half metals, that is the free electrons are almost completely spin polarized; this is essential when trying to feed a spin polarized current in most spintronics devices.

In this context, my experimental work was devoted to the study of the $La_{0.7}Sr_{0.3}MnO_3$ ($LSMO$) manganite, that is robust ferromagnet, showing the highest Curie temperature among manganites. I will try to demonstrate that $LSMO$ is actually suitable for applications. This is based on the full control of the growth process of epitaxial films, that I achieved resorting to different deposition techniques (sputtering, laser ablation, laser ablation assisted by $RHEED$, that is high energy electron diffraction), on the investigation of the physical properties of the deposited films and multilayers, and on the demonstration of functionality of prototype devices. This work required the joint application of many different experimental techniques, and it was only possible due to the cooperation between the two Institutions that granted this PhD, namely the University of Cassino, Italy and the $GREYC$ laboratory at the University of Caen / Basse Normandie, France, and of the CNR / $INFM$ *Coherentia* laboratory of Napoli, Italy.

The remaining part of the manuscript is divided as follows. Chaps. 1, 2 are devoted to some introductory remarks on materials and applications, respectively. The other chapters report the results of the set of experiments that I realized:

— in Chap. 3, I focus on the fabrication of $LSMO$ films with the quoted techniques, to the basic characterization of samples (also achieved resorting to advanced investigation techniques) and to the comparison between material properties of the samples, trying to demonstrate to what extent each technique successfully provides high quality samples;

- in Chap. 4, I report on the fabrication and characterization of two sets of multilayer structures that were designed in Caen to achieve crystalline *LSMO* growth on *Si* substrates, with the aim of indicating the best route to the fabrication of films for application to room temperature bolometers;
- the Chap. 5 is devoted to fundamental material science investigations, regarding the transport and magnetic properties of *LSMO* films;
- finally, the fabrication technique and the characterization of prototype spintronics devices based on *LSMO* is discussed in Chap. 6.

The Appendix contains the detailed structural data as determined by x-ray diffraction performed on several samples.

Many achronims are employed in the text. A comprehensive list is at page 7.

Contents

Used abbreviations & symbols

MIT	Metal Insulator Transition
LSMO	$La_{1-x}Sr_xMnO_3$, $La_{0.7}Sr_{0.3}MnO_3$
CMR	Colossal magnetoresistance
JT	Jahn Teller
STO	$SrTiO_3$
LAO	$LaAlO_3$
DOS	Density of States
DE	Double Exchange
T_C	Curie temperature
P	Paramagnetic, Parallel
I	Insulating, Insulator
AFM	Antiferromagnetic metalllic, Atomic Force Microscopy
FM	Ferromagnetic metallic, Ferromagnet
PM	Paramagnetic metallic
PI	Paramagnetic insulating
M	Metallic, Metal
M_S	Saturation magnetization
λ	Magnetostrictive constant
Py	Permalloy ($Ni_{0.80}Fe_{0.20}$)
DW	Domain Wall
H_S	Saturation field
H_C	Coercive field
GB	Grain Boundary
SW	Stoner-Wohlfarth (model)
MR	Magneto Resistance
AMR	Anisotropic magnetoresistance
PS	Phase Separation
ε_B	bulk strain
$\varepsilon*$	biaxial strain
LCMO	$La_{0.7}Ca_{0.3}MnO_3$
NGO	$NdGaO_3$
θ_{vic}	vicinal angle
TCR	Temperature Coefficient of Resistivity
YBCO	$YBa_2Cu_3O_7$
NEP	Noise Equivalent Power
α_H/n	Normalized Hooge parameter
GMR	Giant magnetoresistance
CIP	Current in-plane
CPP	Current perpendicular to plane
AP	Anti-Parallel
MTJ	Magnetic Tunnel Junction
TMR	Tunnel magnetoresistance
LWMR	Low Field magnetoresistance
PLD	Pulsed Laser Deposition
M.O.D.A.	Modular facility for the Oxides Deposition and Analysis

HP-RHEED	High Pressure Reflection High Energy Electron Diffraction
UHV	Ultra High Vacuum
XRD	X-Ray Diffraction
XPS	X-ray Photoemitted Spectroscopy
SPA-LEED	Scan Profile Analyzer Low Energy Electron Diffraction
SPM	Scanning Probe Microscopy
RBS	Rutherford Back Scattering
FWHM	Full width at half maximum
STM	Scanning Tunnel Micoscopy
T_P	Maximum resistivity temperature
T_{MI}	Metal Insulator Transition temperature
ZFC	Zero Field Cooled
RMS	root-mean-square (roughness)
HR-TEM	High Resolution Trasmission Electron Microscopy
RSM	Reciprocal Space Mapping
YSZ	Yttria-Stabilized-Zirconia
BTO	$Bi_4Ti_3O_{12}$
BTO-based	$BTO/CeO_2/YSZ/Si$
STO-based	$STO/CeO_2/YSZ/Si$
EDS	Electron Dispersive Spectroscopy
FPT	Ferromagnetic Paramagnetic Transition
HFM	Half ferromagnetic metal
el-el	electron-electron
el-ph	electron-phonon
STS	Scanning Tunnel Spectroscopy
MOKE	Magneto optical Kerr effect
SEM	Scanning Electron Microscopy

Chapter 1

Colossal magnetoresistive manganites

The perovskitic manganese oxides exhibiting a *Metal-Insulator Transition* (*MIT*) accompanied by *magnetoresistive* effects soon raised the interest of the scientific community because of their potential technological applications. In particular, in the $La_{0.7}Sr_{0.3}MnO_3$ (*LSMO*), the sharp drop of the electric resistance around room temperature together with the occurrence of a metallic phase with a fully spin-polarized conduction band are very promising for temperature and field sensors, non-volatile memories and magnetic read-heads [1, 2, 3, 4, 5, 6].

In this chapter, I report on the structural, transport and magnetic properties of the manganite films, referring in particular to the *LSMO* compound. The aim is to fix here the phenomenological basis on the *LSMO* properties, in order to discuss later on the devices based on high quality *LSMO* films.

1.1. Perovskitic structure

The colossal magnetoresistive (*CMR*) manganites have the perovskitic structure. The general formula was identified by Jonker and van Santen [7] as ABO_3, where A is a trivalent rare earth (La, Pr, Nd) ion and B is a trivalent Mn ion. The susbtitution of the rare earth with a divalent alkaline (Sr, Ca, Ba) ion (*doping*) determines a mixed valence $Mn^{3+} - Mn^{4+}$ state. Fig.1.1 illustrates the structure of a *LSMO* compound, where the trivalent La^{3+}_{1-x} and divalent Sr^{2+}_x ions are located at the corners of the unit perovskite cell (A site), the oxygen ions occupy the center of the faces in the unit cell, and the smallest Mn^{3+}_{1-x} and Mn^{4+}_x ions are in the center of the octahedral oxygen ions (B site).

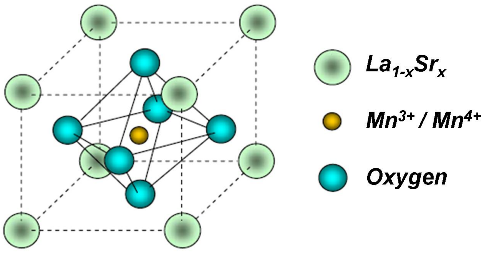

Figure 1.1. Perovskitic structure of the $La_{1-x}Sr_xMnO_3$ compound.

The properties of the manganites are governed by the *tolerance factor* [8]

$$t = \frac{r_{La,Sr} + r_O}{\sqrt{2}\,(r_{Mn} + r_O)} \tag{1.1}$$

that takes into account the average ionic radii ($r_{La,Sr}$, r_O and r_{Mn}) of the species. The perovskite structure is stable for $0.89 < t < 1.02$ [8], while $t = 1$ corresponds to the perfect cubic closely packed structure. In the manganites, t differs appreciably from 1 leading to the rearrangment of the cells in rhombohedral or orthorhombic structures of lower simmetry, as illustrated in Fig. 1.2. At the microscopic level, the distortion of the cubic cells comes with the deformation of the oxygen octahedra around the Mn ions (*Jahn Teller* (JT) *effect*). In the *LSMO*, the Mn^{3+} ions show a noticeable JT distortion, while the Mn^{4+} sites do not [9, 10].

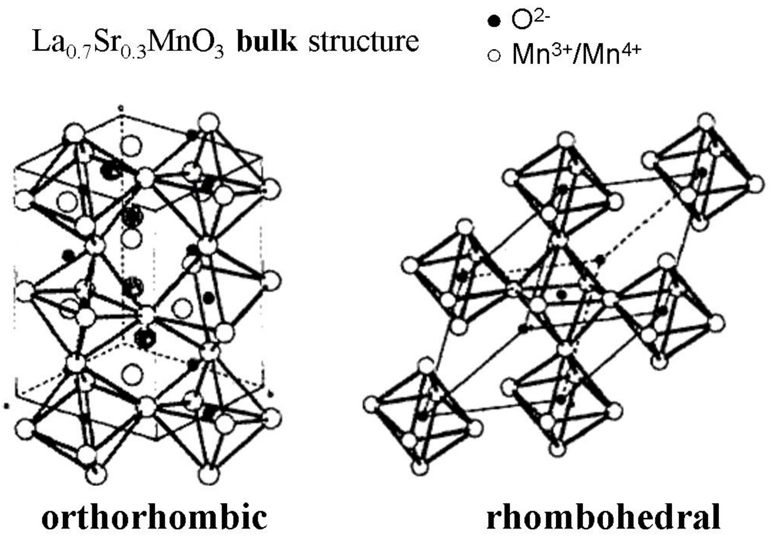

Figure 1.2. Orthorhombic and rhombohedral structures of $La_{1-x}Sr_xMnO_3$ bulk.

1.1.1. Strain effects in films

When the manganite is prepared as an *epitaxial* film (i.e. the deposited film takes on a lattice structure and orientation identical to those of the substrate), its crystallographic structure can differ from that of the parent bulk, often assuming a tetragonal or a pseudo-cubic structure. This is due to the biaxial stress determined by the substrate that results in a strained film structure. The stress affects many physical properties of the manganties, so that the choice of the substrate is very relevant. It is widely accepted (see for a review paper [11]) that epitaxial *LSMO* shows optimal properties when grown on single crystal perovskites, such as $SrTiO_3$ (STO) and $LaAlO_3$ (LAO), mainly because of the small *lattice mismatch* (δ). δ is defined as follows:

$$\delta = \frac{a_{Substrate} - a_{Film}}{a_{Substrate}} \tag{1.2}$$

where $a_{Substrate}$ and a_{Film} are the lattice parameters. The STO has a cubic cell with $a_{STO} = 0.3905nm$, while the LAO cell is pseudo-cubic with $a_{LAO} = 0.3793nm$. The lattice mismatches with *LSMO* for these two substrates result $\delta_{LSMO-STO} = +0.8\%$ and $\delta_{LSMO-LAO} = -2.1\%$, that is the STO applies a tensile stress while the LAO a compressive stress to the *LSMO* cell (Fig. 1.3).

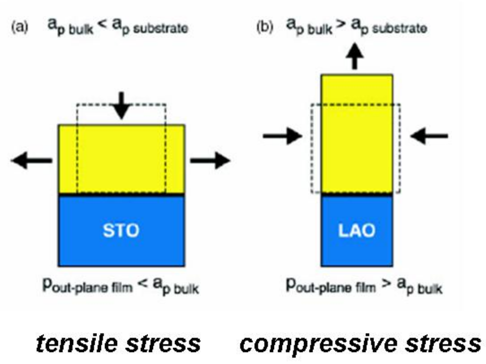

Figure 1.3. Schematic of the *film-substrate mismatch*, in the case of *tensile* strain *(a)* and *compressive* strain *(b)*, induced by the (001)-oriented *STO* and *LAO* single crystal substrates, respectively (after [11]).

In order to study the deformations of *LSMO* we can consider the *stress-strain* realations. The stress tensor is defined as follows:

$$\sigma = (\Omega_{ij}) \cdot \epsilon_{ij} \tag{1.3}$$

where ϵ_{ij} is the strain tensor and (Ω_{ij}) are the strain components, that are measured in Pa. The (Ω_{ij}) for *LSMO* are found in [12]. The *in-plane* and the *out-of-plane* strain components of the strain tensor are defined as follows:

$$\varepsilon_{[100]} = \frac{c_{[100]} - c^0_{[100]}}{c^0_{[100]}} \tag{1.4}$$

$$\varepsilon_{[001]} = \frac{c_{[001]} - c^0_{[001]}}{c^0_{[001]}} \tag{1.5}$$

where $c^0_{[100]} = c^0_{[001]} = 0.3873nm$ is the unstrained *LSMO* bulk lattice parameter.

In Fig. 1.4 I show a sketch illustrating the main features of the deformations which the *LSMO* unit cell undergoes when epitaxially grown on (110) *STO* . The *LSMO* cell matches its diagonal (along the $[1\bar{1}0]$ crsytallographic direction) and one side (along the [001]) with the respective diagonal and side of *STO* (Fig. 1.4*(b)*). This stress mechanism leds to *in-plane* anisotropy because the two *in-plane* axes are differently strained by the substrate, in contrast to what happens in the case of the (001) growth orientation where the two in-plane axes, (100) and (010), are equivalent (Fig. 1.4*(a)*).

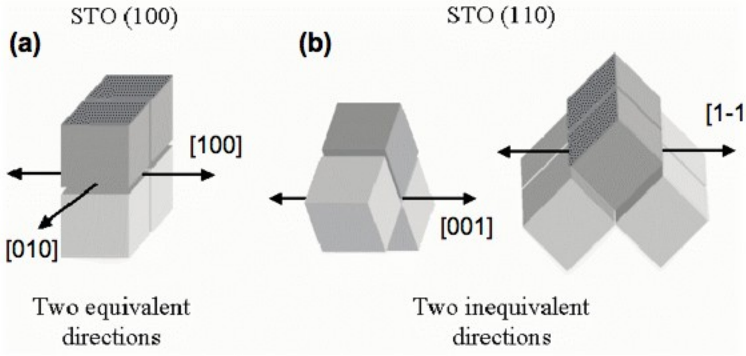

Figure 1.4. The different deformations the *LSMO* unit cell undergoes when growing epitaxially on *STO* (110). The mechanism for matching the substrate lattice parameter is shown for *STO* (001) *(a)* and for *STO* (110) *(b).*

1.2. Electronic structure and spin polarized transport

In an isolated $3d$ manganese ion, five degenerated orbital states are available to the $3d$ electrons (Fig. 1.5). The five $3d$ orbitals are splitted by the cubic crystal field into three t_{2g} orbitals and two e_g orbitals. In the MnO_6 octahedron, the splitting between the lowest t_{2g} level and the highest e_g level is $\Delta \sim 1.5eV$. The intraatomic correlations ensure parallel alignment of the electron spins of the Mn^{3+} and Mn^{4+} ions (*first Hund's rule*); the corresponding exchange energy of about $2.5eV$ being larger than the crystal field splitting Δ. Mn^{3+} is $3d^4$, $t_{2g}^{3\uparrow}e_g^{\uparrow}$ with $S = 2$ whereas Mn^{4+} is $3d^3$, $t_{2g}^{3\uparrow}e_g^0$ with $S = 3/2$. Neglecting the small orbital contribution, their respective magnetic moments are $\sim 4\mu_B$ and $\sim 3\mu_B$.

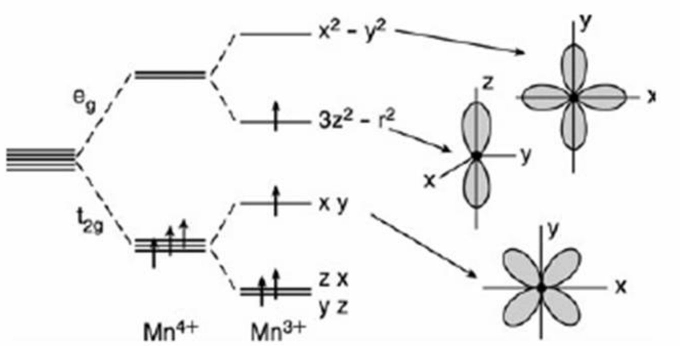

Figure 1.5. Field splitting of the atomic $3d$ levels into lower t_{2g} and higher e_g levels of a Mn ion.

The electrons on the t_{2g} levels do not partecipate in the transport process because strongly localized [13]. Thus, the system consists of a core state with total spin $S = 3/2$ plus an electron per Mn^{3+} site on the e_g orbital involved in the conduction process [14].

Most importantly for an innovative technology, *LSMO* is an almost perfect *half metal*, that is, the conduction band is mostly filled up with one orientation of spin (see Fig. 1.6), opening the door to application of spin injection [3, 6]. Being $N_\uparrow(E_F)$ and $N_\downarrow(E_F)$ the *spin-up* and *spin-down* density, the spin polarization is defined as:

$$P = \frac{N_\uparrow(E_F) - N_\downarrow(E_F)}{N_\uparrow(E_F) + N_\downarrow(E_F)} \tag{1.6}$$

Although *spin-polarized* transport naturally occurs in any material presenting an imbalance of the spin populations at the Fermi level, the spin polarization is generally far from the value $P \sim 1$ that is achieved in *LSMO*.

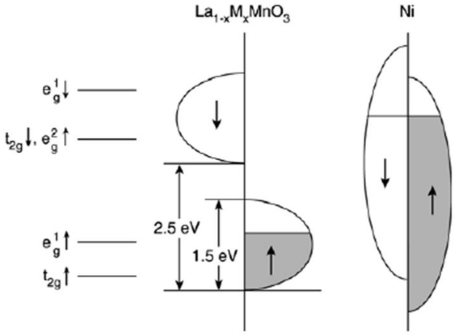

Figure 1.6. Schematic representation of *DOS* of an $La_{1-x}M_xMO_3$ half-metal (*left*) and of a *Ni* ferromagnetic metal (*right*) (after [11]).

The charge transport of the electrons can be described as the ***hopping*** of a conduction electron into a *Mn* site only: $Mn^{3+}_{1\uparrow}O^{-2}_{2\uparrow,3\downarrow}Mn^{4+} \longrightarrow Mn^{4+}O^{-2}_{1\uparrow,3\downarrow}Mn^{3+}_{2\uparrow}$ where 1, 2 and 3 label electrons that belong either to the oxygen between manganese or to the e_g level of the *Mn* ions. As illustrated in Fig.1.7, there are two simultaneous motions (hence the name ***double exchange*** (*DE*)) involving electron 2 moving from the oxygen to the right *Mn* ion and electron 1 from the left *Mn* ion to the oxygen. Since the hopping integral between sites i and j of an electron is $t_{ij}cos(\theta_{ij}/2)$ [15, 16, 17, 18], where θ_{ij} is the angle between the spins S_i and S_j, the itinerant electron spin must always be parallel to the local spin on each site. Thus, a conduction electron can only hop onto a site with its spin parallel to the local moment at that site. If the average number of conduction electrons per site is $n < 1$, the double occupation of a site is strongly suppressed. The system is therefore a *strongly correlated electron system.* For $n = 1$ the system is a *Mott insulator.*

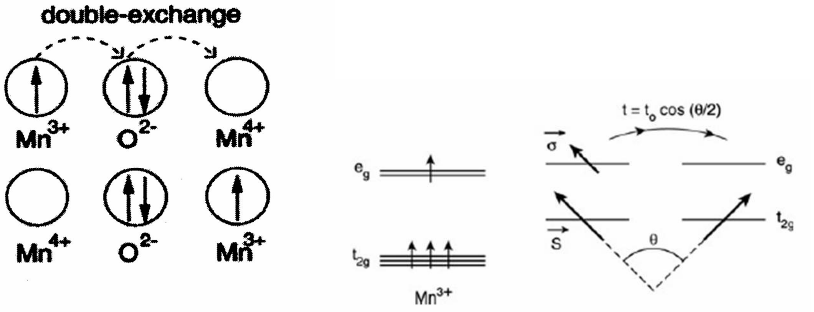

Figure 1.7. Sketch of the *DE* mechanism which involves two *Mn* ions and one *O* ion (*left*). Mobility of e_g-electrons improves if the localized spins are polarized (*right*).

1.3. Metal-Insulator Transition

The doping x in *LSMO* manganite controls the number of carriers, actually holes, at the Fermi level. At the optimal doping ($x = 0.3$) the *LSMO* is a robust ferromagnet with Curie temperature T_C well above room temperature. It exhibits a transition from the high temperature paramagnetic (P) semi-conducting or insulating (I) phase to the low temperature ferromagnetic metallic (FM) phase. The phase diagram of the $La_{1-x}Sr_xMnO_3$ compound is shown in Fig. 1.8 [19]. In the P phase, the electrical resistivity exhibits a strong temperature dependence. For $x < 0.3$ $LSMO$ is insulating and paramagnetic above the Curie temperature while lowering the temperature becomes ferromagnetic metallic. For $x \leq 0.17$ an insulating phase occurs also at temperature below T_C. Moreover, it is metallic for $x > 0.3$. If $x > 0.5$ an antiferromagnetic metallic (AFM) stable phase occurs.

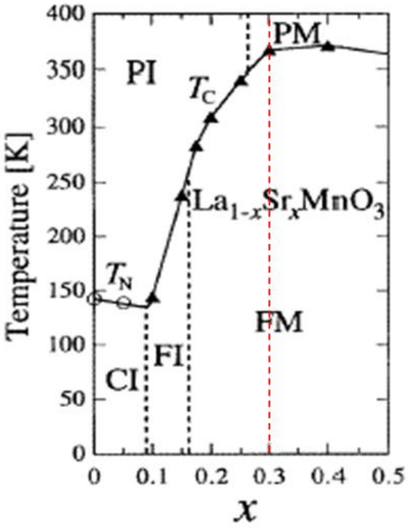

Figure 1.8. Phase diagram of $La_{1-x}Sr_xMnO_3$ [19]. PM, PI, FM, FI and CI denote paramagnetic metal, paramagnetic insulator, ferromagnetic metal, ferromagnetic insulator and spin-canted insulator states, respectively.

By the way, the comparison between magnetization and resistivity, as shown in Fig. 1.9, demonstrates that, in the case of the $x = 0.3$ doping the $LSMO$ compound, $LSMO$ is a good metal in the ferromagnetic phase (below T_C), and it is a bad conductor in the paramagnetic phase (above T_C) . So that, this value of doping is usually referred as optimal for applications.

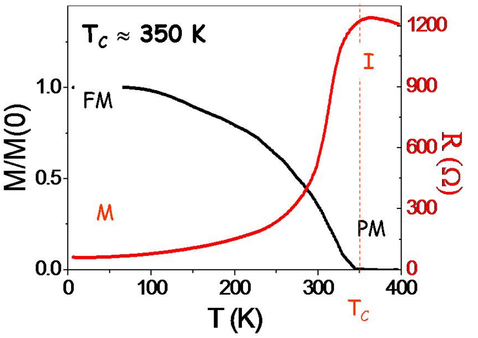

Figure 1.9. Comparison between magnetization and resistivity vs. temperature of a $LSMO$ film grown on STO (110) substrate. T_C is the Curie temperature.

At low temperature, the spontaneous alignment of the Mn spins below the Curie temperature T_C allows a delocalization of the e_g electrons, leading to a low resistivity FM phase with $\rho \sim \rho_0 + aT^{\alpha}$, with α ranging between 2 and 3 for $T \ll T_C$ [20] and ρ_0 residual resistivity.

In the high temperature region, the behaviour of $\rho(T)$ follows the simple thermal activation law $\rho = \rho_{\infty} exp\{E_0/k_B T\}$, that takes into account the depression of the *DOS* at the Fermi level due to the strong localization of the carriers [20].

1.4. Magnetic properties

By minimizing the energy of a ferromagnetic system, described in terms of applied magnetic field H, volume saturation magnetization M_S or anisotropy constants K, we obtain its (local) equilibrium states at particular experimental conditions. It is important to remark that energetics of ferromagnetic films is fairly different from that of the bulk materials. While some energy scales, such as those related to the interaction between magnetization M and H (Zeeman energy) are common to both cases, there are some terms (such as the demagnetization energy and the interlayer coupling energy) which are rather unique to the case of thin films [21].

The relevant terms in the Hamiltonian that describes a ferromagnetic system are the *exchange interaction* energy, that accounts for the presence of a *long-range* magnetic order, and the *Zeeman* energy, that comes out of the interaction between the external magnetic field and the spins. The *exchange interaction* energy can be written in the form [21]

$$E_{ex} = \sum_{i \neq j} J_{ij} \vec{S_i} \cdot \vec{S_j} \tag{1.7}$$

where J_{ij} refers to the exchange constant between two atomic spins S_i and S_j. A positive J_{ij} implies ferromagnetic coupling. Besides, the *Zeeman energy* per unit area is

$$E_{Zeeman} = -t\vec{H} \cdot \vec{M}_S \tag{1.8}$$

where t is the thickness of the ferromagnetic layer. It is worth to note that Eq. 1.8 can only be applied to systems that have homogeneous magnetization, which only happens in particular systems (for example ellipsoids or small magnetic particles).

The magnetization of ferromagnets usually shows a directional dependence. For example, a *magnetocrystalline anisotropy* along different crystal orientations results from the combined effects of the spin-orbit coupling and the crystallographic structure of material [22].

Shape anisotropy If there is a magnetization component along the film normal direction, dipoles are formed at the film surfaces and a *demagnetizing* field H_d opposing to the magnetization, is generated. This effect can be characterized by a *demagnetizing factor* $\eta_d = -H_d/M_S$ where M_S is the saturation magnetization of the ferromagnet [23]. For a simple treatment [22] we can regard a thin films as a disk-like ellipsoid (which always has a uniform magnetization within its volume) with a large thickness-to-diameter ratio. By doing this we obtain a demagnetizing factor close to 1 in S.I. (while it is $\eta_d \sim 4\pi$ in C.G.S.) along the short ellipsoid axis (film normal direction), and close to zero along the long axes (film plane direction). The volume energy density associated with this shape anisotropy is given by

$$E_d = -\frac{1}{2} \int\limits_{sample} \vec{H}_d \cdot \vec{M} dV = -\frac{1}{2} \int\limits_{sample} \eta_d M^2 dV \tag{1.9}$$

Therefore M generally lies in the film plane, unless the large cost in energy due to demagnetization is compensated by the magnetocrystalline anisotropy or by the magnetostriction (vide infra).

Magnetocrystalline anisotropy The anisotropy can be an intrinsic property of a material depending on its crystal symmetry [22]. In the case of *LSMO* films the *JT* distortion (see Sec. 1.1) lowers the simmetry with respect to the cubic perovskite simmetry. In the case of the tetragonal symmetry that is achieved in films, the uniaxial magnetic anisotropy energy (E_u) can be written as [24]:

$$E_u = K_u sin^2\theta \tag{1.10}$$

where θ is the angle between $\overrightarrow{M}$ and the easy axis of magnetization.

Induced anisotropy Epitaxial films are stressed by the substrate. Hence, the coupling between the magnetization and the strain, due to the spin-orbit interaction, induces a *magnetostrictive effect* [22], which is essentially a *magnetoelastic* stress. When the films are stressed, the anisotropy axes can move either towards or away from the stress axis, depending on the sign of the *magnetostrictive constant* λ. Materials with positive λ, as in the case of *LSMO*, tend to switch the anisotropy axis towards the tensile stress direction, while those with negative λ tend to switch the axis towards a compressive stress direction. For the *LSMO* films the magnetostrictive constant at $100K$ is found to be $\lambda_{100K} = 2.2 \times 10^{-5}$ [25] while a negligible magnetostrictive effect is reported for "simple" ferromagnets, such as $Ni_{0.80}Fe_{0.20}$ (Py) (λ of magnitude 10^{-6} has been found in polycrystalline *Py* films with thickness above $10nm$ [26]). The magnetoelastic anisotropy energy can be written as:

$$E_{mel} = K_1^{eff} cos^2\theta \tag{1.11}$$

In terms of the magnetostriction constant λ, the effective in-plane biaxial magnetic anisotropy is $K_1^{eff} = -3\lambda\varepsilon Y/2$ [24, 27], where Y is Young's modulus ($Y = 5 \times 10^{11}$ N/m^2 [28]) and ε the in-plane strain defined in 1.4.

1.4.1. Magnetic domains and domain walls

The existence of regions of uniform magnetic polarization (*domains*) in ferromagnetic materials was first postulated by Weiss, and explained by Landau and Lifshitz in terms of domain formation as a consequence of energy minimization [29]. Ferromagnets have an internal structure that is divided into *domains*, each of which is a region of uniform magnetic polarization. As known, the equilibrium configuration of domains is such to minimize the energy of the stray fields, as it happens in the closed loop configuration [30] (Fig. 1.10).

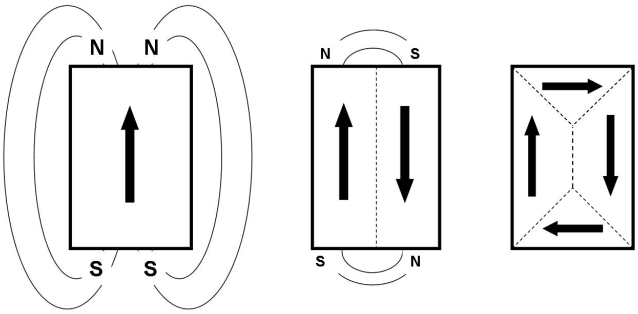

Figure 1.10. Origin of magnetic domains in a ferromagnet.

When a magnetic field is applied, the boundaries formed between adjacent domains having different magnetization directions shift and the domains rotate. Both these effects cause a change in the sample size (*magnetostriction*). The domains are separated by *domain walls* (DWs), in which the magnetization direction is smoothly twisted.

The energy density associated with such domain walls can be expressed as a sum of exchange energy plus anisotropy energy [22]. In the particular case of a 180° wall (in which the adjacent domains have antiparallel magnetizations) the total energy density is given by

$$E_{DW} = \left(\frac{\pi J_{ex} S^2}{wa}\right) + Kw \tag{1.12}$$

where w is the width of the domain wall, J_{ex} is the exchange constant between two spins S, and a is the lattice constant of a cubic crystal. The value of w can then be calculated by solving the equation $\partial E/\partial w = 0$, giving

$$w = \sqrt{\frac{\pi^2 J_{ex} S^2}{Ka}} \tag{1.13}$$

The above described DW is known as *Bloch wall*, in which the magnetization transition takes place in a direction perpendicular to that of the neighbouring domain magnetization (Fig. 1.11*(a)*). This may not be favourable in the case of ultrathin films, due to dipole formation at the film surfaces. In such cases *Néel walls* can be formed, in which the transition occurs within the plane of the adjacent domain magnetization directions (Fig. 1.11*(b)*).

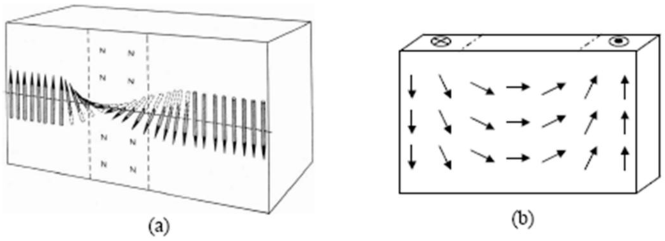

Figure 1.11. Schematic diagrams showing *(a)* a 180° Bloch wall and *(b)* a Néel wall [22, 30].

1.4.2. Magnetization reversal and hysteresis

The reversal of magnetization within ferromagnets under the influence of an external magnetic field can be described qualitatively by domain nucleation, domain wall motion and magnetization rotation [22]. With the aid of a hysteresis loop ($M(H)$ loop) in Fig. 1.12, starting from a saturation field $+H_S$, reversible magnetization rotation occurs as the field decreases, returning the magnetization back to its anisotropy axes. As the field continues to decrease (following the arrows), new domains are nucleated within the existing ones. The Zeeman energy associated with individual domains favours the "growth" of domains with magnetization vectors along (or with a component along) the field direction, which takes place by DW motion. This process continues until the unfavourable domains are eliminated. The final stage of the reversal process ($-H_S$) involves the rotation of remaining domains from their anisotropy axes towards the field direction, finishing half of the reversal cycle. The above description is highly simplified for the actual situation, and deviations are likely to happen locally due to inhomogenities.

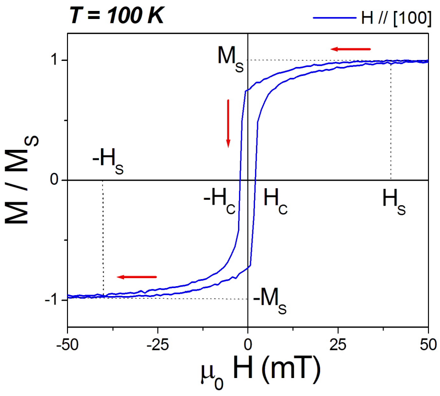

Figure 1.12. Typical magnetic hysteresis loop of a single layer of ferromagnetic film (in this case the film is a $10nm$ thick $LSMO$ grown onto (001) STO). The external magnetic field H is applied along the [100] *in-plane* direction. H_C and H_S is the coercivity and the saturation field, respectively. M_S is the saturation magnetization.

The magnetization of the sample does not vanish when the field sweeps towards zero. There is some lapse of field, called the *coercivity* of the sample H_C, before the magnetization comes to zero. The size of coercivity is important in determining the potential applications of particular materials, and is the consequence of a number of intrinsic and extrinsic factors.

— *Anisotropy:* As already discussed above, the anisotropy is the tendency of the magnetization to stay along particular axes. Anisotropy could be both intrinsic (*magnetocrystalline*) or extrinsic (*induced and shape*) in nature. The strength of the anisotropy is the dominating factor in determining the coercivity of bulk ferromagnets and epitaxial films.

— *Grain size and defects:* grain boundaries (GB) and numerous defects in the films can be extra sources of coercivity, hindering the magnetization reversal processes. These features act as additional barriers for the motion of DWs. Magnetization reversal dissipates more energy than in perfect lattice structures, giving rise to enhanced coercivity. On the contrary, it is known that amorphous films may have extremely low coercivity [22]. In this case, the average distance between defects is smaller than the DW size, which become inefficient in impeding the magnetization processes. This, together with the virtual absence of magnetocrystalline anisotropy in such films due to their amorphous nature, gives very low H_C values.

The above discussed effects of the intrinsic and extrinsic material parameters can be incorporated into a single model to describe the magnetization reversal of ferromagnets. The difficulty is that the reversal process is complicated by the domain walls-defects interactions. Besides, magnetization processes can take the form of domain nucleation, wall motion and magnetization rotation. The *Stoner-Wohlfarth* (SW) model [31] is the most commonly employed model in describing the hysteresis behaviour of magnetic materials. In such a model, we consider non-interacting single domain particles with uniaxial anisotropy. The reversal mechanism is assumed to be entirely due to magnetization rotation, according to the energy equation

$$E = E_{ex} + E_{Zeeman} + E_{mc} + E_{mel} \tag{1.14}$$

where the terms correspond to the exchange interaction, the Zeeman, the uniaxial magnetic anisotropy, and effective in-plane biaxial magnetic anisotropy energy, respectively. Magnetization behaviour of the system is determined from the local minima of Eq. 1.14. The major advantage (or disadvantage) of the SW model is its simplicity, in which the reversal is treated solely in terms of rotations.

1.4.3. Magnetoresistive effects

The *CMR* consists in a large reduction of the electric resistance when an external magnetic field is applied (Fig. 1.13).

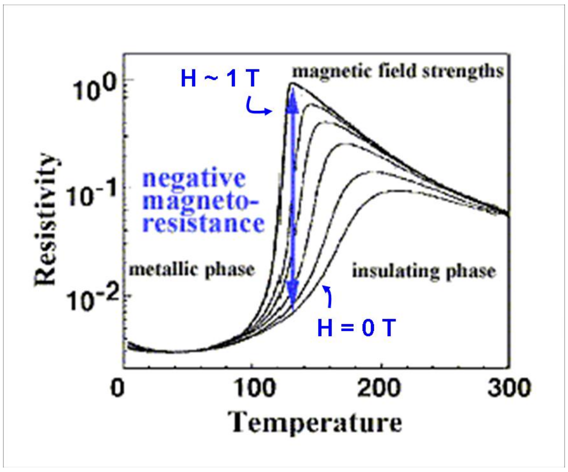

Figure 1.13. *CMR* effect for a $La_{0.7}Ca_{0.3}MnO_3$ compound (after [32]).

In manganites, it is explained by the interplay between the double-exchange term that promotes hopping of the carriers, and a strong interaction between electrons and lattice distortions, that is responsible for the localization of the carriers [33]. This effect arises from the close correlation between the magnetic phase transition and the electronic phase transition near the Curie temperature in maganites. If an external magnetic field satured the material ($H = H_{sat}$), the hopping of an electron sited on a Mn^{3+} to an Mn^{4+} ion is favoured when conserving its spin orientation (*DE* model) (Fig. 1.14). A *CMR* of 60% was observed by Von Helmotz in $La_{0.67}Ba_{0.33}MnO_3$ thin films at room temperature in 1993 [34]. In 1994, Jin *et al.* [2] reported an *MR* effect of millions percent at $77K$ in $La_{0.67}Ca_{0.33}MnO_3$ thin film. However, since high magnetic field are required (few Teslas) no imminent technogical applications based on such effect are envisaged [35].

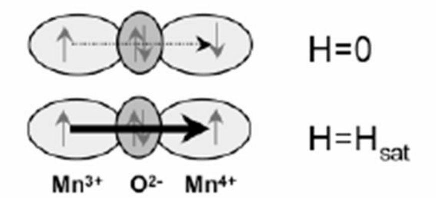

Figure 1.14. Schematic of the colossal magnetoresistance mechanism.

While in manganites the maximum effect of the *CMR* is found close to the Curie temperature, at low temperature the anistropy magnetoresistance (*AMR*) dominates. The *AMR* arises from the dependence of the electrical resistance on the angle between the direction of electrical current and orientation of magnetization vector (Fig. 1.15). It is attributed to a larger probability of *s-d* scattering of electrons in the direction of magnetic field. The magnetic field magnetizes the material, that is, it aligns the spin system, and the spins affect the electric conductivity through the spin-orbit interaction [36]. The net effect is that the electrical resistance has its maximum value when the direction of the current is parallel to the applied magnetic field. Being θ the angle between $\overrightarrow{M}$ and the current i, the resistivity is $\rho(\theta) = \rho_{\perp} + (\rho_{\parallel} - \rho_{\perp})cos^2\theta = \rho_{\perp} + \triangle\rho_{max}cos^2\theta$. The *AMR* is defined as follows:

$$AMR = \frac{\rho_{\parallel} - \rho_{\perp}}{\rho_{\parallel}} \tag{1.15}$$

Values of AMR up to 0.3% are typically obtained in *LSMO* at low temperature, while it usually vanishes at higher temperatures [35].

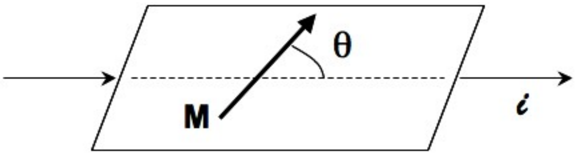

Figure 1.15. Schematic of the anisotropic magnetoresistance (*AMR*).

1.5. Thickness effects on the physical properties of LSMO films

The physical properties of the manganites films consistently differ from those of the parent bulk compound mainly because of the effects of the strain induced by the substrate. Indeed, it has been found that properties such as magnetoresistance, magnitude of the temperature T_C, resistivity, magnetization [37, 38], transport and magnetic anisotropies [39], and spin and orbital order structure [40] are sensitive to the *epitaxial strain.* These properties are different from the changes induced by hydrostatic or chemical pressure, since *in-plane* strain generally leads to an *out-of-plane* strain of different sign. Moreover the effects induced by the substrate are able to influence the tendency toward phase separation (*PS*), induce inhomogeneities in films, and cause new electronic behaviour not found in bulk materials of the same composition [41, 42].

The strain in *LSMO* films can be expressed by the sum of two terms: a ***bulk strain*** (ε_B) and a ***biaxial strain*** (ε^*). Millis *et al.* [43, 44] proposed the following dependence of T_C on strain:

$$T_C(\varepsilon_B, \varepsilon^*) = T_C^0[1 - a\varepsilon_B - b\varepsilon^{*2}] \tag{1.16}$$

where, in the case of films grown on (001)-oriented substrates,

$$\varepsilon_B = \frac{1}{3}[2\varepsilon_{[100]} + \varepsilon_{[001]}] \tag{1.17}$$

$$\varepsilon^* = \frac{1}{2}[\varepsilon_{[001]} - \varepsilon_{[100]}] \tag{1.18}$$

and T_C^0 is the Curie temperature of the unstrained *LSMO.*

The effect of ε_B and ε^* on T_C has different origin. The hydrostatic compression tends to increase the electron hopping between two adjacent Mn ions enhancing the Curie temperature. On the other hand, in the case of tensile strain the stretching of the $Mn - O$ bonds reduces the *in-plane* electron transfer inducing a reduction of the T_C. Otherwise, the biaxial strain (ε^*) increases the energy difference between the e_g levels imposed by the Jahn Teller distortion, reinforcing the electron tendency to be localized, thus determining a reduction of the Curie temperature in both tensile and compressive strained *LSMO.*

Another relevant effect that takes place in films is the appearance of a non magnetic layer, called *dead layer*, which can extend to a depth of some nm from the surface. The existence of such dead layer was demonstrated for common ferromagnetic metals and alloys by comparing the magnetic moment of samples with different thickness and in the case of $LSMO$ also by comparing the values of the electrical conductance. The thickness of the dead layer strongly depends on different parameters, among which are the annealing time, the annealing temperature, the deposition technique and even the kind of substrate [45, 46]. Recently, the existence of an insulating *dead layer* has also been proven [46] in ferromagnetic $LCMO$ at the interface with Platinum (Pt). Some authors [47, 48] suggested that this intrinsic insulating layer can be used as a tunnel barrier for the fabrication of high quality magnetic tunnel junctions. It is not clear whether the formation of this insulating barrier is localized in the topmost layers of the manganite or it must be rather ascribed to the oxidation of the metal close to the interface because of oxygen diffusing from the manganite.

Fig. 1.16 shows the principal features of the thickness dependence of the $LSMO$ film deposited onto STO, LAO and NGO substrates [49]. Fig. 1.16*(a)-(c)-(d)* illustrates the behaviours of the *out-of-plane* lattice parameter, MIT temperature and MR increasing the film thickness, respectively. It is found that above a certain thickness ($\sim 150nm$) the $LSMO$ film "relaxes" taking back the bulk properties. Otherwise, below a *critical thickness* the $LSMO$ film shows a drastic drop of the MIT temperature and of the MR, while the crystal quality results even better (Fig. 1.16*(b)*).

To conclude, we have seen that the strain affects so many quantities. Thus, it can be used to control the properties of interest by depositing films on different substrates and in different growth orientations, changing the deposition conditions and the postannealing procedure, and varying the thickness [50].

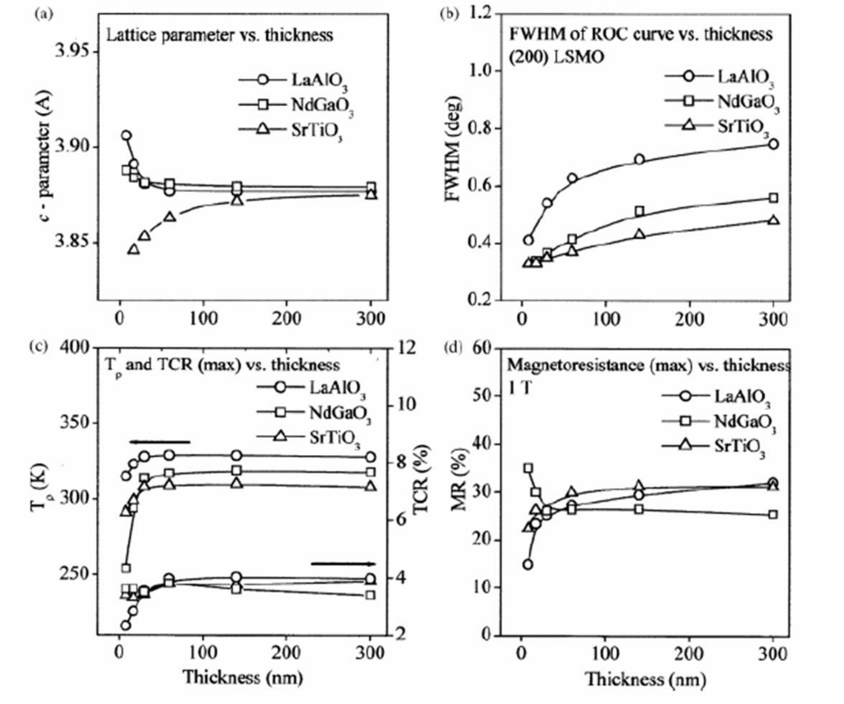

Figure 1.16. The substrate and thickness effects on structural, electrical and magnetic properties of $LSMO$ films deposited on STO, LAO and NGO substrates (from [49]).

1.6. Terminating and vicinal surfaces

The substrate surface properties, i.e., morphology and terminating atomic plane, affect the epitaxial film growth and can be used to tailor the properties of the films themselves. To obtain epitaxial $LSMO$ films, atomically flat, crystalline surfaces are required. Surfaces free of contaminants like CO and H_2O are usually obtained by proper treatment.

Here, I refer in particular to the STO, that is largely employed in this work as substrate for the $LSMO$ growth. The STO unit cell is schematically depicted in Fig. 1.17*(a)*. It consists of Ti occupying the corner position and Sr sited at the body center. The Ti is 6-fold coordinated to oxygen forming the corner-sharing oxygen octahedrals. The structure of STO can be viewed as a stack of alternating TiO_2 and SrO planes along one of the principal axes. A top view of the TiO_2 and of the SrO planes is visualized in Figs. 1.17*(b)* and 1.17*(c)* respectively. In real substrates, the surface terminates either with TiO_2, SrO or a mixture of both. A preference towards TiO_2 termination is predicted by surface energy calculations [51]. Several groups determined the surface composition of STO and showed that thermal treatments in oxygen [52, 53, 54, 55] as well as reducing [56, 57, 58, 59, 60] environments, result in any of the above mentioned terminations. A reliable method to obtain a single termination is a chemical treatment. Here, the difference in solubility of SrO and TiO_2 in acids is employed. The first reported chemical procedure [61] to control the surface terminating layer utilized a NH_4F buffered HF solution ($pH \sim 4.5$) for the removal of SrO from the surface without etching of the TiO_2. After subsequent thermal treatment a crystalline TiO_2 terminated STO surface was obtained. Just recently, Van der Heide *et al.* [62] studied such TiO_2 terminated (001) STO surfaces and observed a well-ordered TiO_2 surface layer. Low energy electron diffraction ($LEED$)[1] patterns indicate a 1×1 structure. However, after prolonged annealing ($T \geq 800$°C) for several hours in O_2 these authors found disordered surface, indicating Sr segregation toward the surface.

In conclusion, the (001) STO surface termination is very sensitive to surface treatments. Depending on the conditions, i.e., temperature, anneal time and environment, thermal treatments can lead to SrO, TiO_2 and a mixture of both in the terminating atomic plane.

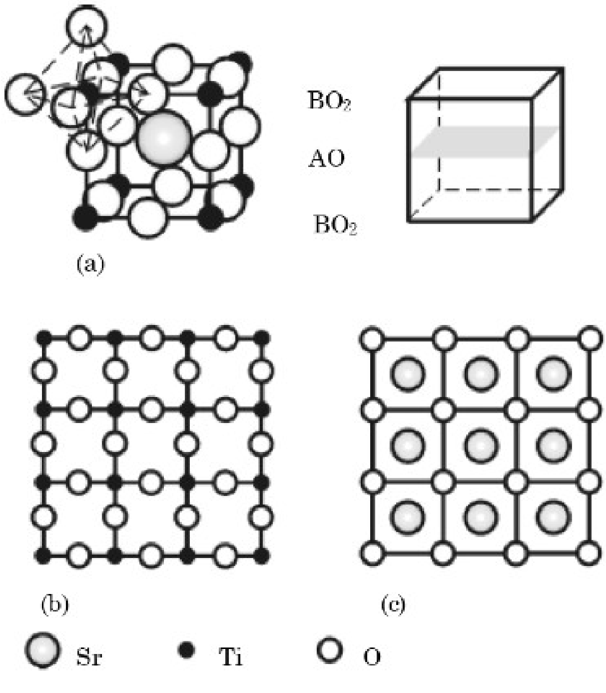

Figure 1.17. Schematic view of the $SrTiO_3$ unit cell with ABO_3 perovskite structure (a). Top view of the TiO_2, i.e., BO_2 (b) and SrO, i.e., AO (c) terminating plane (after [96]).

---

[1] The electron diffraction will be discussed in Chap. 3

Either mechanical and chemical surface treatments can be also employed to obtain atomic steps on the sample surface. A vicinal surface (see Fig. 3.20) is fabricated by a slight miscut of the substrate surface along an orientation close to a high symmetry one. It is made up of low index terraces separated by unit cell steps in the case of perovskite substrates. The terrace width (L) is determined by the miscut angle (vicinal angle θ_{vic}), defined as the angle between the actual surface plane and the high symmetry plane, and by the step height (d). The steps break the fourfold rotational symmetry of the substrate surface and therefore it influences the properties of the films, such as the magnetization, inducing a uniaxial magnetic anisotropy [63], influencing strongly the in-plane magnetization reversal within thin and ultrathin films [64].

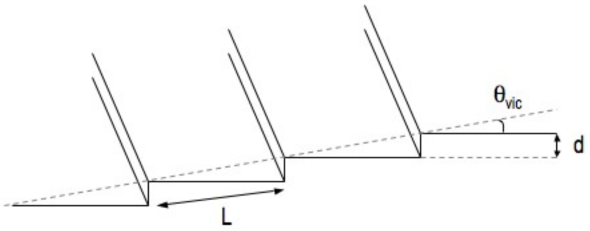

Figure 1.18. Sketch of the vicinal surface, being θ_{vic} the vicinal angle, L the terrace width and d the step height.

Chapter 2

Device applications of manganites

Haghiri-Gosnet *et al.* [11], and previously Venkatesan *et al.* [65], classified the most interesting device applications of *CMR* manganite thin films as follows:

- — bolometric application: metal to insulator transition (high *Temperature Coefficient of Resistivity* (*TCR*))
- — magnetic application: spin valve, vertical and planar junctions for non-volatile memory and microwave application using magnetoresistive properties (*MR*)
- — electrical application: *STO* gate and ferroelectric gates in *Field Effect Transistor* (*FET*)
- — low temperature hybrid high temperature superconducting: *CMR* devices

In this thesis, I focus the attention on the bolometric applications (see Chap. 4) and magnetic junction devices (see Chap. 6) based on high quality *LSMO* films with well controlled and tailored properties (see Chap. 3).

2.1. Infrared detectors

Due to the large variation of the resistivity at the *MIT* temperature, that is close to the room temperature, the *LSMO* is considered [4, 66, 67] as a promising material for application to uncooled infrared (*IR*)[1] bolometer. An *IR* detector is a transducer that converts the energy of the absorbed radiation into an electric signal. The field of application of *IR* detector is nowadays extremely wide: explorer of space and terrestrial objects, security guard, medical investigation, night-vision systems for automobiles, fire detecting, industrial and constructional areas in any kinds of weather condition. The temperature coefficient of resistivity (*TCR*), defined as

$$TCR = \frac{1}{R}\frac{dR}{dT} \tag{2.1}$$

is one of the main figure of merits of bolometric materials. Fig. 2.1 shows the *TCR* values of several manganite compounds. The highest values are found in materials that are not suitable for room temperature applications. Notably, *LSMO* demonstrates a *TCR* at $300K$ that is larger than amorphous *Si* (see e.g. Tab. 2.1).

---

[1] The range of *IR* is classified into middle wavelength *IR* (*MWIR*, $3-5\ \mu m$), long wavelength *IR* (*LWIR*, $8-14\ \mu m$) and far *IR* (*FIR*, $30-1000\ \mu m$).

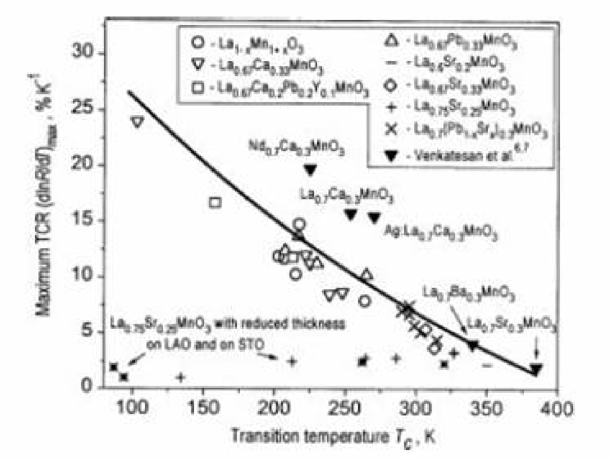

Figure 2.1. Maximum TCR values according to transition temperature T_C of manganite films for bolometric application (after [68]).

Schematically, the IR detectors may be divided into two groups: thermal detectors and non-thermal detectors.

A *thermal detector* absorbs photons in the "absorber" film, that is heated. The temperature increase is measured by a resistive thermometer (see e.g. Eq. 2.1) in bolometers, by thermoelectric-induced voltage in thermopiles, or by pyroelectric effect. These thermal detectors must be constructed on structures that are thermally isolated from the sorrounding in order to enhance the temperature change. Referring to the sketch in Fig. 2.2*(b)*, the properties of the thermal detector can be expressed by a thermal capacitance C_{th} $[J/K]$, called thermal mass, and the absorbing volume to store heat energy. The sensing area is thermoelectrically coupled to the supporting structure (substrate and/or buffer layers) (thermal conductance G_{th} $[W/K]$). To develop highly sensitive thermal detector, the corresponding temperature change must be as large as possible while the C_{th} and G_{th} must be minimized [69]. In order to lower the heat flow, Méchin *et al.* micromachined thermal insulating materials as a supporting membrane [70].

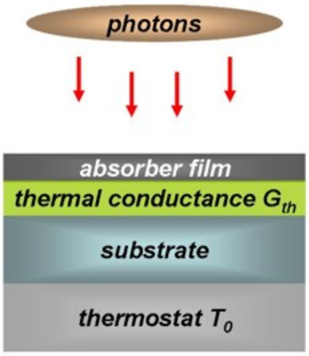

Figure 2.2. Schematic view of a infrared thermal detector.

The principle of the *non-thermal detectors* is that the absorbed radiation affects the electronic energy distribution in the sensing material driving it to a non equilibrium state. This determines a fast variation of the transport properties resulting in an electric signal [71].

Thermal detectors are usually less sensitive and slower than non-thermal detectors, but the detecting wavelenght range is much larger since it only depends on the chosen absorbing material. Above $1mm$, thermal detectors are the most competitive detectors.

An alternative idea is to fabricate fast detectors using manganites by analogy to what is done using superconducting materials [72]. Because of their fast optical response ($\sim 1ps$) the superconductors, such as *YBCO,* are commonly used for this application [72]. The disadvantage of these detectors is that a cryogenic cooling system is required. Due to its fast responsivity at room temperature, *LSMO* circumvents this problem. In order to prove this statement, I measured the response delay time of *LSMO* thin films grown onto (001) *STO* (Fig. 2.3) that I fabricated in the M.O.D.A. laboratory in Naples (see Sec. 3.2.3 for details on the films growth) resorting to a pump-probe[2] technique [73]. The pump energy was $1.4eV$ ($\lambda = 800nm$), the laser fluence was ranged between $0.05\mu J$ and $1.5\mu J$, and the resolution delay time was $40fs$. The fast responsivity is due to the electron interaction after the pumpe pulse ($\sim 0.3ps$) (Fig. 2.3*(a)*). The lattice thermalizes in a time scale $1-2$ order of magnitude longer (Fig. 2.3*(b)*). Responsible of such thermalizations are the lattice phonons and the electron spins. The overall thermalization is then completed in few ns (Fig. 2.4).

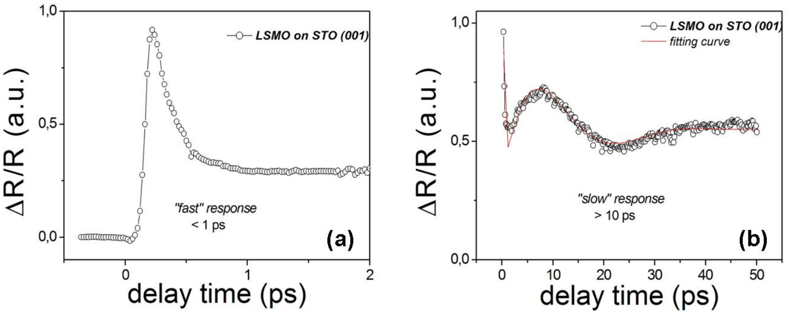

Figure 2.3. Pump-probe optical reflectivity of a $30nm$ thick *LSMO* film grown onto (001) *STO* substrate. The fast responsivity ($< 1ps$) is due to the electron interaction after the pump pulse *(a)*. The lattice thermalizes in a longer time scale ($> 10ps$) *(b)*.

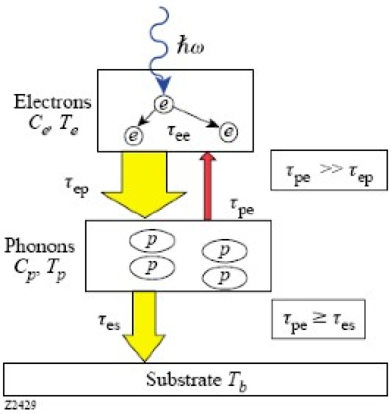

Figure 2.4. Relaxation times due to electron, phonon and spin interaction in the absorber film (from [72]).

---

[2] These measurements were performed at the Laboratoire d'Optique Appliquée (*LOA*), Ecole Polytechnique in Palaiseau with the group of the Prof. D. Boschetto.

2.1.1. Sensitivity and noise characteristic of bolometer

The sensitivity $\Re_V[V/W]$ of a bolometer is defined as the ratio between the voltage change ΔV and the radiation power ΔP. In practice, the input power is the sum of the optical power and the electrical power brought by the bias current (Joule heating).

In the case of harmonic power variations, the microbolometer behaves as a first-order system where the sensitivity is expressed as [70]:

$$\Re_V = \frac{\Delta V}{\Delta P} = \frac{RI_b\eta}{G_{th}\left(1 + j\omega\tau\right)}TCR \tag{2.2}$$

where η, R are the radiation absorption coefficient and the electrical resistance of the sensing material, ω the angular frequency of the absorbed radiation, and I_b is the applied bias current. The thermal time constant τ is the ratio of the thermal mass over the thermal conductance: $\tau = C_{th}/G_{th}$. Because of the relation between $\Re_V$ and τ, high sensitivity are obtained at low frequency. It is worth to remark that in Eq. 2.2, C_{th} and G_{th} are strongly linked to the geometry of the device while TCR is only dependent to the electrical transport property on the sensing material.

The minimum temperature change that can be detected gives an output signal equal to the root mean square of the electronic noise. Therefore, the performance of bolometers can be evaluated by the *noise equivalent power* (*NEP*, $W/\sqrt{Hz}$). The *NEP* is the sensitivity of bolometer to fluctuations in incident energy. Such fluctuations (*noise*) are unwanted disturbance. The main sources of noise in the bolometer and its readout circuit are the *Johnson noise*, due to random thermally excited vibration of charge carriers in a conductor ($S_{V_J} = 4k_BTR$), the *phonon noise* due to the phonons that transport energy from the absorber and the heat sink through the thermal conductance G_{th} ($S_{V_{ph}} = \Re_V^2 \cdot 4k_BT^2G_{th}$), and $1/f$ *noise* that occurs at low frequency ($S_{V_{1/f}} = \frac{const}{f^\alpha}$) [69].

Being $S_V = \sqrt{S_{V_J}^2 + S_{V_{ph}}^2 + S_{V_{1/f}}^2}$ the overall noise spectral density with assumption of negligible photon noise from the incident radiation and readout circuit noise, the *NEP* can be finally defined as the ratio between the total noise spectral density and the sensitivity

$$NEP_V = \sqrt{\frac{S_V}{\Re_V^2}} = \sqrt{4k_BT^2G_{th} + \frac{4k_BTR}{\Re_V^2} + \frac{S_V(f)}{\Re_V^2}} \tag{2.3}$$

The semi-empirical *normalized Hooge parameter* (α_H/n) enables the comparison of the $1/f$ noise level in materials independently of the bias conditions and sample geometries. Being n the charge carrier density and Ω the volume considered, f the frequency the normalized Hooge parameter is defined by the following formula [74]:

$$\frac{\alpha_H}{n} \times \frac{1}{\Omega \times f} = \frac{S_V(f)}{V^2} \tag{2.4}$$

2.1.2. Room temperature bolometers

Low *NEP* values are requested for high performance bolometers. Besides, from the material point of view, high *TCR* and low α_H/n are required. Typical materials that can be employed in room temperature bolometers are: VO_x, semiconducting *YBCO*, amorphous *Si* and manganites. Tab. 2.1 lists the *TCR* and the normalized Hooge parameter values for such materials including manganite thin films obtained by different research groups. It is worth to note that the most promising result was achieved by Kim *et al.* on $La_{0.67}(Sr,Ca)_{0.33}MnO_3$ manganite films deposited on *Si* substrates [75].

In this framework, I optimized the growth of the *LSMO* onto buffered silicon buffered by using different template layers (as it is discussed in Chap. 4), partecipating to the research activity on uncooled bolometers at the *GREYC* laboratory in Caen.

Ref.	*Composition*	$T(K)$	$TCR(K^{-1})$	$\alpha_H/n(m^3)$
[76]	$La_{0.72}Sr_{0.28}MnO_3/\ STO$	300	+0.025	2.2×10^{-32}
[77]	$La_{0.7}Sr_{0.3}MnO_3/\ MgO$	300	+0.02	1.6×10^{-26}
[4]	$La_{0.7}Sr_{0.3}MnO_3/\ STO$	300	+0.030	9×10^{-31}
[78]	$La_{0.7}(Pb_{0.63}Sr_{0.37})_{0.3}MnO_3/\ LAO$	300	+0.074	3×10^{-27}
[75]	$La_{0.7}(Sr, Ca)_{0.3}MnO_3/$ buffered Si	294	+0.044	1.6×10^{-26}
[79]	$YBCO$ semiconductor	300	−0.031	10^{-29}
[80]	VO_x	300	−0.033	10^{-29}
[80]	*amorphous Si*	300	+0.0021	-

Table 2.1. *TCR* coefficients, ***Hooge normalized parameters*** a_H/n at $30Hz$ and $300K$ of *LSMO* films of different composition compared with other materials used as room temperature thermometers.

2.2. Spin polarization and spintronics

As already noted, adding the spin degree of freedom to conventional charge-based electronic devices has potential advantages in terms of nonvolatility, increased data processing speed, decreased electric dissipation, and increased integration densities compared with conventional semiconductor devices [3, 6]. Thus, a new technology based on spin transport electronics (***spintronics***), where it is not the electron charge but the electron spin that carries information, offers opportunities for a new generation of devices combining standard microelectronics with spin-dependent effects that arise from the interaction between spin of the carrier and the magnetic properties of the materials.

The shift in energy of the two spin densities of free charge carriers (***spin-up*** $N_{\uparrow}(E_F)$ or ***spin-down*** $N_{\downarrow}(E_F)$, see Sec. 1.2) is the source of the magnetic moment associated to a spin polarization (Eq. 1.6). In the ideal case of 100% spin polarization, the only states that are available to the carriers are those for which the spins are parallel to one direction. If the magnetization of the materials is reversed by applying an external field, the spin direction of those states also reverses. Thus, depending on the direction of magnetization of a material relative to the spin polarization of the current, the material can work as either a conductor or an insulator for electrons of a specific spin polarization.

In such a context, I worked at the *LAM* laboratory in Cassino and at the M.O.D.A. laboratory in Naples to the realization of prototype devices for *MR* applications, based on high quality *LSMO* films that I deposited in the M.O.D.A. lab with well controlled properties (as it is discussed in Chap. 6, Secs. 6.1, 6.3) and at the *GREYC* laboratory in Caen in the fabrication of *LSMO* films on vicinal substrates (Chap. 6, Sec. 6.2).

2.2.1. Magnetic junctions

A ferromagnetic metal may be used as a source of spin-polarized carriers injected into a semiconductor, a superconductor, or a normal metal or can be used to tunnel through an insulating barrier. The most dramatic effects are generally seen for the most highly polarized currents. Among the ferromagnets, the *LSMO* is found to have a quasi-total spin polarization (close to 100%) (for comparison *Fe*, *Co*, *Ni*, and their alloys, have a polarization *P* ranging from 40 to 50%).

Giant Magnetoresistance device The Giant magnetoresistance (*GMR*) was discovered by A. Fert in 1988 [1] in $Fe(001)/Cr(001)$ superlattices. It consists in an enhancement of the

MR ($\sim 45\%$ at $4.2K$ in $Fe(001)/Cr(001)$) due to the interlayer exchange coupling $-J_{ij}\vec{M}_i \cdot \vec{M}_j$, that can be seen as the macroscopic version of the exchange coupling (Eq. 1.7). Being θ the angle between the magnetization of two layers, he found $R(\theta) = R_0 + \frac{\triangle R_{GMR}}{2}(1 - cos\theta)$.

The basic action in a spin-polarized device (*spin valve*) is shown in Fig. 2.5*(a)* for a current parallel to the interface (*CIP*) and in 2.5*(b)* for a current perpendicular to the interface (*CPP*). It is assumed that the electrons are travelling from a ferromagnetic (*FM*) metal, through a normal (*N*) metal, into a second ferromagnetic (*FM*) metal. When the magnetic moments of the two ferromagnetic metals are in an aligned state, the resistance is *low*, whereas the resistance is *high* in the antialigned state (*giant magnetoresitance* (*GMR*)).

In order to explain the *GMR* we can refer to the "resistor" model [1] illustrated in Fig. 2.5*(c)*. Since the electrons are differently scattered in the ferromagnet layer depending on their spin, we can distinguish two resistivities, in parallel and antiparallel configuration, $\rho_P = \frac{\rho_{\uparrow\uparrow}\rho_{\uparrow\downarrow}}{\rho_{\uparrow\uparrow}+\rho_{\uparrow\downarrow}}$ and $\rho_{AP} = \frac{\rho_{\uparrow\uparrow}+\rho_{\uparrow\downarrow}}{2}$, and the giant MR is defined as follows

$$GMR = \frac{\rho_P - \rho_{AP}}{\rho_{AP}} = -\left(\frac{\rho_{\uparrow\uparrow} - \rho_{\uparrow\downarrow}}{\rho_{\uparrow\uparrow} + \rho_{\uparrow\downarrow}}\right)^2 \tag{2.5}$$

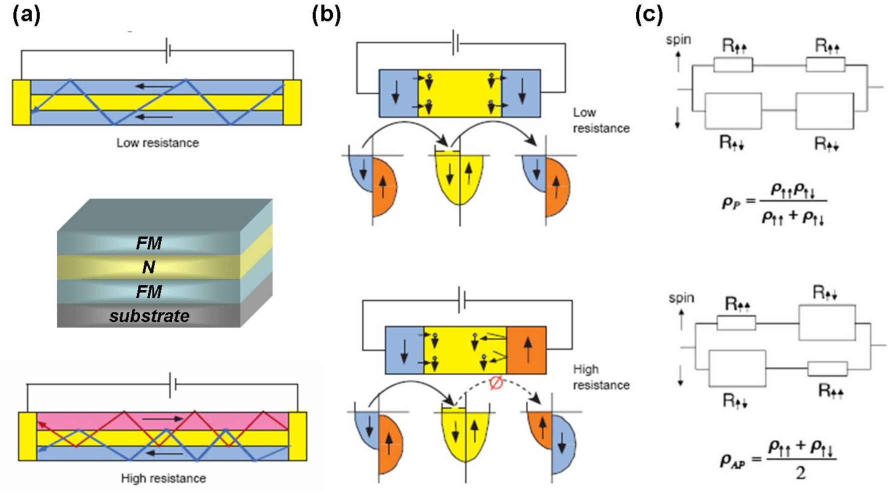

Figure 2.5. Schematic representations of spin-polarized transport from a ferromagnetic metal spaced by a normal metal in layered films in *CIP* configuration *(a)* and in *CPP* configuration *(b)*; *GMR* "resistor" model *(c)*. Depending on their spin, the electrons scattered by the ferromagnet (*FM*) layer show different resistivities (ρ_P and ρ_{AP}). (from [1, 3]) .

Magnetic tunnel junction A magnetic tunnel junction (*MTJ*) is a device in which a pinned layer (lower *FM* in Fig. 2.6*(a)*) and a free layer (upper *FM* Fig. 2.6*(a)*) are separated by a very thin insulating layer . The tunneling resistance, modulated by a magnetic field, exhibits up to thousands per cent change in the magnetoresistance, and requires a saturating magnetic field equal to or somewhat less than that required for a *GMR* device. Since the tunneling current density is usually small, *MTJ* devices generally have high resistances. The basic two terminal *MTJ* consists by two electrodes of the magnetic material separeted by a thin insulating barrier layer, through which the *spin-polarized* carriers tunnel (Fig. 2.6*(b)*). As the spin-up electrons can only tunnel into spin-up empty states, no tunneling occurs when the magnetic moment is in an anti-parallel configuration in both electrodes and the resistance of the device becomes very high. The tunnel conductance between such a layers depends on the orientations of their magnetization. In the parallel configuration, that is the magnetizations of the layers are aligned, the tunnel conductance G_P is written as $G_P(0) \propto N^1_\uparrow(E_F)N^2_\uparrow(E_F) + N^1_\downarrow(E_F)N^2_\downarrow(E_F)$. Otherwise, if the two layers have opposite magnetization, the G_{AP} is $G_{AP}(0) \propto N^1_\uparrow(E_F)N^2_\downarrow(E_F) + N^1_\downarrow(E_F)N^2_\uparrow(E_F)$. Thus, the tunnel MR is defined [81] as

$$TMR = \frac{1/G_{AP} - 1/G_P}{1/G_P} = \frac{2P_1P_2}{1 - P_1P_2} \tag{2.6}$$

where P_1, P_2 is the spin polarization of the two ferromagnets defined in Eq. 1.6.

Following the scheme in Fig.2.6*(c)*, when the two electrode are characterized by the same polarization, the electrons can tunnel trough the insulating spacer (low MR state). By applying an external magnetic field the electrodes change the polarization and a high MR state occurs. Therefore, this device is able to sense the direction of the external magnetic field. The main advantage of such a TMR device is the low magnetic field required to switch between the states.

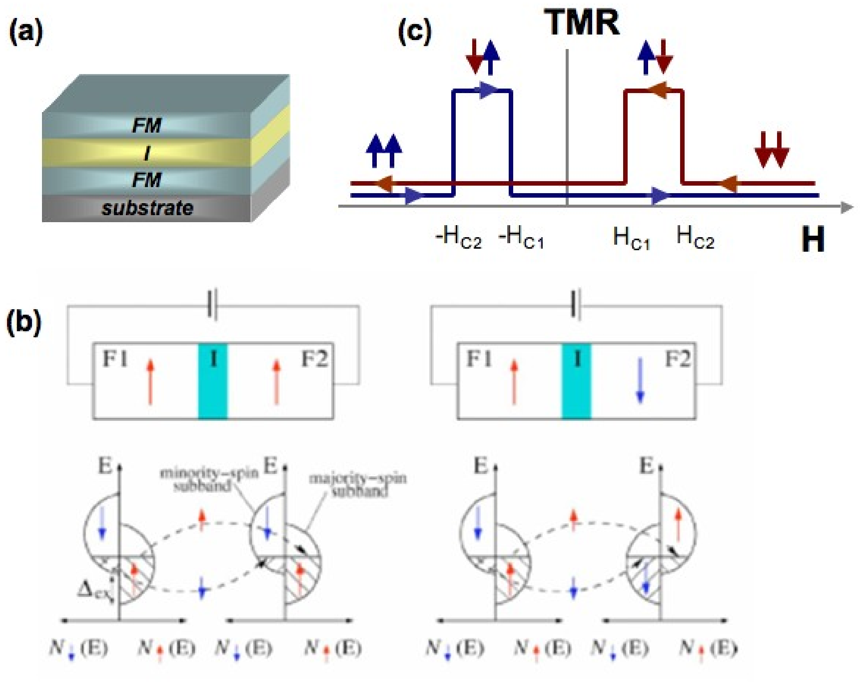

Figure 2.6. MTJ device *(a)*. Schematic representations of the tunnelling mechanisms between two ferromagnets (FM) separated by an insulating (I) spacer with aligned and antialigned magnetization (CPP configuration) *(b)*. As indicated, the spin orientation is preserved during tunneling because spin flip process have very low probability. TMR vs. applied field H ($H_{c1,c2}$ is the coercive field of the FM layer F1, F2) *(c)*.

Bowen *et al.* [82] observed a magnetoresistance of 1850% by applying a magnetic field of less than $20mT$ in $LSMO$-based tunnel junctions, from which they deduce an average spin polarization of at least 95% in $LSMO$ at the interface with STO (Fig. 2.7*(left)*). However, the temperature dependence of the magnetoresistance for these junctions shows the TMR vanishes at about $280K$ (Fig. 2.7*(right)*).

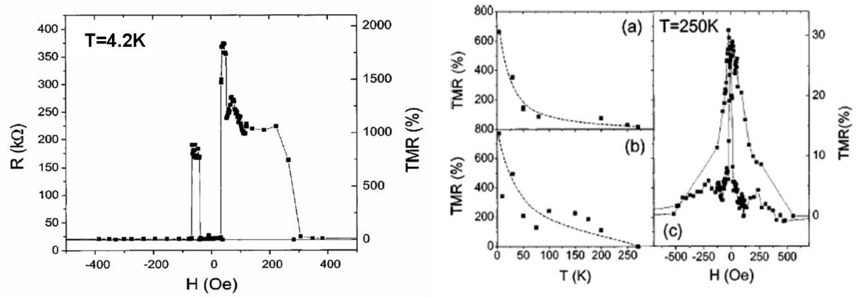

Figure 2.7. *TMR* at 4.2*K* *(left)* and at 250*K* *(right)* of *LSMO/STO/LSMO/Co* vertical junction (after [82]).

The major applications of the above mentioned magnetic junction devices concern the magnetic random access memories (*MRAM*). A disadvantage of the conventional memory, dynamic random access type (*DRAM*) and static random access one (*SRAM*), is that they are volatile because of leakage current in circuits. In order to retain data in the memory, a power consumption for refreshing is periodically necessary. The spin polarization of thin manganite films may be applied to non-volatile *MRAM*s [6]. The principle of operation of a *MRAM* is illustrated in Fig. 2.8. It basically uses magnetic hysteresis to store data and magnetoresistance to read data. The *MRAM* can exploit both the *GMR* and *TMR* effect. In the former case, the *GMR* elements are manipulated for writing or reading by applying magnetic fields that are generated by currents passing through lines above and below the elements (Fig. 2.8*(b)*), while in the latter case, the *RAM* is constructed of *MTJ* connected together in a point contact array and the conducting wires provide current to the junctions and permit voltage measurements to be made (Fig. 2.8*(c)*).

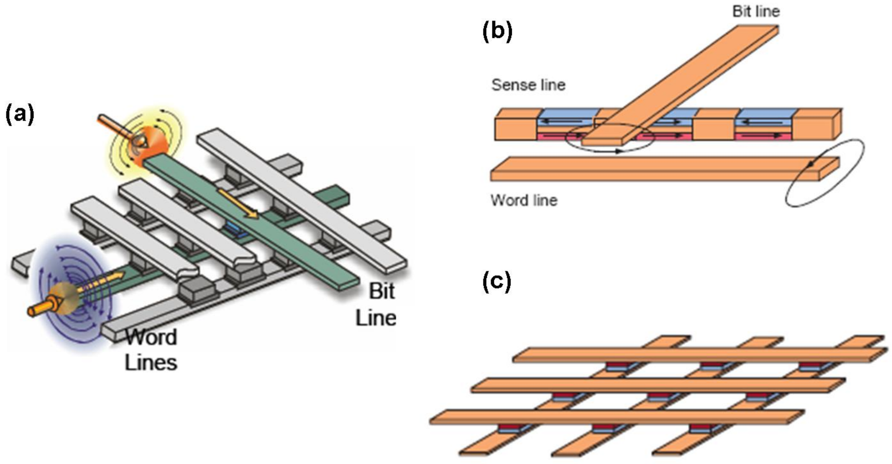

Figure 2.8. Schematic representation of a *MRAM* *(a)*, constructed of *GMR* elements connected in series *(b)* and of *MTJ* connected together in a point contact array *(c)* (after [3])

These *GMR*-based *MTJs* or pseudo-spin valve memory cells are integrated in a circuit chip and work as a static semiconductor *RAM* chip with the added feature that the data are retained with power off. Potential advantage of the *MRAM* compared with silicon electrically erasable programmable read-only memory (*EEPROM*) and flash memory is 1000 times faster writing processes and potentially higher integration due to the lower power consumption.

2.2.2. Devices based on new idea

Another idea to obtain large *MR* effects is to use the uniaxial magnetic anisotropy along step edges induced by a vicinal surface (see Sec. 1.6). Wang *et al.* [24] have observed magnetic anisotropy at 80K in ultrathin (12.6nm thick) *LSMO* films grown on 10° vicinal substrates. Yet, Mathews *et al.* [83] obtained an in-plane anisotropy at room temperature in 7nm and 25nm thick *LSMO* films deposited on *STO* (001) substrates with very low vicinal angles (0.13° and 0.24°) toward the (100) crystallographic direction. As shown in Fig 2.9, the films have uniaxial anisotropy with the easy direction parallel to the steps and the hard direction perpendicular to the steps. Since the steps generically nucleate magnetization reversal and pin the motion of domain walls, the magnetization reversal proceeds by nucleation and propagation of the *DW*s.

I will detail in Sec. 3.2.2.2 the structural and surface properties of vicinal *LSMO* films I have grown on vicinal *STO* substrates and in Sec. 6.2 the magnetic domain arrangements and magnetization reversal in these films.

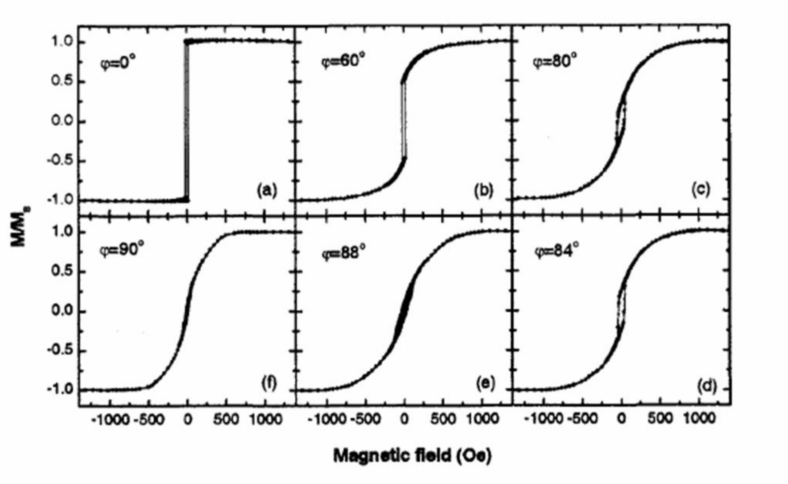

Figure 2.9. Hysteresis loops of the vicinal *LSMO* film (12.6nm thick) grown on vicinal *STO* (001) 10° tw (100) substrate at 80K measured with in-plane magnetic field applied at various angle φ with respect to [100], that is the direction of the steps [24].

In order to obtain large *MR* effects, it is also possible to introduce artificial defects, which can be either grain boundaries (*GB*), or domain walls (*DW*). The *MR* due to defects requires low field and it is clearly related to the alignment of ferromagnetic domains on both sides of the defect. It is attributed to spin dependent transmission of electrons across the *DW*.

It has been demonstrated that the introduction of a nanoconstriction in a thin ferromagnetic film favors both the pinning of *DW* inside the constriction and a lateral size reduction of the constrained-*DW* [84]. In such a constrained *DW*, the spin of the electrons cannot rotate to line up with magnetization, inducing a large increase of the resistance. If a magnetic field is applied or a pulsed current is injected, the *DW* can move and disappear. A large *MR* effect should be recorded in a half-metal.

Moreover, the nanoconstrictions, because the nanoconstrictions pin the domain walls. When located at nanocostrictions the walls become thinner and scatter electrons more efficiently. The use nanoconstrictions to control the *DWs* was exploited by several groups [85, 86, 87, 88, 89].

In Fig. 2.10, the concept at the base of a double nanocostriction valve is shown. If the magnetic moments of the *LSMO* side arms are parallel to the moment of the acicular region, a low resistance (*Low MR*) state occurs (Fig. 2.10(a)). Increasing the external magnetic field, the side arms flip earlier, because for geometrical reasons the central region has higher coercivity (high resistance state, Fig 2.10(b)). Finally, only at a higher field all the magnetic moments are again parallel (Fig 2.10(c)).

I will show in Sec. 6.3 results concerning this kind of devices.

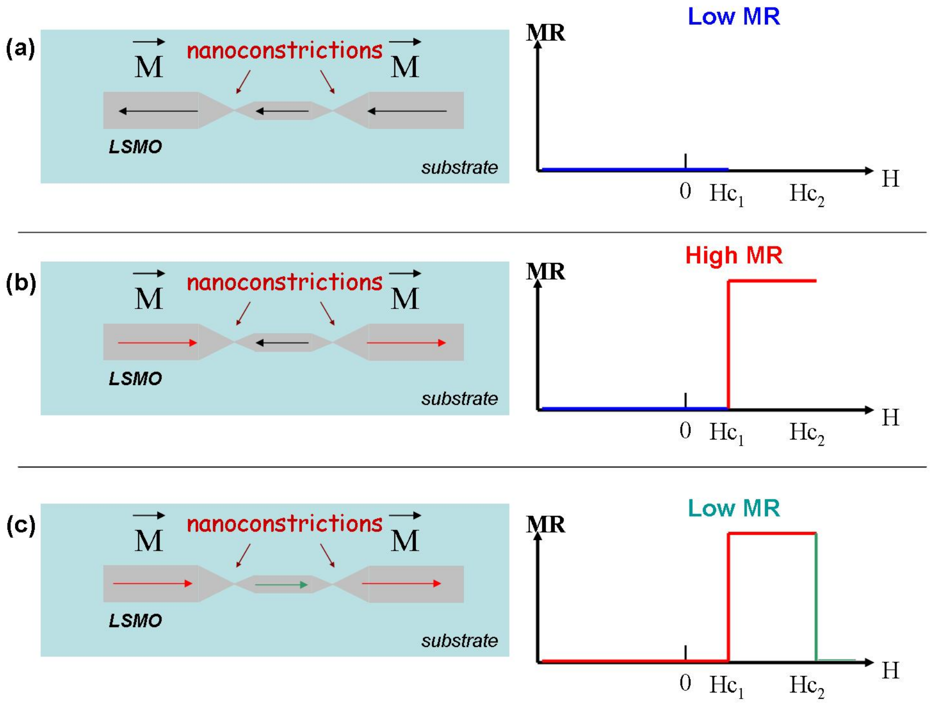

Figure 2.10. Sketch illustrating the domain walls pinning due to the nanoconstrictions. *Low MR* at $H < H_{C_1}$ (*a*); *High MR* at $H_{C_1} < H < H_{C_2}$ (*b*); *High MR* at $H > H_{C_2}$ (*c*).

Chapter 3

Growth of LSMO thin films on STO substrates with different orientation

The final performances of the devices based on manganite films, as discussed in the previous chapter, rely upon the ability to fabricate high quality epitaxial thin films.

There are several methods to grow manganese oxides films. It is well accepted that physical deposition methods, such as sputtering and laser ablation, are the most suitable to achieve high epitaxy and high control of the film growth [11]. Moreover, these techniques allow to preserve the stoichiometry of the chosen single crystal target (in this work $La_{0.7}Sr_{0.3}MnO_3$) during the transfer of the species to the substrates, that is an important task for the growth of complex oxides.

The *sputtering* is the best technique for industrial production due to possibility to cover large areas and for the low costs, but it has a low flexibility because only few deposition parameters can be directly controlled. On the other hand, the *laser ablation* is the most straightforward method that allows to grow different materials even in sequence (multilayer), that is an advantage for application to devices. However, the small deposition area makes at present this technique mostly dedicated to the fundamental research.

I fabricated thin films of *LSMO* onto different single crystal substrates using a sputtering deposition and a *RHEED*-assisted laser ablation at the *CNR-INFM Coherentia* M.O.D.A. laboratory in Naples. Moreover, at the *GREYC - ENSICAEN* laboratory in Caen I fabricated *LSMO* film grown onto *STO* single crystal and buffered silicon substrates using a pulsed laser deposition (*PLD*) technique. First, I devoted particular attention to the deposition conditions, in order to optimize the *LSMO* growth. The *LSMO* films were carefully investigated for their structural, transport and morphological properties, using in-situ and ex-situ techniques, according to the goals of the technological applications described in Chap. 2.

In this chapter, I report on the above mentioned film deposition techniques of manganites and on the characterizations of *LSMO* films grown onto *STO* single crystal substrates.

3.1. Deposition techniques

3.1.1. Sputtering

The principle of the sputtering process can be seen in Fig. 3.1. The target is placed at the cathode. An inert gas such as Ar, is inserted between the electrodes. Oxygen (O_2) is often mixed with Ar during the deposition of oxides. When an electric field in DC or at radiofrequency (RF) (typically $13.56 MHz$) is applied across the electrodes, electrons are emitted from the cathode. The electrons, being accelerated by the field, collide with the gas atoms, generating ions and yet more electrons (secondary electrons). The Ar^+ ions are accelerated towards the cathode and sputter the material that constitutes the target. The trajectories of the electrons are bent by a magnetic field in the so-called *magnetron* sputtering (Fig. 3.1), leading to a certain degree of confinement of electrons around the cathode (target) surface. This effectively increases the probability of ionization of the gas, permitting a higher deposition rate, usually in the range $10^{-2} - 10 nm/sec$ also depending on the target material.

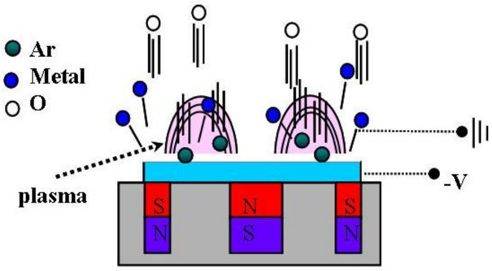

Figure 3.1. Sketch of magnetron sputtering deposition.

As already stated, only a few physical parameters must/can be controlled in sputtering processes. Main are the deposition temperature (T_d), pressure (p_{Ar}, p_{O_2}) and substrate-target distance (D). The *RF* power governes the film deposition rate, but acceptable values are constrained by the total pressure (typically in the range $0.3-0.7mbar$) to self-sustain the plasma formation, and by the geometrical configuration. Finally, the distance target-substrate cannot be considered as an independent parameter too, because it is linked to the plasma configuration.

The optimization of the microstructure and magneto transport properties of manganite films strongly depends on the capability to achieve the correct oxygen stoichiometry [90, 91, 92]. It was demonstrated [44, 93] that the sputtering usually results in some oxygen deficiency. Therefore, post-annealing process in oxygen may be sometimes required.

The sputtering system available in the *CNR - INFM* laboratory in Naples, which I used to fabricate epitaxial *LSMO* films, consists of a vacuum chamber with a base pressure of about $10^{-5}mbar$. The heater on which the substrates are glued by silver paste reaches temperatures up to 900°C. The maximum incident *RF* power is up to $200W$.

3.1.2. Pulsed Laser Deposition

The basic concept of the laser ablation is the following. A pulsed laser beam, with a duration of tens of nanoseconds, pulverizes a target. The particles ejected from the target are highly ionized and energetic and form a plasma with a characteristic shape (Fig. 3.2*(right)*) that is called "ablation plume". The plume condenses on a heated substrate placed in front of the target. The physical quantities that are controlled are the fluence of the laser, the background oxygen pressure, the distance between target and substrate and the temperature of substrates. Both the temperature of the substrate and the oxygen partial pressure influence the size and the shape of the plume, and consequently the deposition rate, while the choice of the energy and the frequency of the laser determine the energy of the atoms and ions that impact the substrate [94].

The *set-up* of the *PLD* system available in the *GREYC* laboratory (Fig. 3.2) is shown in Fig. 3.3. The system consists of two chambers: the deposition chamber and a small chamber for the introduction of the substrates. The deposition chamber is equipped with a multistage rotating carousel on which it is possible to mount up to 5 different targets. The base pressure is about $10^{-6}mbar$ and the maximum temperature reached by the radiative heater is 750°C. The excimer (KrF) laser is a *Lambda Physics / Compex 102* (repetition rate $1-10Hz$, laser energy per pulse $100-400mJ$; pulse duration $30ns$), emitting UV light at $248nm$. The laser beam is focalized by a lens and it reaches the target through an external window. The main advantage of such deposition system is certainly represented by its versatility. Moreover, the system is optimally designed, allowing to get high quality films of several materials, such as manganites, *STO*, *BTO*, *YSZ*, CeO_2, *YBCO*, etc. However, an intrinsic limitation of this system is at present the limitation in the deposition temperature, because some processes may require $T > 750$°C.

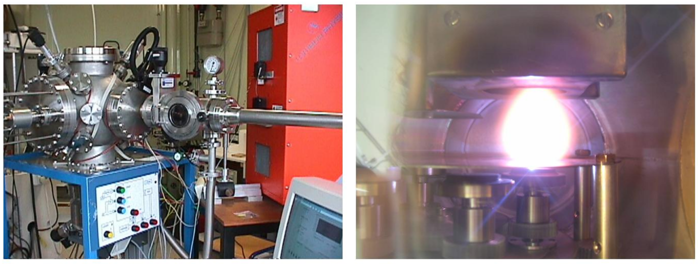

Figure 3.2. Snapshots of the *PLD* system of the *GREYC* laboratory *(left)* and of the plume after the laser beam impact on a $La_{0.7}Sr_{0.3}MnO_3$ target *(right)*.

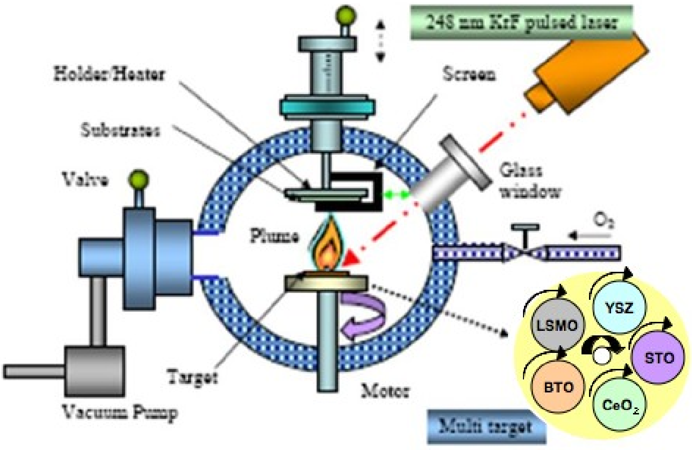

Figure 3.3. Schematic of the *PLD* system utized in the *GREYC* laboratory in Caen.

3.1.3. RHEED-assisted laser ablation

The *RHEED*-assisted laser ablation (also called *laser-MBE*) allows to grow oxide materials usually in low oxygen pressure. Such deposition technique, whose basic principle is the same of the *PLD* described in Sec. 3.1.2, is very suitable for monitoring the film growth during the deposition, achieving a high control of the film growth. The system that I used at the *CNR/INFM Coherentia* laboratory in Naples is equipped with a special High Pressure *RHEED* (described in Sec. 3.1.3.1) allowing the growth monitoring also at high oxygen pressure.

Since the technological development of the oxide based devices results tightly dependent on the control of the film surfaces and the film-substrate interfaces, monitoring *in-situ* the film growth is fundamental to get optimal properties. In such structures, the control of the interfaces at the micro and nano scale results of great relevance, in order to achieve the best performances. Of course, the higher degree of control has a cost in terms of easiness, because the *laser-MBE* is far more complex than standard *PLD*.

The *RHEED*-assisted laser ablation that I used is part of a more complex system (*Modular facility for the Oxides Deposition and Analysis* (M.O.D.A.) (Fig. 3.4) that was designed for the study of surfaces and interfaces of oxide films. For this reason, complex technical upgrades of a basic *PLD* system were introduced. The M.O.D.A. system consists of two main part: a *deposition chamber*, devoted to the fabrication of thin oxide films and an *analysis chamber*, devoted to the invetigation of surfaces of the samples. To prevent any contamination of the deposited films, the base pressure is kept below 10^{-8}*mbar* in the depostion chamber and below $10^{-11} mbar$ in the analysis chamber. For this reason, a complex pumping system is installed. A scheme of M.O.D.A. is shown in Fig. 3.5.

Figure 3.4. Picture of the *CNR/INFM Coherentia* M.O.D.A. laboratory in Naples.

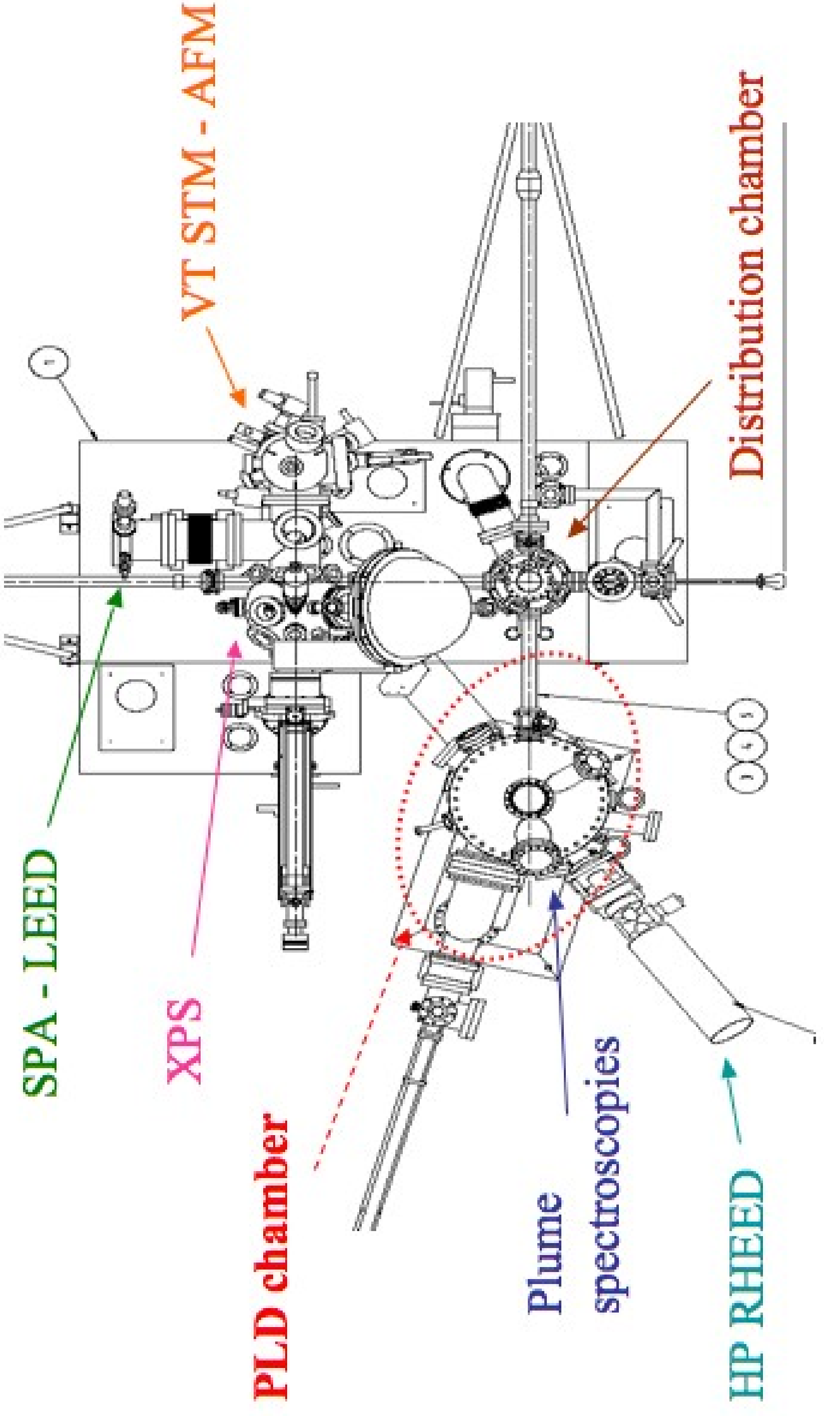

Figure 3.5. Schematic of the *CNR/INFM Coherentia* M.O.D.A. system (top view).

3.1.3.1. M.O.D.A. deposition chamber and HP-RHEED

The *deposition chamber* (Fig. 3.6) is equipped with a laser (*Coherent COMPEX 200*, repetition rate $1 - 50Hz$, laser energy per pulse $100 - 600mJ$; pulse duration $10ns$, spectral width $1pm$), a multistage rotating carousel on which it is possible to mount up to 6 different targets, a radiative heater capable to reach a temperature up to 1100°C and the *High Pressure Reflection High Energy Electron Diffraction (HP-RHEED)* for monitoring in-situ the film growth [95].

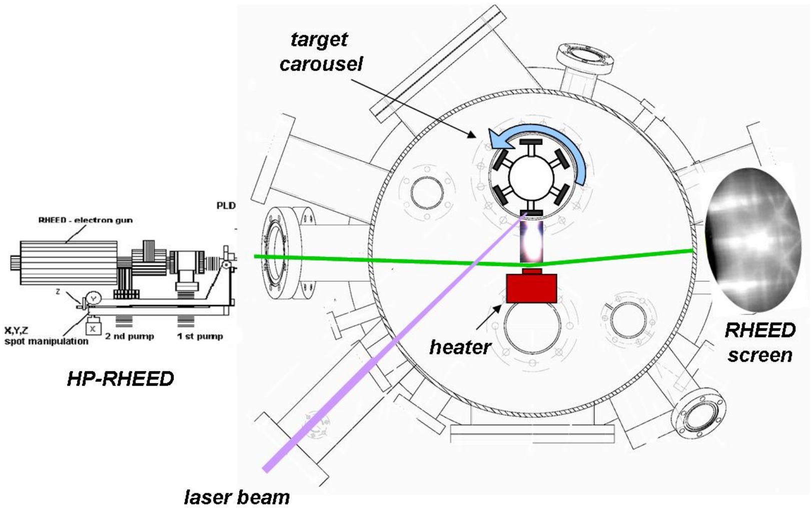

Figure 3.6. Scematic of the *deposition chamber* of the M.O.D.A. system.

HP-RHEED This technique is used as an in-situ monitoring technique to study the growth during deposition providing information of the periodic arrangement of the surface atoms. The *HP-RHEED* consists of an electron beam focused on the sample surface at grazing angle (focus spot $\leq 100\mu m$; beam divergence $\leq 0.2mrad$, working distance $10cm$) and a fluorescent screen on which the reflected electrons are collected. Since the oxide deposition requires high oxygen pressure (up to $0.5mbar$), high energy electrons are required ($30keV$, $1.20A$) and their path in the chamber is as short as possible. Moreover, the source must be kept at lower pressure, resorting to a differential pumping. The fluorescent screen that collects the reflected electrons is placed very close to the substrate [96, 97] (Fig. 3.6). It must be noted that, in order to have an optimal alignment of the electron beam on the sample surface, the heater is provided with 5 position degrees of freedom, i.e. x, y, z, azimuth and tilt, remote controlled. The wavelength of the electron is

$$\lambda_{el}(\text{Å}) = \left(\frac{h^2}{2m_e eE}\right)^{-\frac{1}{2}} \sim 0.07\text{Å} \tag{3.1}$$

at $30keV$, that is lower than in standard *RHEED* setup operating at $\sim 10keV$. In spite of the enhanced diffusion of electrons by the ambient gas and of the reduced dimensions of diffraction patterns due to the adopted geometry, the *HP-RHEED* results on excellent tool for investigation, as I will demonstrate in the following.

In standard *XRD* geometry, the x-ray interacts weakly with matter, and penetrates $1-10\mu m$ underneath the surface, so that a large number of layers contribute to the diffraction. The 3 dimensional periodicity of the crystal determines thus well defined Bragg condition. This results in a typical spot pattern of the reciprocal space. On the contrary, at low angle, the electrons are scattered within a depth of about one atomic layer, due to the strong electron-electron interaction. Therefore, the *RHEED* is a probe of the surface structure of the sample. The lack of perpendicular periodicity relaxes the constraints on the perpendicular scattering vector ($K_\perp$) (Fig. 3.7). The complete indetermination of the reciprocal vector perpendicular to the crystal surface results in the typical rod pattern, where only the parallel component of the reciprocal vector ($K_\parallel$) is quantized. In Fig. 3.8*(left)* the typical rods features recorded on the screen of the M.O.D.A. system for a *LSMO* grown onto (001) *STO* single crystal are shown. In Fig. 3.8*(right)*, the behaviour of the intensity of the specular spot (i.e., the $(0,0)$ peak) is recorded as a function of deposition time, quantified by the number of laser shots. The oscillations indicate that the surface has the highest reflectivity when the surface structure is perfect, that is when a complete atomic layer is deposited, while lower values are achieved for incomplete, disordered layers. Such a periodic *RHEED* intensity oscillations are a well known example for the observation of a layer-by-layer mode in a crystal growth experiment and this can be very useful when one want to deposit multilayer having a direct control of the number of the cells of each layer. However, if the film surface is rough spots instead of rods appear, indicating a 3D crystal ordering even in only few monolayers (*ML*s).

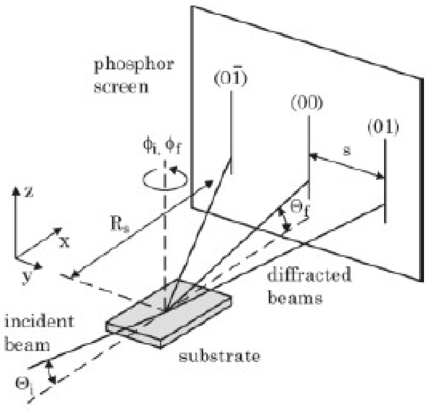

Figure 3.7. Schematic view of the *RHEED* geometry. Θ_i (Θ_f) and ϕ_i (ϕ_f) are the incident and azimuthal angles of the incident (diffracted) beam. R_S is the distance between substrate and phosphor screen and s the distance between the diffraction spots or streaks (after [96]).

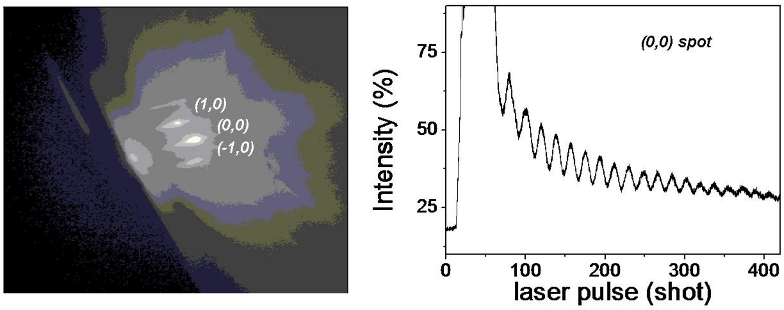

Figure 3.8. Typical *RHEED* pattern *(left)* and oscillation on the $(0,0)$ spot *(right)* for a *LSMO* film grown onto (001) *STO* single crystal.

3.1.3.2. M.O.D.A. analysis chambers

The *analysis chambers* (Fig. 3.5) are devoted to *in-situ* surface characterizations. The sample is mounted on a stage (sample holder) that can reach temperatures up to 900°C and can be moved through 3 separate chambers. The first chamber is equipped with a x-ray gun and a collector emisphere for the *Photoemitted* electrons that provides the *X-ray Photoemission Spectroscopy* (*XPS*). The second chamber rooms a *Spot Profile Analysing - Low Energy Electron Diffraction* (*SPA-LEED*) (Fig. 3.9*(a)*). Finally the morphology and the electronic characterization of the sample surface can be investigated by a *Scanning Probe Microscopy* (*SPM*) in the third chamber.

The low energy electron diffraction is one of the most useful surface science techniques [98]. The *SPA-LEED* mounted in M.O.D.A. consists of an electron gun, that generates low energy electrons (current $50pA - 500nA$; source voltage $100 - 150eV$, leading to $\lambda_{el} \sim 0.1nm$ from Eq. 3.1), an electrostatic unit, that provides the deflection of the incident and diffracted electrons and a channeltron single electron detector (Fig. 3.9*(a)*). The angle between incident and reflected beams stays constant at 4° as determined by the angle between gun and detector. While the incident angle is changed, the Ewald sphere is rotated around the origin of reciprocal space. As a result the diffraction pattern falls on a sphere with the origin at (000) and twice the diameter of the Ewald sphere. Scanning the incident angle of the elctron beam results in a simultaneous variation of the angle under which diffracted electrons are recorded. This variation of both the incident and the exit angle of the electrons results in a very special scanning mode in reciprocal space.

To conclude, the position of the diffraction spots is used to determine lateral lattice constants [98], step heights and the strain state of films with a precision of about $0.01nm$. With the knowledge of the spot profile we could also determine island and domain size distributions and correlation functions of arbitrary surface defects and atomic arrangement in the surface unit cell (*reconstruction*) (see Sec. 1.6).

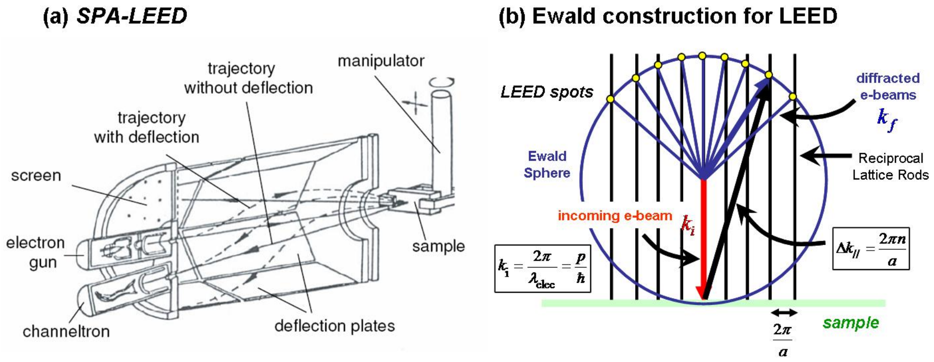

Figure 3.9. Schematic of the *SPA-LEED (a)* and Ewald construction for *LEED (b)*.

3.2. Deposition and characterization of LSMO films

3.2.1. LSMO films deposited by sputtering

I deposited *LSMO* films in the *CNR - INFM Coherentia* laboratory in Naples by *RF* magnetron sputtering (see Sec. 3.1.1) from a *LSMO* target on different single crystal substrates, such as *STO*, *LAO*, *NGO* and *MgO* with different crystal orientations, i.e. (001), (110), including crystals with vicinal cut. The deposition conditions optimized for the growth of *LSMO* onto *STO* substrates are the following. The substrates were heated up to 840°C and kept in vacuum for 30min before film deposition. The sputtering atmosphere was a mixture of argon and oxygen, with equal partial pressures. The deposition rate was $0.03nm/s$ at $100W$ *RF* incident power. After deposition, the chamber was slowly vented in O_2 up to $400mbar$. The cooling was completed in about $2h$ [93].

Careful *Rutherford BackScattering* (*RBS*) analyses were performed[1] on thin samples deposited on *MgO* substrates at different pressure, in order to check the stoichiometry of the deposited samples [93]. The choice of *MgO* (001) substrates guarantees that no contribution due to the substrate overlaps film peaks. (Fig. 3.10). At $P_{tot} = 0.67 mbar$, the target stoichiometry is reproduced in the films within the experimental error (5%) (inset in Fig. 3.10).

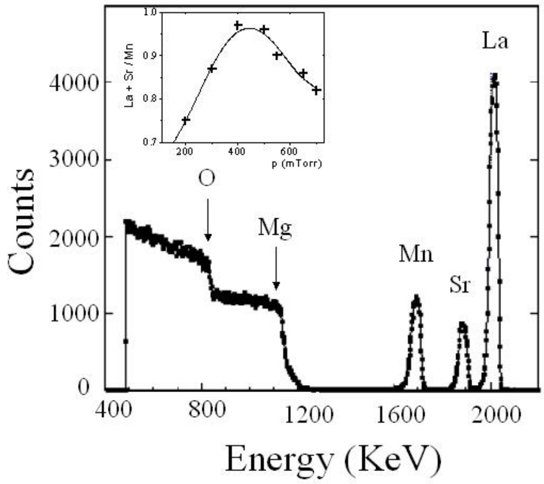

Figure 3.10. Rutherford Backscattering (*RBS*) analyses of *LSMO* sputtered films deposited on *MgO* (001) substrates [93].

3.2.1.1. Structural properties

I carried out x-ray diffraction measurements for the structural investigation of sputtered samples. *XRD* analyses have been performed by using a standard two-axes diffractometer in *Bragg-Brentano* focusing geometry [99].

I resorted to rocking curves (ω-scans) and grazing incidence x-ray reflectivities to check the sample quality. A prove of the high crystal quality is given by the rocking curves of the symmetric reflections, that show a *FWHM* only limited by the diffractometer resolution (Fig. 3.11). Moreover, the $\theta - 2\theta$ plots are characterized by clear oscillations at low angle (Fig. 3.12*(left)*). Such interference fringes demonstrate low surface roughness. A typical $\theta - 2\theta$ plot around the (002) reflection is shown in Fig. 3.12*(right)*. This kind of checks proves that high quality samples with very similar properties were routinely obtained.

---

[1] at the *T.A.S.C. CNR - INFM* laboratory in Trieste

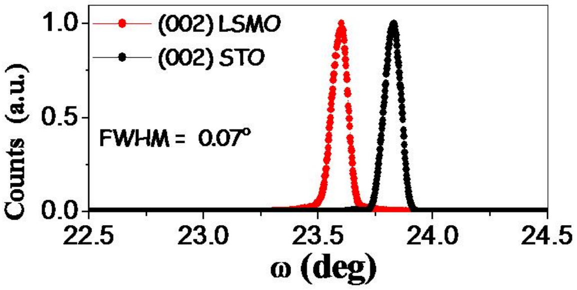

Figure 3.11. ω-scan around the (002) reflection of the *LSMO* film grown on (001) *STO* substrate.

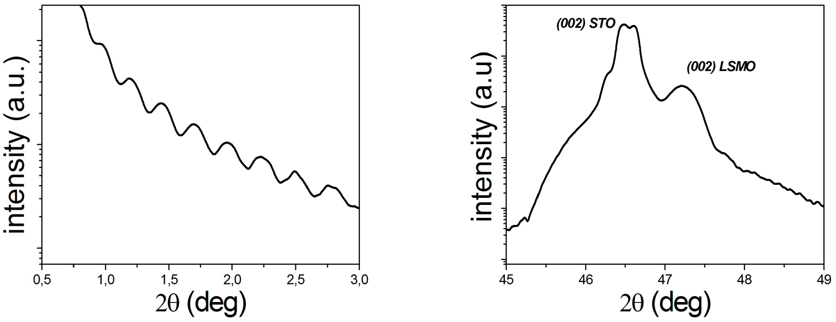

Figure 3.12. Grazing angle X-ray reflectivity *(left)* and $\theta - 2\theta$ plot around the (002) crystallographic reflection *(right)* of a *LSMO* film grown on (001) *STO*. The splitting of the (002) *STO* peak is due to the *Cu* $K\alpha_2$.

3.2.1.2. Morphology

The morphological analysis of the *LSMO* films grown on (001) and (110) *STO* were performed by *STM*. The investigated samples exhibit smooth surfaces, with a roughness of about $1 - 2nm$.

In the case of the *LSMO* ($10nm$ thick) deposited on (001) *STO*, some sharp structures were imaged. The *STM* topography reported in Fig. 3.13*(a)* shows rectangular shaped growth structures, partially overlapping, on a scale of few nanometers. Fig. 3.14*(a)* shows a topographic image taken on a *LSMO* thin film grown on (110) *STO*. The surface has very regular features, exhibiting terraces with parallel step edges. The preferential orientation of the steps runs along the $[001]_{STO}$ direction. From the line profile (Fig. 3.14*(b)*), the average terrace width is about $50nm$, while the step height is of the order of some nanometers. On each single structure terrace, the average surface roughness is low (only few Å). The good surface quality of these samples is also confirmed by the atomic resolution that was occasionally achieved (Fig. 3.14*(c)*).

Note that it was necessary to expose the samples to air to perform *STM*, that was carried in this case in inhert atmosphere. As the measurements indicate, the samples are reasonably smooth even though *PLD* samples (see Figs. 3.23, 3.32) have clearly superior properties under this respect.

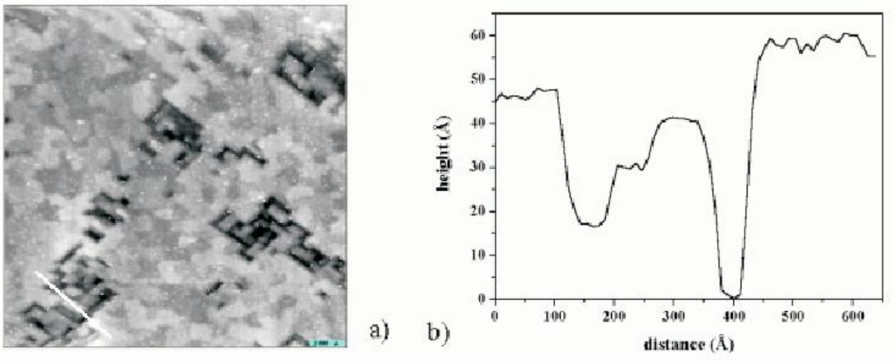

Figure 3.13. *(a)* $200nm \times 200nm$ *STM* topographic image ($V = 2V$; $I = 70pA$) on a very thin *LSMO* film on (001) *STO*; *(b)* height profile along the line reported in the image *(a)* [42].

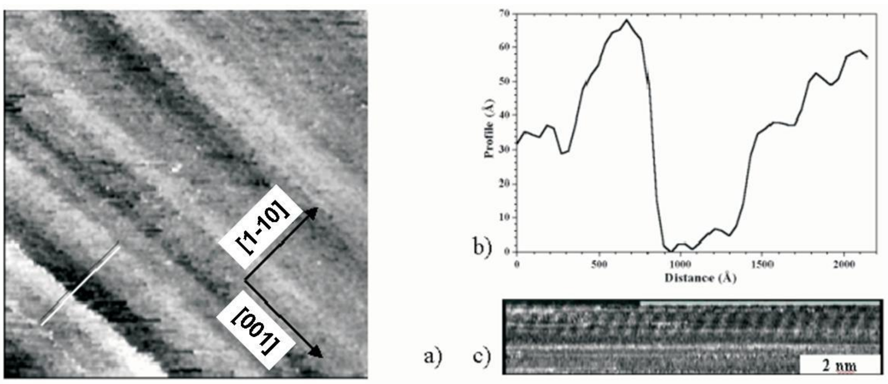

Figure 3.14. *(a)* $800nm \times 800nm$ *STM* topographic image ($V = 1V$; $I = 200pA$) on a very thin *LSMO* film on (110) *STO*; *(b)* height profile along the line shown on the image; *(c)* sign of atomic resolution, indicating the high quality of the sample [42].

3.2.2. LSMO films deposited by PLD

3.2.2.1. Deposition conditions

I fabricated *LSMO* samples by *PLD* in the *GREYC* laboratory (see Sec. 3.1.2). In order to achieve high quality crystal structure, high *MIT* temperature, low resistivity and smooth surfaces I first optimized the deposition condition for the *LSMO* growth on (001)-oriented *STO* substrate varying the growth temperature (T_{dep}), the oxygen pressure (p_{O_2}) and the laser energy (EGY). The laser pulse energy, controlled by an internal calorimeter (and checked systematically by an external calorimeter), was varied in the range $250 - 270mJ$. The beam rate was fixed at $3Hz$, the spot size on the target was $2 \times 1mm^2$ and the *LSMO* deposition rate on *STO* was $\sim 0.006nm/sec$. As we can see in Fig. 3.15, ranging the oxygen pressure from $0.20mbar$ to $0.40mbar$, the *LSMO* *c-axis* becomes smaller. The maximum resistivity temperature (T_P) and the lowest resistivity (ρ_{300K}) value occur for $T_{dep} = 720$°C and $p_{0_2} = 0.35mbar$ (Fig. 3.15).

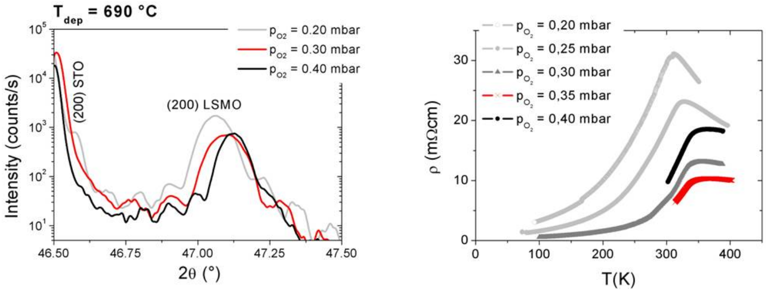

Figure 3.15. $\theta - 2\theta$ scans (*left*) and $\rho(T)$ measurements (*right*) of *LSMO* films ($75nm$ thick) deposited onto (001) *STO* substrates for different p_{O_2} at $T_{dep} = 690\,^{\circ}C$.

The *LSMO c-axis* becomes smaller also by increasing the deposition temperature from 690°C to 730°C, . The maximum resistivity temperature (T_P) and the lowest resistivity (ρ_{300K}) value occur for $T_{dep} = 720$°C and $p_{O_2} = 0.35mbar$ (Fig. 3.16).

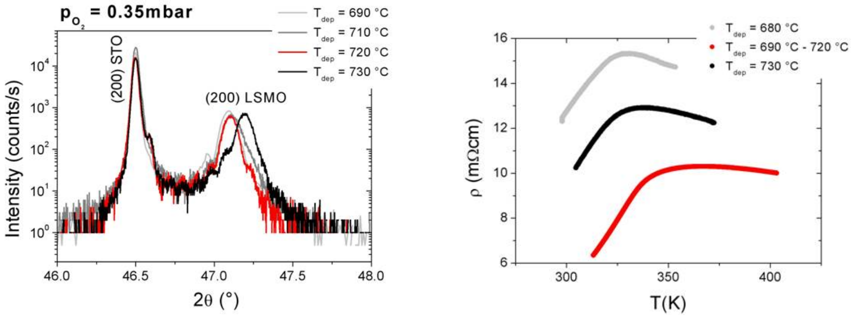

Figure 3.16. $\theta - 2\theta$ scans (*left*) and $\rho(T)$ measurements (*right*) of *LSMO* films ($75nm$ thick) deposited onto (001)-*oriented STO* substrates for different T_{dep} at $p_{O_2} = 0.35mbar$.

Tab. 3.1 lists the resistivities (ρ), the T_P and the *c-axis* of *LSMO* thin films ($75nm$ thick) grown on (001) *STO*.

T (°C)	pO2 (mbar)	ρ (mΩ cm) @ 300K	Tp (K)	c-axis (nm)
690	0,2	29,35	311	0,3859
	0,3	10,19	344	0,3856
	0,4	10,26	363	0,3854

pO2 (mbar)	T (°C)	ρ (mΩ cm) @ 300K	Tp (K)	c-axis (nm)
0,35	690	4,72	363	0,3857
	710	9,52	343	0,3855
	720	7,00	352	0,3855
	730	10,2	338	0,3849

Table 3.1. Resistivities, T_P and c-axis of *LSMO* thin films, $75nm$ thick, grown on (001) *STO* .

Magnetization vs. temperature ($M(T)$) measurements[2] were performed using a *SQUID* magnetometer in a magnetic field of $5kOe$ in zero field cooled (*ZFC*) configuration. The

---

[2] These measurements were performed at the *CRISMAT - ENSICAEN* laboratory in Caen.

measurements reveal a magnetic moment per Mn site close to the ideal theoretical expectation, i.e. $M = 3.7\mu_B$ per Mn site in the case of the $LSMO$ sample grown at 720°C (Fig. 3.17).

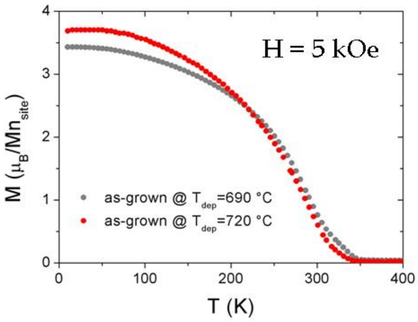

Figure 3.17. $M(T)$ measurements on $LSMO$ films deposited onto STO (001)-oriented substrates at 690°C (*grey line*) and 720°C (*red line*).

In Fig. 3.18 I show the resistance vs. temperature and the magnetization vs. temperature curves, indicating a MIT temperature above $300K$ and an optimal value of $\sim 3.7\mu_B$ of the magnetization at $8K$.

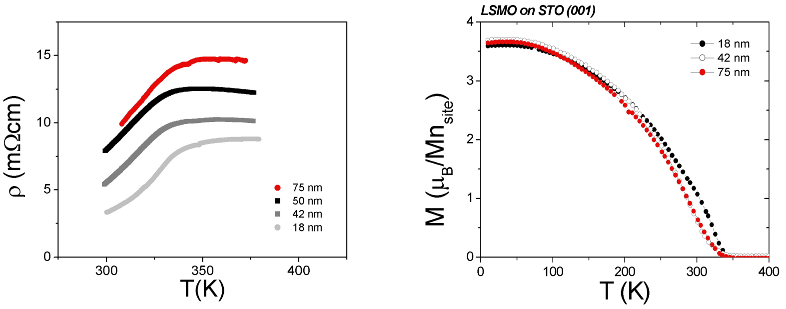

Figure 3.18. Resistivity vs. temperature (*left*) and magnetization vs. temperature (*right*) of $LSMO$ film deposited on STO (001)-oriented substrate with different thickness.

As already discussed (Sec. 1.5, Fig. 1.16), the choice of the thickness can be crucial for applications. Fig. 3.19 shows the MIT temperature (T_{MI}) vs. thickness. The T_{MI} is depressed below $10nm$ thick $LSMO$ while it tends to the bulk value for thicker films. However, it is worth to note that the reduction of the T_{MI} is consistent with other published data and with the theoretical expectations [11] (Fig. 3.19).

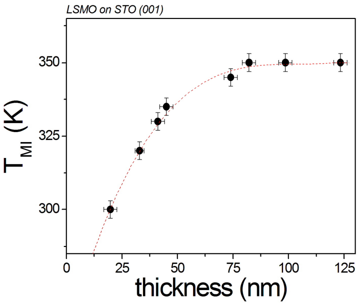

Figure 3.19. T_{MI} versus thickness for $LSMO$ films grown onto (001) STO.

3.2.2.2. Vicinal LSMO

I deposited two series of *LSMO* thin films of thicknesses $42nm$ and $75nm$, onto commercially available vicinal *STO* (001) substrates. The vicinal angles (θ_{vic}) were 2°, 4°, 6°, 8°, and 10°, inducing the formation of the steps along the [110] crystallographic direction (Fig. 3.20).

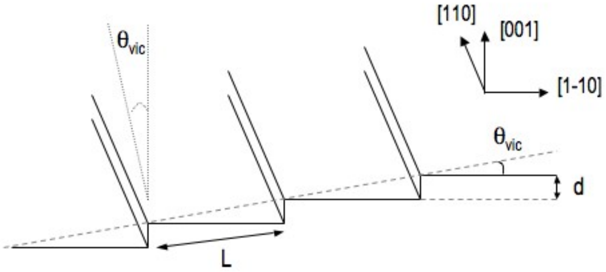

Figure 3.20. Sketch of the vicinal (001) $SrTiO_3$ substrate with the vicinal angle θ_{vic} toward the ($1\bar{1}0$) crystallographic direction.

I used the deposition conditions optimized for the growth of *LSMO* on standard (001) *STO* substrates (see Sec. 3.2.2). These values gave excellent single-crystalline films also in this case, as judged by the *XRD* study. I checked that the offset angle of the *LSMO* cell was equal to the substrate vicinal angle within 0.05° for all the considered angles. This means that the crystallographic *LSMO* growth orientation was always parallel to the *out-of-plane* axis (along the [001] crystallographic direction) for both film thicknesses considered. The measured *FWHM* around the (002) *LSMO* of the rocking curves was in the 0.23° - 0.31° range (Fig. 3.21*(a)*). These values can be compared to 0.23° which was typical for *LSMO* films of comparable thickness deposited on (001) *STO* substrates. The in-plane alignment of the layers is demonstrated by the ϕ-scan measurements around the (002) reflection (Fig. 3.21*(b)*).

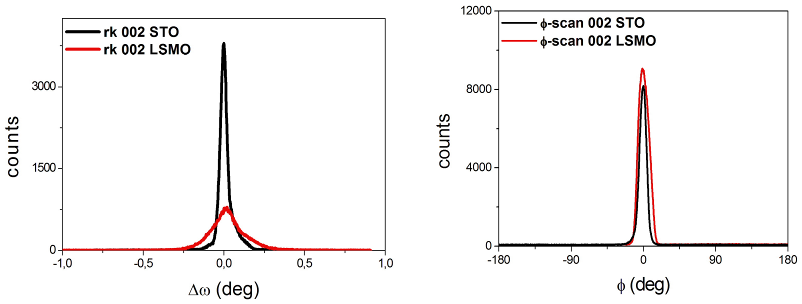

Figure 3.21. Rocking curve (a) and $\phi - scan$ (b) around the (002) peaks of the $42nm$ thick *LSMO* film with a vicinality of 10°.

Typical $\theta - 2\theta$ patterns are shown in Fig. 3.22.

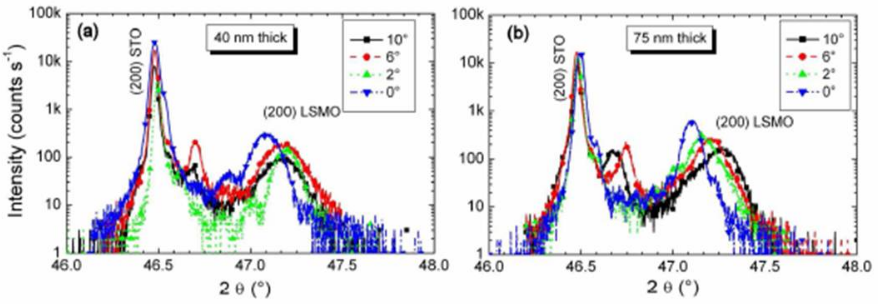

Figure 3.22. *XRD* $\theta - 2\theta$ *patterns measured using an offset value on* θ. No peaks could be recorded if no offset was added thus confirming that the *LSMO* films grew with their (001) axis coincident with the (001) axis of the substrate: (*a*) 40*nm* thick series, (*b*) 75*nm* thick series [100].

One can note the satellite peaks around the *LSMO* (002) peak, which give an indication of the low roughness of the films. The average *out-of-plane* parameter of the vicinal *LSMO* films is 0.3859*nm*, which corresponds to a lattice mismatch with *STO* of 1.18×10^{-2}. It has to be compared to the value of 0.3865*nm* (i.e. a lattice mismatch of 1.02×10^{-2}), which is typically measured on 40*nm* thick *LSMO* films on *STO* (001) substrates (Tab. 6.6). This means that the *LSMO* cell shows an higher *out-of-plane* compression in the case of vicinal films ($\varepsilon_{[001]} = -0.00361$) than in the case of *LSMO* on standard *STO* (001) ($\varepsilon_{[001]} = -0.00207$), while the in-plane strain component is the same ($\varepsilon_{[100]} = 0.00826$), leading to a cell volume expansion of $\sim 1.2\%$. Finally, the bulk strain and the biaxial strain, as defined in Sec. 1.5 by the Eqs. 1.17 and 1.18, are $\varepsilon_B = 0.00415$ and $\varepsilon^* = -0.00609$, respectively.

3.2.2.3. Morphology

I investigated the morphology of the films performing *AFM* and *STM* measurements.

The *LSMO* films deposited onto (001) *STO* substrates in Caen are very smooth. They show a roughness of the order of the lattice parameter. Even at 75*nm* film thickness, as shown in Fig. 3.23*(a)-(b)*, the root-mean-square roughness (*RMS*) on $5 \times 5\mu m^2$ area, scanned in tapping mode by *AFM*, is 0.130*nm*. Resorting to scanning tunnel microscopies on smaller area of $500 \times 500nm^2$, clear terraces 80*nm* wide indicate a *step-flow* like growth (Fig. 3.23*(c)-(d)*). Note in this respect the difference with the analogous measurements performed on sputtered samples (Fig. 3.13) that indicate on the contrary a significative step bounching.

Two batches of *LSMO* films, 75*nm* and 42*nm* thick, deposited onto (110) *STO* substrate were also analyzed by *AFM* and *STM*. In Fig. 3.24*(a)-(b)* I show *AFM* $2 \times 2\mu m^2$ images over which the calculated *RMS* is 0.373*nm* and 0.224*nm* for the thicker and for the thinner thick film, respectively. Note the typical elongated shape of the (110) *LSMO* grains that is typical of this orientation growth (Fig. 3.24*(c)-(d)*).

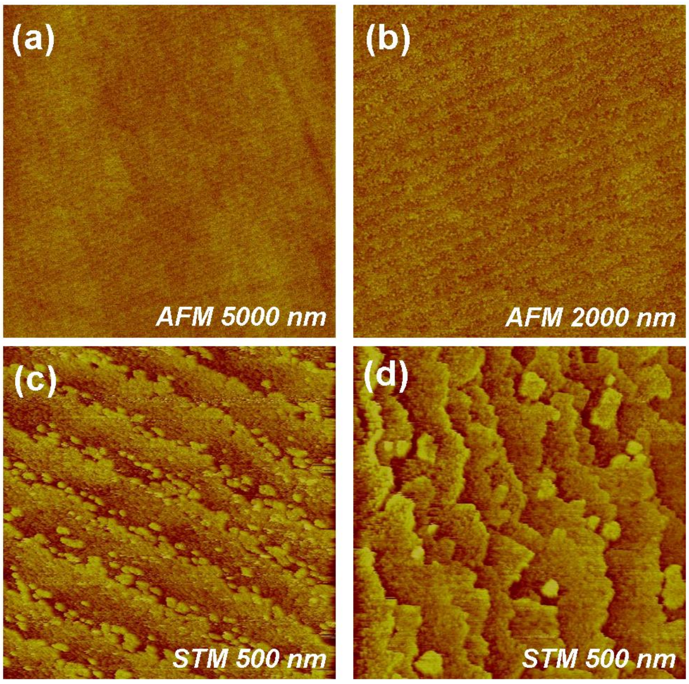

Figure 3.23. $5 \times 5\mu m^2$ *(a)* and $2 \times 2\mu m^2$ *(b)* *AFM* topographies of the surface of the *LSMO* ($75nm$ thick) deposited onto (001) *STO*; $500 \times 500nm^2$ *STM* topography ($V = 1V$; $I = 100pA$) of the surface of the *LSMO* $75nm$ *(c)* and $18nm$ *(d)* thick deposited onto (001) *STO*. The average width terraces is $80nm$.

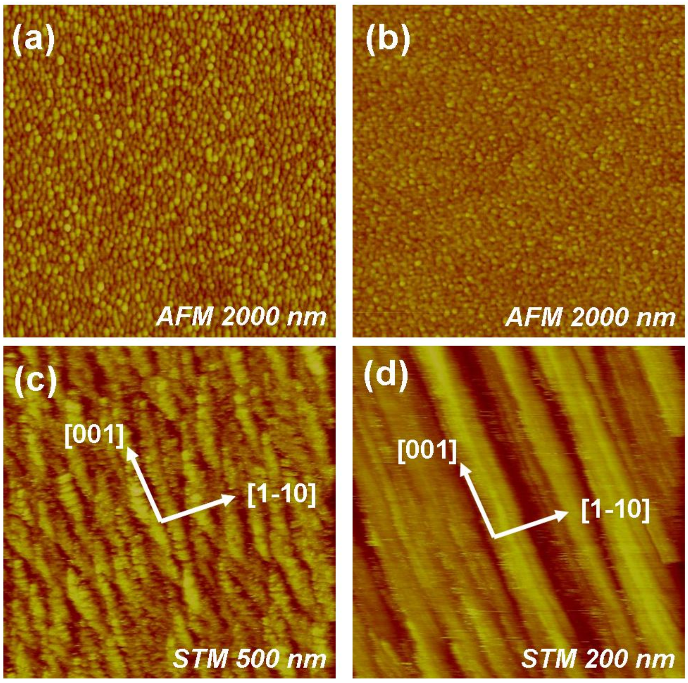

Figure 3.24. $2000 \times 2000nm^2$ *AFM* topographies of the surface of *LSMO* $75nm$ *(a)* and $42nm$ *(b)* thick films deposited onto (110) *STO* substrate; $500 \times 500nm^2$ *(c)* $200 \times 200nm^2$ *(d)* and *STM* topographies ($V = 1V$; $I = 100pA$) of the *LSMO* $42nm$.

The *LSMO* films with thicknesses of $42nm$ and $75nm$, grown onto vicinal *STO* (001) substrates, are very smooth and show regular step-terrace structures corresponding to the replication of the substrate vicinal surface.

The *RMS* roughness, as measured in the $2\mu m \times 2\mu m$ *AFM* images, is in the $0.130nm$ - $0.580nm$ range for all films (Tab. 3.2). These values have to be compared to the typical value $0.130nm$ that was obtained for non-vicinal *LSMO* films. Note that for angle below 2° the thickness has no clear effect on roughness, but above 4° the $75nm$ thick films are systematically rougher than the $42nm$ series for each angle. In the case of the vicinal 10°, the *RMS* roughness is $0.264nm$ for the $42nm$ thick film and $0.579nm$ for the $75nm$ thick film (Fig. 3.26).

In the case of *LSMO* deposited on standard (001) *STO* substrates, I systematically observed large steps (about $80nm$ wide) suggesting a *step-flow growth* mechanism and reproducing the very small miscut (of the order of 0.1°) of the substrates (see for example Fig. 3.25). For the *LSMO* $42nm$ thick deposited on 2° vicinal substrates, no step are observed by *AFM* (Fig. 3.25). As expected, above 4°, I observed that the step width decreased with increasing vicinal angle, i.e. $60nm$, $50nm$, $36nm$, $32nm$ for 4°, 6°, 8°, and 10°, respectively (Tab. 3.2), and for the two considered thickness values, the step width did not depend significantly on the thickness (Fig. 3.26).

I also performed *STM* measurements of both series of different thickness for various vicinal angles. $500nm \times 500nm$ images replied the *AFM* images, demonstrating the accuracy of such measurements and the quality of the *LSMO* surface (Fig. 3.27). It is worth to note that very regular seps were recorded by *STM* even in the case of the 2° vicinal angle where no steps could be observed by *AFM*.

Concluding, the *AFM* and *STM* images confirm the *XRD* study, demonstrating the homomorphic growth on the vicinal substrates, up to relatively high thicknesses ($75nm$). Published data on vicinal *LSMO* films had concerned so far only ultrathin films ($12nm$ - $25nm$) [24, 83].

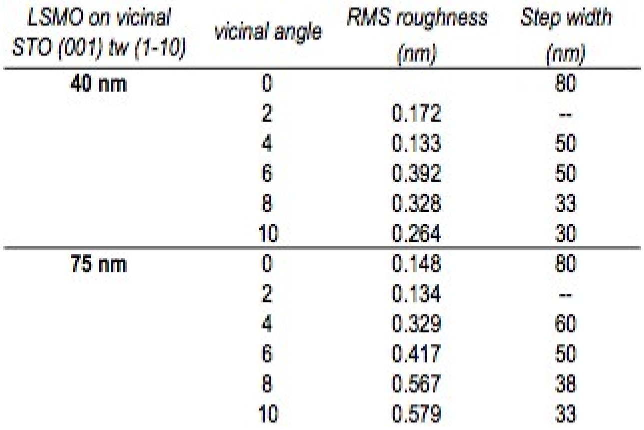

LSMO on vicinal STO (001) tw (1-10)	vicinal angle	RMS roughness (nm)	Step width (nm)
40 nm	0		80
	2	0.172	--
	4	0.133	50
	6	0.392	50
	8	0.328	33
	10	0.264	30
75 nm	0	0.148	80
	2	0.134	--
	4	0.329	60
	6	0.417	50
	8	0.567	38
	10	0.579	33

Table 3.2. *RMS* roughness and step width of the vicinal *LSMO* films of different angle and of different thickness.

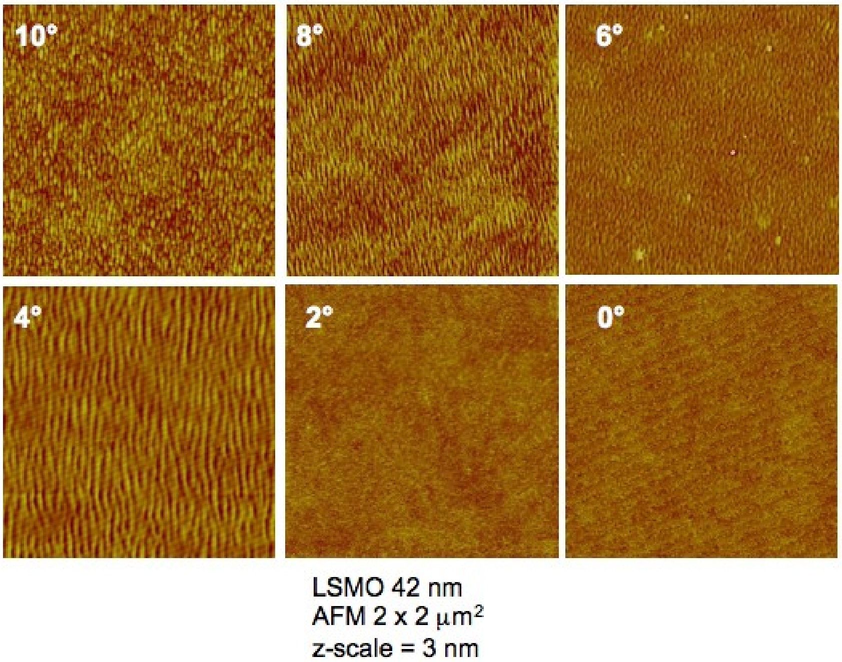

Figure 3.25. $2\mu m \times 2\mu m$ AFM images recorded in *tapping* mode ($z - scale = 3nm$) of $42nm$ thick $LSMO$ films for various vicinal angles.

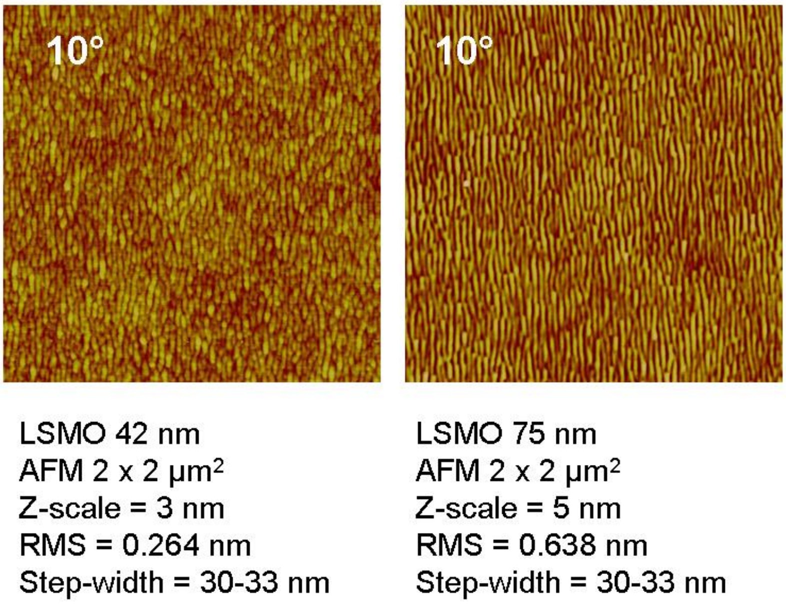

Figure 3.26. $2\mu m \times 2\mu m$ AFM images recorded in *tapping* mode of the vicinal 10° $LSMO$ films, $42nm$ (*left*) and $75nm$ (*right*) thick.

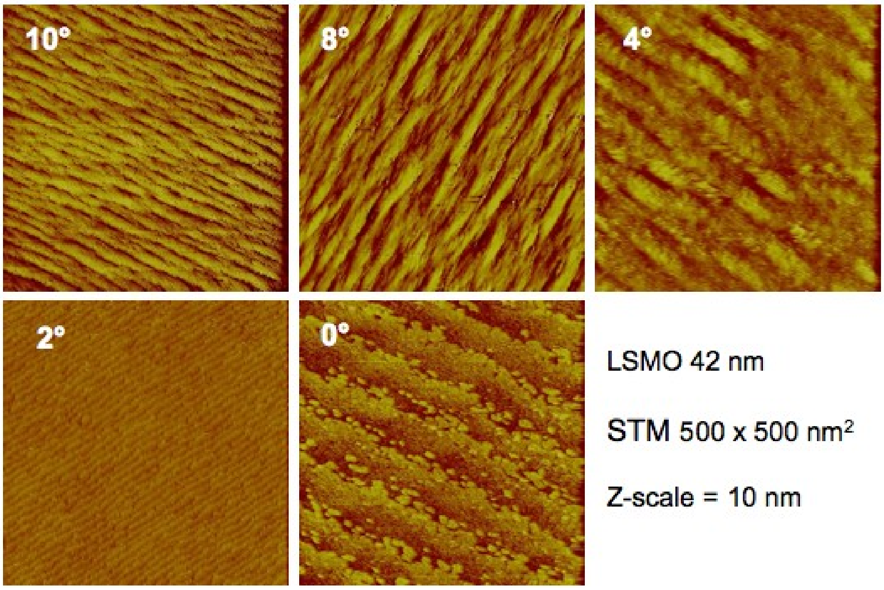

Figure 3.27. $500nm \times 500nm$ STM images ($V = 1V$; $I = 100pA$) of $42nm$ thick $LSMO$ films for various vicinal angles.

3.2.3. LSMO films deposited by RHEED-assisted laser ablation

In this section, I report on the study of the *LSMO* thin films grown onto *STO* single crystal substrates by the *RHEED-assisted laser deposition* technique at the M.O.D.A. laboratory in Naples (see Sec. 3.1.3). The substrate and film surface characterization were obtained *in-situ* without breaking of the *UHV* conditions, thus avoiding the surface contamination. Otherwise, structural and transport measurements were performed *ex-situ.*

For the *LSMO* growth, the laser energy and the repetition rate were fixed at $400mJ$ and at $2Hz$, respectively. The growth temperature was optimized at 800°C, while the oxygen pressure was $0.1mbar$. The target-substrate distance was $40mm$. After the growth, samples were cooled to room temperature in about 20°C/min in the same atmosphere. No post-growth annealing treatments, either in situ or ex situ, were carried out on the films in this case, at difference from the case of sputtering and *PLD* in Caen.

3.2.3.1. Growth control

The films growth was always monitored using the *HP-RHEED* (Sec. 3.1.3). Typical *RHEED* oscillations performed during the *LSMO* growth on a (001) *STO* substrate at the previously mentioned condition are shown in Fig. 3.28. A *STO* thin layer was routinely deposited in order to improve the substrate surface before the growth of the *LSMO.* Each *STO* deposition was interrupted once the layer was fully completed, i.e. on a maximum of intensity of the *RHEED* oscillations. The separations between the partial maxima in Fig. 3.28 indicate that 26 laser shots are necessary to build one *LSMO* unit cell (therefore, the *LSMO* deposition rate is $0.0037nms^{-1}$). The *LSMO* growth shows an initial layer-by-layer and a consequent step-flow growth dynamic. After completing each deposition the *RHEED* intensity increases. Such exponential recovery signal is proportional to $1 - exp\left\{\frac{t}{\tau}\right\}$ where $\tau = \frac{\ell^2}{2D}$ and ℓ and $2D$ are the diffusion length and the surface diffusion constant, respectively [96]. Since, we found $\ell \leq \zeta$ where ζ is the step width, the typical *LSMO* growth in the above mentioned conditions follows a *layer-by-layer* dynamic.

Fig. 3.29*(a)* and Fig. 3.29*(b)* show the specular spot *RHEED* patterns of typical *STO* (001)-oriented single crystal substrate and *LSMO* film deposited on it, respectively. The *RHEED* patterns of all the deposited films showed *2D* character, that is streaky patterns.

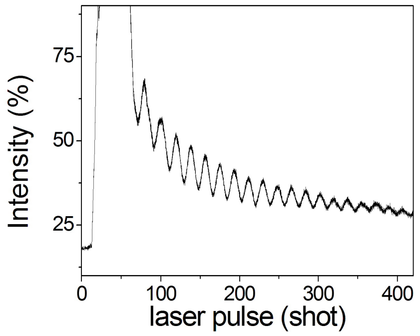

Figure 3.28. *RHEED* intensity oscillations of the $(0, 0)$ reflection during the *LSMO* growth on (001) *STO.*

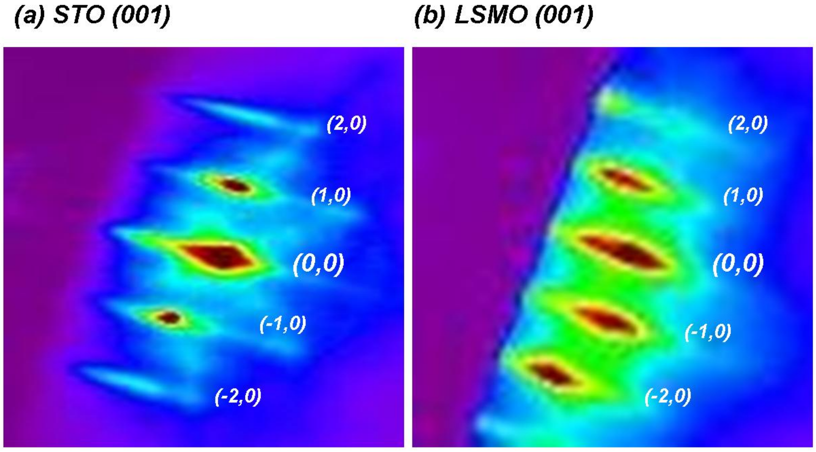

Figure 3.29. *RHEED* patterns of the crystal surface structure of (001) *STO (a)* and of the *LSMO* film deposited onto (001) *STO (b)*.

3.2.3.2. Surface analyses

The surfaces of the *STO* substrates and of the deposited *LSMO* films were carefully investigated by *LEED* and *STM*. The *LEED* measurements of a (001) *STO* substrate and of the *LSMO* film grown on it are reported in Fig. 3.30. The reciprocal lattice observed by the *LEED* measurements yields a square direct lattice with 3.9Å spacing, that corresponds to the unit cell of the *STO*. The same happens in the case of *LSMO*, and it is found that the lattice parameters are equal within the experimental errors. The surface of the (001) *STO* substrate before the deposition did not show any reconstruction (Fig. 3.30*(left)*). Note that the *STO* surface reconstructions have been extensively studied and they are correlated to the thermal treatments. After the *LSMO* deposition, the film surface was not reconstructed, showing an ***in-plane*** lattice parameter of 3.9Å in both crystallographic direction, in agreement with what was calculated resorting to *ex-situ* x-ray diffraction (Fig. 3.30*(right)*). Fig. 3.31 shows, analogously, the *LEED* measurements of the surface of the (110)-oriented *STO* substrate and of the *LSMO* film. Here, the substrate surface has the 6 × 4 reconstruction (Fig. 3.31*(left)*) while the film surface shows a $c \times 4$ reconstruction (Fig. 3.31*(left)*).

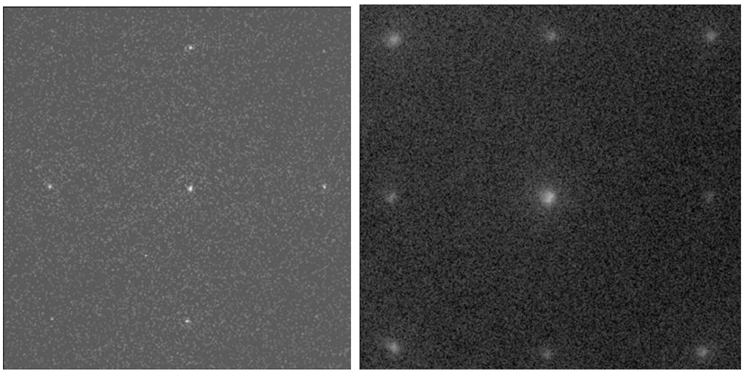

Figure 3.30. *LEED* patterns of the (001) *STO* single crystal substrate (*left*) showing no reconstructured surface and of the *LSMO* film deposited on it (*right*) showing itself no reconstruction.

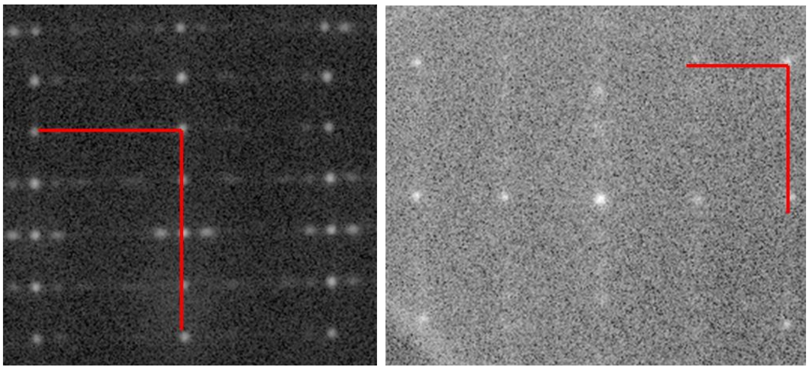

Figure 3.31. *LEED* patterns of the (110) *STO* single crystal substrate (*left*) showing a 6 × 4 reconstructured surface and of the *LSMO* film deposited on it (*right*) showing 1 × 4 reconstruction.

Fig. 3.32 shows the scanning tunnel microscopies (*STM*) of a (001) *STO* single crystal substrate and of a *LSMO* film grown on (001) *STO* performed in *UHV* condition at room temperature in non-contact mode ($1pA$ - $2V$). The typical width of terraces is $140nm$. The average roughness on a $3\mu m \times 3\mu m$ area is $0.5nm$.

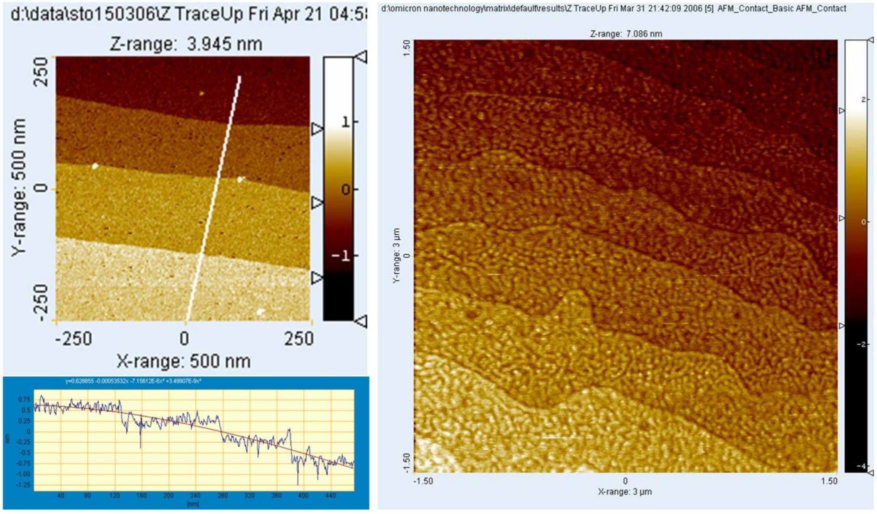

Figure 3.32. Left panel: $500 \times 500 nm^2$ *STM* image ($V = 2V$; $I = 10pA$) of the surface of a (001) *STO* single crystal substrate *(left)*. Right panel: $3 \times 3\mu m^2$ *STM* image ($V = 1V$; $I = 100pA$) of the surface of a *LSMO* film grown on (001) *STO*.

3.2.3.3. Structural and electronic measurements

The structural properties of the samples were investigated performing ex-situ measurements. Two sets of films with different thickness were particularly studied, namely $13nm$ and $45nm$. The *FWHM* of the rocking curve of the (002) *LSMO* peak was always of the order of the (002) substrate peak ($\sim 0.02°$), indicating the high quality crystal structure of the film (Fig. 3.33(*left*)). Moreover, the x-ray interference frings on the side of the (002) *LSMO* peak in the $\theta - 2\theta$ scan are an indication of an extremely smooth film surface (Fig. 3.33(*right*)).

The *STO* / *LSMO* ($13nm$ thick) interface was investigated by *High Resolution Trasmission Electron Microscopy* (*HR-TEM*) [3] (Fig. 3.34). The *TEM* images were performed in high

---

[3] This measurement was performed at the laboratories of the Physics Department of the University of Cagliari by Dr. A. Falqui.

resolution bright field. The *LSMO* appears darker for two distinct reasons. First, during the sample preparation it was observed that *LSMO* is harder than *STO*, so that a slightly different and perhaps inhomogeneous thickness is possible. Second, the electronic density of *LSMO* is higher, resulting in a higher absorption coefficient of the electron beam. Such measurements do not show any sign of relaxation of the *LSMO* structure, indicating that the film is completely strained on the substrate, in agreement with the *XRD* measurements. Moreover, neither dislocations nor stacking faults were found.

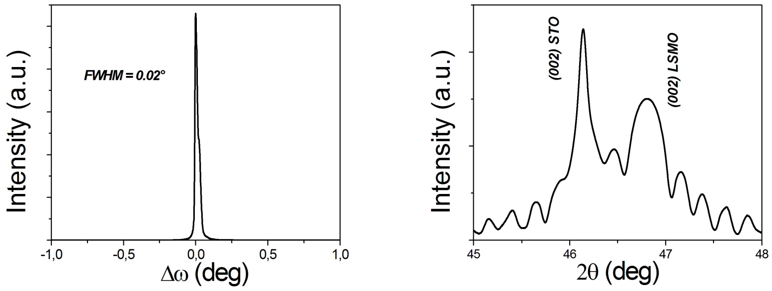

Figure 3.33. ω-scan (*left*) and $\theta - 2\theta$ scan (*right*) around the (002) reflection of the *LSMO* film (45nm thick) deposited onto *STO* (001). Note the $FWHM = 0.02°$ value of the *LSMO* rocking *(left)* and the interference frings around the (002) peak *(right).*

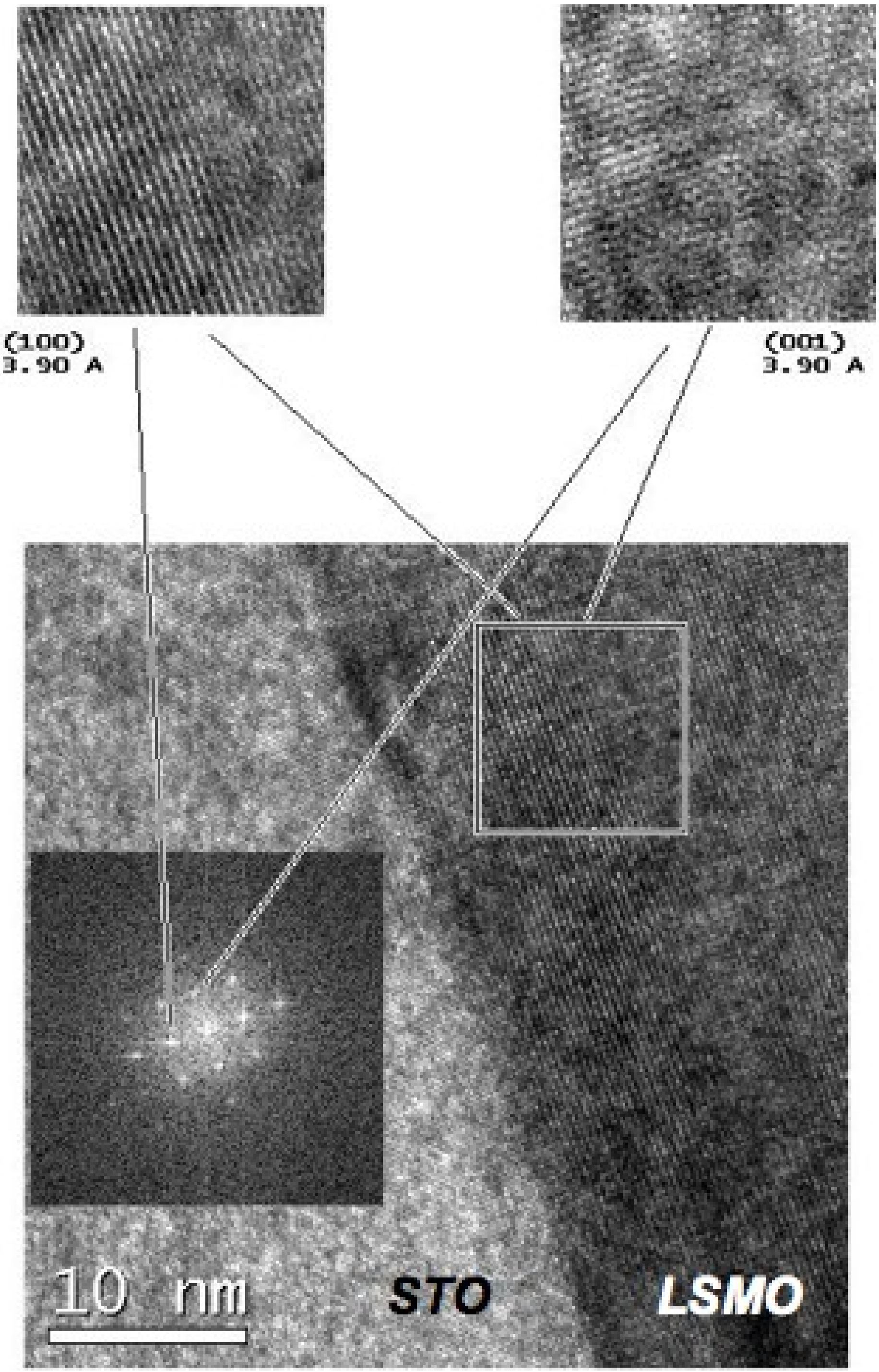

Figure 3.34. *HR-TEM* of *LSMO*, $13nm$ thick, grown onto *STO* (001).

3.3. Detailed investigation of the structural properties of LSMO thin films

A deeper investigation of the films structure was performed by resorting to *Reciprocal Space Mapping* (*RSM*) on several *LSMO* films grown onto *STO* in both (001) and (110) crystallographic orientations. Even though the general properties are very similar, slightly different features were found depending on the deposition technique.

The *XRD* analyses were performed as following. I determined the relevant regions of reciprocal space by calculation based on reasonable assumptions on film structure. To this aim, a pseudocubic notation was adopted to index film reflections. Once relevant regions were identified, the reciprocal space was mapped by a sequence of ω-scans at increasing 2θ values. Finally, the positions of *LSMO* peaks were refined. The presence of a substrate peak in each investigated region is a useful reference, that allows us to estimate and minimize the calibration error of the set-up at each reflection. Even though 3 independent reflections are sufficient to determine the crystal structure, a least-square fit procedure respectively with more reciprocal space vectors were usually considered [99].

3.3.1. Structure of LSMO grown onto (001) STO

In the following, I show the structural analysis of selected samples of *LSMO* grown on (001) *STO* deposited by sputtering and laser ablation.

3.3.1.1. Samples grown by sputtering

Defining a reference frame (that is always adopted in what follows with regards to the (001) crystallographic growth orientation) in such a way that $[100]_{STO}\|\hat{x}$, $[010]_{STO}\|\hat{y}$, $[001]_{STO}\|\hat{z}$, $\hat{x}$ and $\hat{y}$ lying in the substrate plane, and $\hat{z}$ being perpendicular to it, the crystallographic *LSMO* growth orientation always results parallel to the *out-of-plane* axis [001].

The *RSM*s of the regions around the (002), (303) and (223) *STO* reflections of a $32nm$ thick *LSMO* grown on (001) *STO* by sputtering are shown in Fig. 3.35.

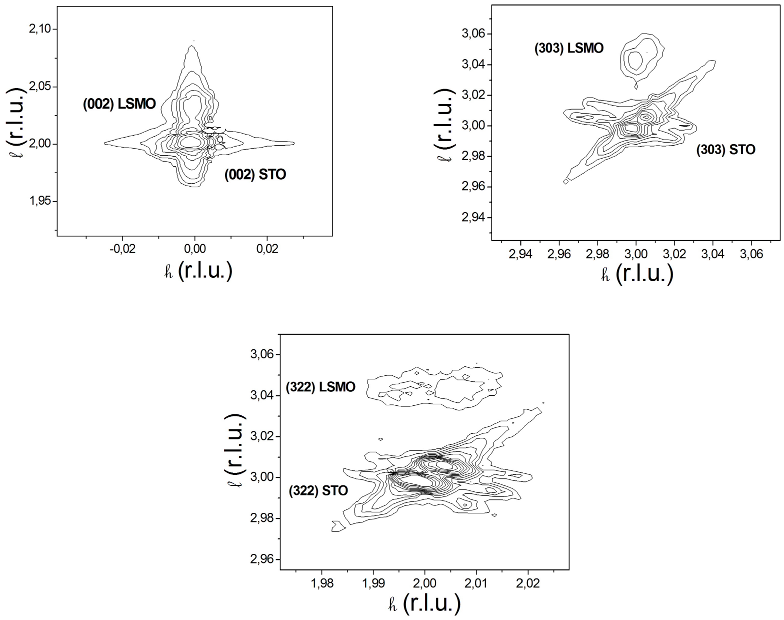

Figure 3.35. *RSM*s around the (002), (303) and (322) reflections of the *LSMO*, $32nm$ thick, film deposited on (001) *STO*.

The indexing of *LSMO* reflections deserves attention. The splitting of (322) and (303) reflections reveal the distortion of the cubic lattice and the presence of two growth domains.

The actual mosaic structure is deduced on the basis of the data and of symmetry considerations. The refined positions of the investigated *LSMO* peaks, together with the results of the least squares fit, are reported in Tab. 6.1. The *LSMO* has a strained rhombohedral cell, with *in-plane* axes elongated and the out-of-plane axis compressed. The angle between the in-plane axes is 90.2°, while the out-of-plane axis is perfectly perpendicular to them. Thus, I found four different crystallographic orientations of *LSMO* lattice (Fig. 3.38*(a)*). The smaller in-plane diagonal of the *LSMO* rhombohedral cell $d^{min}_{LSMO} = 0.5511nm$ is tilted of $\gamma = \gamma\prime = arct\left(\frac{d_{STO}-d^{min}_{LSMO}}{d^{min}_{LSMO}}\right) = 0.12°$ in respect to the diagonal of the *STO* ($d_{STO} = 0.5523nm$). These data confirm the distortion of the pseudocubic structure, that also determines the existence of four twinned domains. The (001) plane is parallel to the (001) *STO* for each domain in the samples (or otherwise, the (002) map in Fig. 3.35 should show *LSMO* peaks splitting). Concluding, these films are perfectly matched to the substrate lattice and their cell volume is expanded of $\sim 1.0\%$ with respect to bulk *LSMO*. This feature is attributed to a small amount of oxygen vacancies (a stoichiometry of about 0.025 in formula units) that are left after the deposition and cooling process.

3.3.1.2. Samples grown by laser ablation

The *RSMs* analyses of $42nm$ thick *LSMO* grown onto (001) *STO* by *PLD* in Caen shows that, also in this case, the *LSMO* has a strained rhombohedral cell, with *in-plane* axes elongated to perfectly match the *STO* cubic lattice, and the [001] axis compressed ($c_{[001]} = 0.3857nm$ for a *LSMO* $75nm$ thick). The angle between the *in-plane* axes is 90.0° within the experimental error. The volume of the *LSMO* cell is therefore slightly expanded of about 1%. The refined positions of the investigated *LSMO* peaks, together with the results of the least squares fit, are reported in Tab. 6.3.

The *RSMs* on the *LSMO* films, $45nm$ and $13nm$ thick, deposited onto (001) *STO* substrate by *RHEED*-assisted laser ablation in Naples were performed following the same procedure described above. *R*egions around the (103), (113), ($\bar{1}13$) and (303) for the *LSMO* $45nm$ thick are shown in Fig. 3.36.

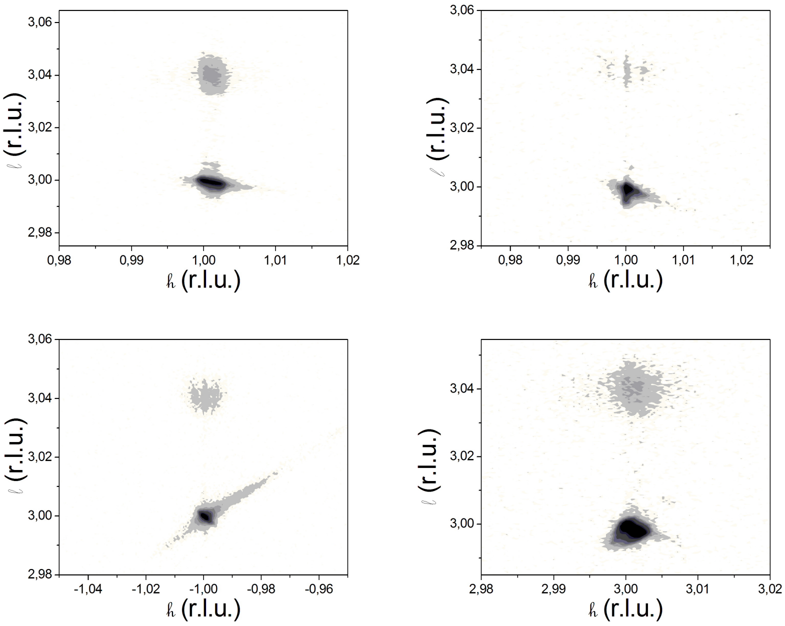

Figure 3.36. *RSMs* around the (103), (113), ($\bar{1}13$) and (303) reflections of the *LSMO* film, $45nm$ thick, deposited onto (001) *STO*.

Regions around the (002) and (103) peaks of the $13nm$ thick $LSMO$ are shown in Fig. 3.37.

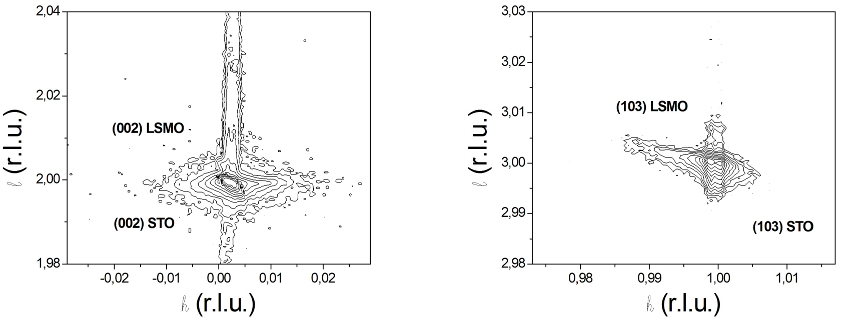

Figure 3.37. *RSMs* around the (002) (*left*) and (103) (*right*) reflections of the $LSMO$ film ($13nm$ thick) deposited onto(001) STO. Note the $FWHM = 0.02°$ value of the $LSMO$ rocking.

Both $LSMO$ films are fully strained showing *in-plane matching* (in plane axis $0.3905nm$ in agreement with the less sensitive $LEED$ measurements (Sec. 3.2.3, Fig. 3.30)). The $45nm$ thick $LSMO$ film shows a $c-axis = 0.3888nm$ while the thinner film has $c-axis = 0.3853nm$, as it results from a least mean square analysis based on the positions of the diffracted crystallographic peaks (Tabs. 6.4 and 6.5).

Concluding, the $LSMO$ films deposited by PLD are fully *in-plane* strained. The *out-of-plane* axis is compressed for the thicker film while it is slightly elongated for the thinner one. The angle between the two in-plane axes is always 90.0° (within the experimental error). The vertical axis is perpendicular to the *in-plane* axes for thick films (90.0°), while for thinner films it results slightly tilted (89.3°). In Fig. 3.38*(b)* a sketch of the distortion of the $LSMO$ on the (001) STO substrate is depicted.

These results are in fair agreement with what obtained for $LSMO$ film of several thickness deposited by PLD and $RHEED$-assisted laser ablation, and they are consistent with reported data in literature [11, 101] for $LSMO$ films deposited by laser ablation.

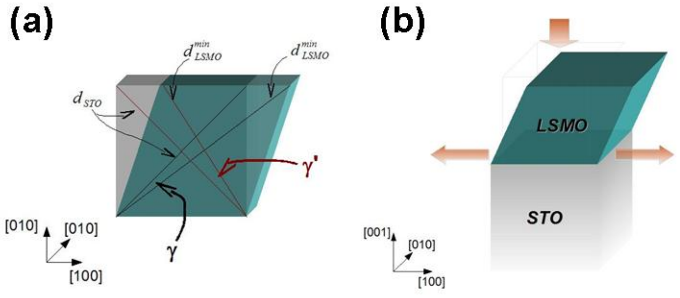

Figure 3.38. Alignment of the *in-plane* cell of $LSMO$ (*green*) with respect to STO (001) *(gray)* in four crystallographic domains in the case of $32nm$ thick film grown by sputtering. The splitting of the $(322)/(32\bar{2})$ $LSMO$ peak is due to the different length of the rhombus diagonals *(a)*; Schematic of the $LSMO$ cell distortion induced by the STO (001) substrate in the case of in the case of $13nm$ thick film grown by PLD *(b)*.

3.3.2. Structure of LSMO grown onto (110) STO

Referring to Fig. 1.4 in Sec. 1.5, I discuss here of the case of *LSMO* films deposited onto (110)-oriented *STO* substrates. Since no significative difference were found between *LSMO* films deposited by sputtering and laser ablation, I show here the main features of one selected sample, that is a sputtered $51nm$ thick *LSMO* film.

Let $[\bar{1}10]_{STO}\|\hat{x}$, $[001]_{STO}\|\hat{y}$, $[110]_{STO}\|\hat{z}$, with $\hat{x}$ and $\hat{y}$ laying in the substrate plane, while $\hat{z}$ is perpendicular to it. In such a way, the crystallographic *LSMO* growth orientation is parallel to the out-of-plane axis [110]. *RSMs* of the regions around the (220), (400) and (222) *STO* reflections are shown in Fig. 3.39.

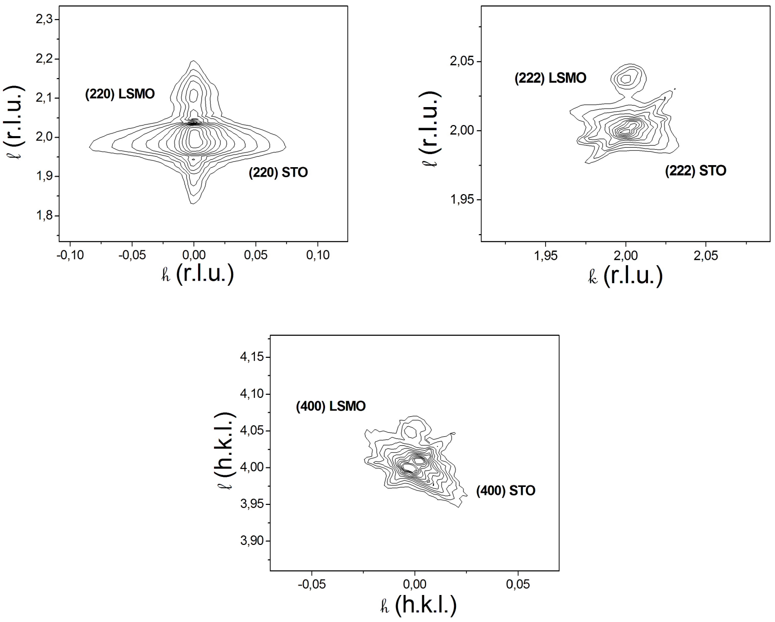

Figure 3.39. *RSM* around the (220), (222) and (400) reflections of the *LSMO* film, $51nm$ thick, deposited on (110) *STO*.

The indexing of *LSMO* reflections is straightforward in this case. The refined positions of the investigated *LSMO* peaks, together with the results of the least squares fit results, are reported in Tab. 6.2. A single domain is detected. However, the $P2$ symmetry of the (110) *STO* substrate surface suggests the existence of two domains, with mirror symmetry with respect to the xz plane. The second domain should yield the $(22\bar{2})$ *LSMO* peak at $2\theta = 86.61°$, $\omega - \theta = 35.08°$. I observed such peak in thicker films, but in this case it is probably hidden by the $CuK_{\alpha 2}$ (220) *STO* at $2\theta = 86.88$, $\omega - \theta = 35.08$. As an alternative explanation, the second domain could really be absent, due to breaking of the $P2$ symmetry because of a small miscut of the substrate.

Summaryzing, the *LSMO* film is strained. The angle $\hat{ab}$ between the ***out-of-plane*** axes is slightly increased with respect to the bulk, while the angles $\hat{bc}$, $\hat{ca}$ that are formed with the *in-plane* axis have the same value as in the unstrained rhomboedral structure. The *in-plane* axis is elongated to match the *STO* lattice spacing. Also in this case the cell volume is somewhat expanded (about 1.0%) with respect to bulk *LSMO*. As in the case of sputtered *LSMO* grown onto (001) *STO*, I attribute this last feature to a small amount of oxygen vacancies (a stoichiometry of about 0.05 in formula units) that are left after the deposition and cooling process.

As a concluding remark, I stress that fully strained films are obtained both on (110) and (001) *STO* even at quite high thickness. The upper limit for the growth of fully strained *LSMO* (i.e., the critical thickness) was not explored neither for sputtering nor for *RHEED*-assisted laser ablation. In the case of the *PLD* in Caen, Fig. 3.16*(left)* indicates that at low deposition temperature some degree of relaxation in present, indirectly pointing to the idea that the highest critical thickness is achieved at the highest deposition temperature.

3.4. Resistivity and magnetization behaviour in function of the temperature of LSMO films

In the following, I report on the behaviour of the resistivity vs. temperature and of the magnetization vs. temperature for three selected samples of *LSMO* deposited onto (001) *STO* substrates grown by sputtering, *PLD* and *RHEED*-assisted laser ablation as described in Secs. 3.2.1, 3.2.2 and 3.2.3, respectively. Although such films show quite similar resistivities and magnetic behaviours, I can envisage some features that are characteristic of each technique. I carried out all the $\rho(T)$ measurements in four probe configuration, typically in the range $8K$ - $450K$ in a cryocooler (Fig. 3.40*(a)*). The $M(T)$ measurements were performed with the magnetic field lying in-plane along the [100] crystallographic direction (Fig. 3.40*(b)*). Both *MIT* temperature (T_{MI}) and Curie temperature (T_C) resulted well above the room temperature for all the considered samples. However, I found a maximum $T_{MI} \sim 380K$ for the sample grown by *RHEED*-assisted laser ablation and the maximum $T_C \sim 345K$ for both the *LSMO* deposited by sputtering and *PLD*. Moreover, the *LSMO* deposited by *RHEED*-assisted laser ablation (black circle in Fig. 3.40*(b)*) shows a very sharp transition from the *FM* to the *PI* phase at $335K$.

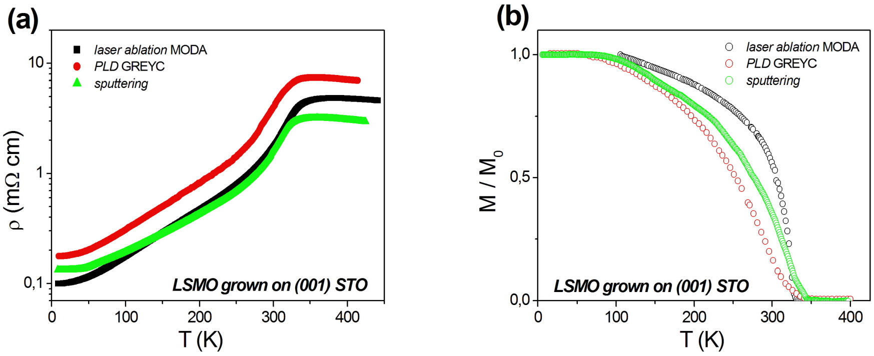

Figure 3.40. $R(T)$ *(a)* and $M(T)$ *(b)* of three selected *LSMO* samples grown onto (001) *STO* substrates by sputtering (*green curves*), *PLD* (*red curves*) and *RHEED*-assisted laser ablation (*black curves*). The magnetic fields, applied along the [100], in *(b)* were $H = 1kOe$, $H = 5kOe$ and $H = 5Oe$ for the films grown by sputtering, *PLD* and *RHEED*-assisted laser ablation, respectively.

Chapter 4

Growth of LSMO thin films on buffered Si substrates

Recently, the scientific community has devoted great attention to the growth of oxides on silicon substrates. Several studies of the growth of *high-k dielectric* oxides (such as *STO* and *LAO*) on silicon for resistance memory applications, *CMOS*, *MOSFET* [102, 103, 104] and on the film-bufferred *Si* substrate interfaces [105] are reported in literature. To meet the industrial demand of high integration and low cost technology, depositing films on silicon is the first step toward their integration with the conventional electronics. In addition, since silicon is commonly used in industrial processes, its utilization as a substrate for deposition of high quality epitaxial films would represent an important boost for the the technologies based on manganites.

Furthermore, using silicon substrates represents an advantage when micromachined processes have to be exploited. As a relevant example (see Sec. 2.1) in order to get high performance in bolometers, the sensor must be thermally decouple from the substrate, that is the heat sink (see Fig. 2.2). This can be achieved by engineering membranes or suspended microbridges by photolitographic and etching processes [106], that is a well established technique for *Si*.

Unfortunately, the deposition of manganite films on silicon is very difficult because *Si* is extremely sensitive to the oxidizing atmosphere, and a SiO_x amorphous layer is immediately formed on it. This has two implications: first, before manganite deposition one must eliminate the amorphous layer, because otherwise no epitaxy can be achieved; second, one must resort to a deposition technique that is inhibits SiO_x formation in the deposition atmosphere before film growth.

A thermal treatment in *UHV* can remove the SiO_x overlayer. as I demonstrated in the following experiment. A *Si* substrate, previously exposed to ambient atmosphere, was introduced in the analytical chamber of M.O.D.A. and a *XPS* measurement was performed. The sample was then annealed at 850°C in *UHV* (less then $10^{-9} mbar$ residual pressure), and the *XPS* was performed again. The comparison of the *XPS* measurements show that the *O* was completely removed, as proved by the absence of the O_{1s} peak in the annealed sample (Fig. 4.1).

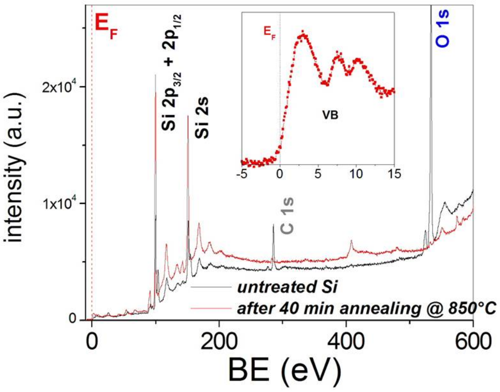

Figure 4.1. *XPS* analysis reveals the removal of the oxygen from the *Si* surface after heating at 850°C for $30 min$.

McKee *et al.* [107] and Zhou *et al.* [108] demonstrated that it is possible to grow a perovskite, namely STO, on the top of a Si substrate, if a suitable deposition procedure is followed. This requires, however, a high deposition temperature, that does not meet the semiconductor industry requirements.

It is therefore desiderable a different strategy. The best approach is at present based on the so-called *buffer* layers. This is the route that I followed in this research, as I will show in the following.

4.1. Growth of LSMO multilayer on buffered Silicon substrates

The epitaxial growth of $LSMO$ (and many of the multicomponent oxides of interest) on silicon is difficult, as stated before, mainly for the following reasons:

1. Chemical reaction between Si and $LSMO$ at the high deposition temperature of $LSMO$;
2. Presence of amorphous native oxide at the Si surface;
3. Large difference in the thermal expansion coefficient between Si and $LSMO$ of the order of $2 \times 10^{-6} K^{-1}$ and $10 \times 10^{-6} K^{-1}$, respectively, resulting in cracks of the films.

To circumvent these problems, one can introduce one or several intermediate layers (*buffer* layers) between Si and $LSMO$ (Fig. 4.2). The disadvantage is that in this case a multilayer is required instead of a single layer, possibly resulting in degraded structural and morphological properties of $LSMO$. The advantage on the other hand, are the following:

1. It is possible to choose a *buffer* layer, namely YSZ (Ytrria-Stabilized-Zirconia) that solves the problem of SiO_x formation and of Si-$LSMO$ reaction;
2. It is possible to choose one (or a sequence of) further layer, to fit the lattice of YSZ to $LSMO$.

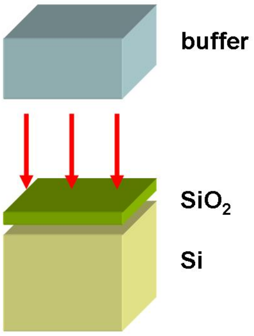

Figure 4.2. Scematic of buffer layer.

YSZ is commonly used as buffer layer to start the epitaxial growth on silicon substrate, because its reducing properties can be used to remove the native amorphous oxide at the Si surface, without resorting to sophisticate etching procedures. Suitable deposition conditions are required, namely a low O_2 pressure in the first stage of growth [109]. In such condition, the reaction:

$$Zr + 2SiO_2 \longrightarrow ZrO_2 + 2SiO \tag{4.1}$$

is favoured and the native SiO_2 is effectively removed from the Si surface. This also allows the epitaxial growth of YSZ. The in-plane lattice of YSZ is square with $a = 0.5430 nm$

spacing. The diagonal has a lenght that is commensurate to perovskite: $d = 0.3840nm$. However, to get the best growth of $LSMO$, some further buffer layer is required. One strategy, that was exploited in [75], is to grow a sequence of CeO_2 and of $Bi_4Ti_3O_{12}$ (BTO) before $LSMO$, but STO and LAO are also interesting buffers (Tab. 4.1).

material	*structure*	**a // [100] (nm)**	**b // [010] (nm)**	**c // [001] (nm)**	**d/2 // [110] (nm)**	**mismatch (%) with LSMO**	**thermal expansion coefficient (1/K @ 300°C)**
Si	cubic	0,5430	0,5430	0,5430	0,3840	-0,8	2,5 x 10-6
YSZ	cubic	0,5150	0,5150	0,5150	0,3642	-5,9	10,3 x 10-6
CeO_2	cubic	0,5420	0,5420	0,5420	0,3833	-1,0	-
$Bi_4Ti_3O_{12}(BTO)$	orthorhombic	0,5410	0,5490	3,2800	0,3825	-1,2	~ 11 x 10-6
$SrTiO_3(STO)$	cubic	0,3905	0,3905	0,3905	-	0,9	10,4 x 10-6
$LaAlO_3(LAO)$	*pseudo*-cubic	0,3790	0,3790	0,3790	-	-2,1	9,4 x 10-6
$La_{0.7}Sr_{0.3}MnO_3(LSMO)$	*pseudo*-cubic	0,3870	0,3870	0,3870	-	-	~ 11 x 10-6

Table 4.1. Non-exhaustive list of possible buffer layers for the epitaxial growth of $LSMO$ on silicon substrates [109].

Quite high MIT temperature and low room temperature resistivity were obtained using $BTO/CeO_2/YSZ/Si$ by Kim *et al.* [75, 112, 113]. Other research groups studied the epitaxial growth of oxides on silicon using different deposition techniques and in different deposition conditions. For instance, polycrystalline $LSMO$ films were obtained if deposited on Si without buffer layer [90], on SiO_2/Si [91] or on YSZ/Si [92]. Two sets of in-plane orientations were found in $1000nm$ thick $LSMO$ films deposited on $YBCO/YSZ/Si$ [92]. Full in-plane epitaxy of $LSMO$ was instead achieved on STO/Si [110, 111] and on YSZ-buffers [75, 112, 113, 114, 115]. A summary of literature data is given in Tab. 4.2.

	Buffer materials	**Deposition technique**	**T_C (K)**	**T_P (K)**	**ρ (mΩcm) @ 300K**
Liu *et al.* [68]	*none*	*Spin coater*	357	260	300
Bergenti *et al.* [69]	*SiO_2*	*Pulsed Plasma Deposition*	325	235	?
Goh *et al.* [70]	*YBCO / YSZ*	*PLD*	?	> 300	0:09
	YSZ	*PLD*	?	230	3
Pradhan *et al.* [87, 88]	*$SrTiO_3$*	*PLD*	330	335	2
Kim *et al.* 60, 89, 90]	*BTO / CeO_2/ YSZ*	*PLD*	?	390	1:14
Fontcuberta *et al.* [91]	*STO / CeO_2/ YSZ*	*PLD*	350	200	20
Trajanovic *et al.* [92]	*BTO / YSZ*	*PLD*	340	390	0,0625

Table 4.2. Examples of literature data showing $LSMO$ deposition on (001) Si using various buffer layers and deposition techniques. T_C is the *Curie temperature*, T_P is the temperature of the maximal resistance, and ρ is the resistivity at room temperature of the $LSMO$.

Within the research project that I carried in Caen, I deposited two particular sequence of layers on silicon substrates: $LSMO$ / BTO / CeO_2 / YSZ / Si and $LSMO$ / STO / CeO_2 / YSZ / Si, named in the following BTO-based and STO-based, respectively. I optimized the deposition conditions of such multilayers in order to get high crystal quality, large change of resistance around the T_C and flat surfaces.

4.1.1. Deposition conditions

I deposited the buffer and the $LSMO$ layers by the standard PLD technique onto (001) Si $10 \times 10mm^2$ substrates in the PLD system at the $GREYC$ laboratory (see Sec. 3.1.2 for details) without any removal of the native amorphous SiO_x oxide from the Si surface. For all materials the laser energy was $250mJ$, the *target-to-substrate* distance was $50mm$, the pulse rate was fixed at $3Hz$, and the spot size on the target was $2 \times 1mm^2$. Tab. 4.3 lists in summary the optimized deposition conditions used for the growth of the multilayers and of the *LSMO* on *STO* single crystal substrate.

substrate	*layer*	T (°C)	p_{O_2} (mbar)	pulses (#)	thickness (nm)	EGY (mJ)	f (Hz)	deposition rate (nm/shot)
Si (001)	YSZ	700	10^{-4}	3000	130	250	3	0,043
	CeO2	700	0,30	250	10	250	3	0,038
	BTO	700	0,30	1000	20	250	3	0,017
	LSMO	720	0,35	3000	50	250	3	0,017
Si (001)	YSZ	720	0,00	3000	130	250	3	0,043
	CeO2	720	10^{-2}	250	10	250	3	0,038
	STO	720	10^{-2}	3000	50	250	3	0,017
	LSMO	720	0,35	3000	50	250	3	0,017
STO (001)	LSMO	720	0,35	2500	40	250	3	0,017

Table 4.3. Deposition conditions for the *LSMO* and under top layers growth on *Si*-buffered and (001) *STO* substrates.

A comprehensive x-ray diffraction study lead to the optimized deposition temperature of 700°C for *YSZ*. During the *YSZ* deposition, the oxygen pressure was fixed at $2 \times 10^{-5} mbar$ during 2 minutes and it was then increased to $10^{-4} mbar$. In such condition, the reaction in Eq. 4.1 is favoured and the *YSZ* layer deposited onto *Si* (001) has the (001) orientation. Fig. 4.3 shows the typical $\theta - 2\theta$ scan. The *FWHM* of the rocking curves of the (004) *YSZ* peak (not shown here) were always found in the 0.5° - 0.8° range. The *YSZ* lattice is to be cubic as it is demonstrated by the *XRD* study (Tab. 6.7), that is, the *YSZ* has the unstrained, bulk lattice. I fixed the deposition temperature and oxygen pressure during the subsequent CeO_2 deposition at 700°C and $0.35 mbar$, in the case of *BTO*-based, and 720°C and $10^{-2} mbar$ in the case of *STO*-based multilayers.

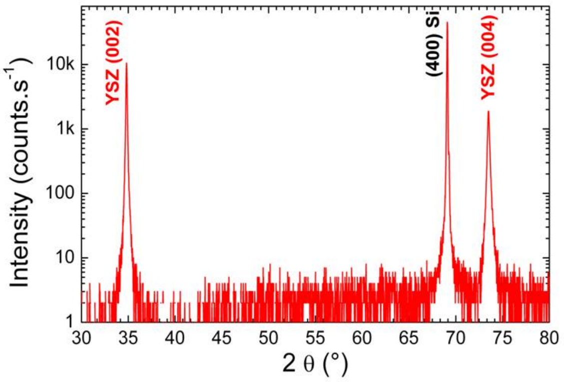

Figure 4.3. $\theta - 2\theta$ scan reveals the epitaxial growth of the *YSZ* layer with a full (001) orientation and no parasitic phases.

The *YSZ* and CeO_2 films are smooth, with *RMS* roughness in the $0.2 - 0.3 nm$ range over $10 \times 10 \mu m^2$ surface areas, as revealed by *AFM* (Fig. 4.4). The CeO_2 layer was never detected in *XRD* measurements, probably because it is too thin. However, if missing, a non epitaxial sequence was obtained, in contrast to the results of Goh *et al.* for *LSMO / YSZ / Si (001)* and *LSMO / YBCO / YSZ / Si (001)* multilayers [92]. Moreover, these authors found an incomplete (001) orientation in the former case and a two set of *in-plane* orientations with an *in-plane* shift of 45° from each other. These findings demonstrate the relevance of the CeO_2 layer.

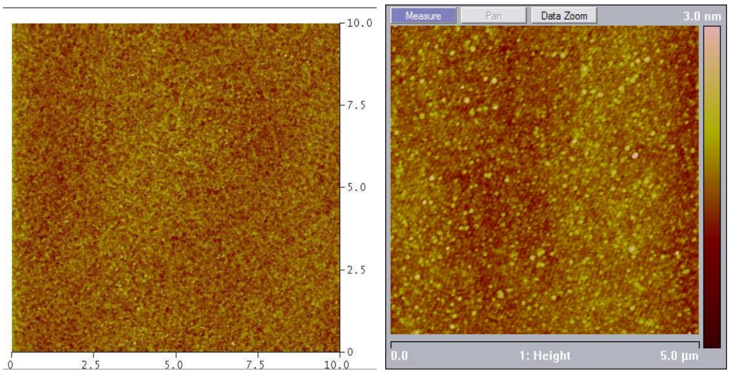

Figure 4.4. Left panel: $10 \times 10 \mu m^2$ *AFM* image of the *YSZ* surface ($RMS = 0.4 nm$) grown on *Si* (001) in reducing condition. Right panel: $5 \times 5 \mu m^2$ *AFM* image of the CeO_2 surface ($RMS = 0.22 nm$) grown on *YSZ* / *Si* (001).

4.2. BTO-based LSMO samples

I fabricated the *LSMO* / *BTO* / CeO_2 / *YSZ* / *Si* (*BTO*-based) *LSMO* multilayers following the deposition conditions reported in Tab. 4.3. The growth temperature and oxygen pressure during the *BTO* layer deposition were optimized at 700°C and $0.35 mbar$. The deposition conditions used for *LSMO* were the same as for the growth on standard (001) *STO* substrates, i.e. the substrate temperature was 720°C and the oxygen pressure was $0.35 mbar$. Soon after *LSMO* deposition, a $700 mbar$ oxygen pressure was introduced in the deposition chamber and the films were cooled to ambient temperature at 10°C/min. The typical layer thicknesses in this study are $10 - 50 nm$, $5 - 60 nm$, $10 nm$ and $130 nm$ for *LSMO*, *BTO*, CeO_2 and *YSZ*, respectively.

4.2.1. Structural properties of LSMO films on $BTO/CeO_2/YSZ/Si$

I studied the structure of the multilayers resorting to *XRD*. The reference frame is defined as following: $[100]_{Si} \| \hat{x}$, $[010]_{Si} \| \hat{y}$, $[001]_{Si} \| \hat{z}$, $\hat{x}$ and $\hat{y}$ lie in the substrate plane, and $\hat{z}$ is perpendicular to it. The multilayers crystal quality were checked by performing ω-scans. It turns out that the *FWHM* of the *LSMO* (002) peak is typically in the 1° - 1.8° range, that is much larger than the *FWHM* of the (002) peak of *LSMO* grown onto (001) *STO* substrate (Fig. 4.5*(left)*). However, the *FWHM* around the (0016) *BTO* is 2°, that is, the mosaicity of *BTO* is probably responsible of the quite large *FWHM* of the (002) *LSMO*. Fig. 4.5*(right)* shows a typical x-ray diffractogram in the $\theta - 2\theta$ configuration. It reveals the $(00l)$ orientation of all layers.

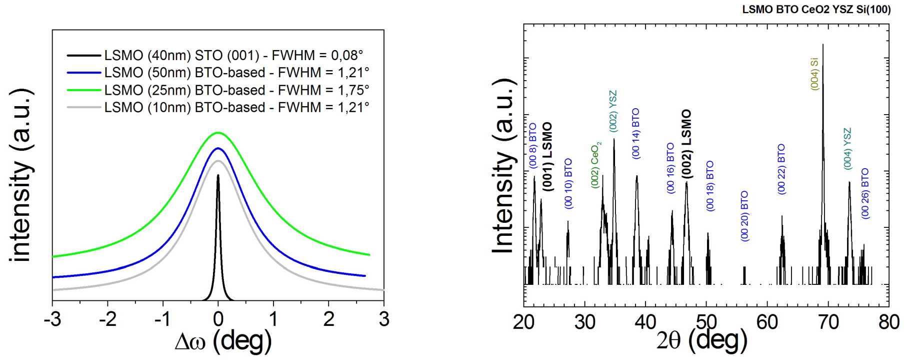

Figure 4.5. Left panel: ω-scans of the *BTO-based LSMO* samples around the (002) *LSMO* relection for different *LSMO* thicknesses. Right panel: X-ray diffractogram in the $\theta - 2\theta$ configuration of a $50nm$ *LSMO* film deposited on $BTO/CeO_2/YSZ/Si$ in the optimized deposition conditions of Tab. 4.3.

The in-plane alignment of each layer was checked resorting to ϕ-scan measurements around the $(103)_{LSMO}$, $(2232)_{BTO}$, $(113)_{YSZ}$ and $(113)_{Si}$ crystallographic planes. These measurements reveal a perfect alignment of the $(110)_{YSZ} \parallel (110)_{Si}$, while the (2232) plane of BTO has a weak minority crystal phase rotated at 45° (Fig. 4.6). Since the $(110)_{BTO} (\parallel (110)_{Si})$ is parallel to $(100)_{LSMO}$ such a minority crystal phase determines two different domains in the $(303)_{LSMO}$, one aligned to the layer below and another rotated itself at 45°.

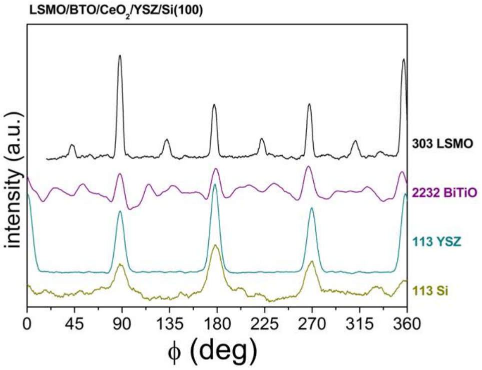

Figure 4.6. ϕ-scans of the *BTO-based LSMO* ($50nm$ thick) sample.

To complete the structural analysis, I performed *XRD* lattice mappings around the symmetrical $(00l)$ and the asymmetrical (113), (1121) and (103) diffraction peaks (Fig. 4.7). These measurements allow us to fully determine the crystal lattices of the samples. The *YSZ* layer grown on (001) *Si* substrate in reducing condition exhibited a *cube - on - cube* growth ($(001)_{YSZ} \parallel (001)_{Si}, (110)_{YSZ} \parallel (110)_{Si}$). The *LSMO* cell grows matching its side on the half *in-plane* diagonal of the orthorhombic *BTO* cell (*diagonal - on - cube*), and the *BTO* cell matches its in-plane side on that of *YSZ*, following a pseudo *cube - on - cube* growth. Thus it results that: $(001)_{LSMO} \parallel (001)_{BTO} \parallel (001)_{YSZ} \parallel (001)_{Si}$ and $(100)_{LSMO} \parallel (110)_{BTO} \parallel (110)_{YSZ} \parallel (110)_{Si}$ (Fig. 4.7).

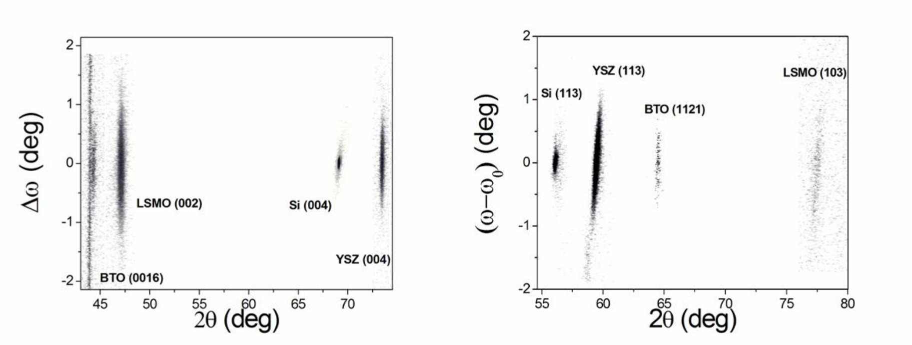

Figure 4.7. Symmetric (*left*) and asymmetric (*right*) *XRD* lattice mapping of *BTO*-based *LSMO* ($50nm$ thick) sample.

Summarizing, the *LSMO* cell is accommodated on the remaining part of the structure by rotating its cell by 45°, see Fig. 4.8, that is according to the epitaxial relation $(100)_{LSMO} \parallel (110)_{BTO} \parallel (110)_{Si}$) and matching its side with the half diagonal of *Si* (see the sketch in Fig. 4.8).

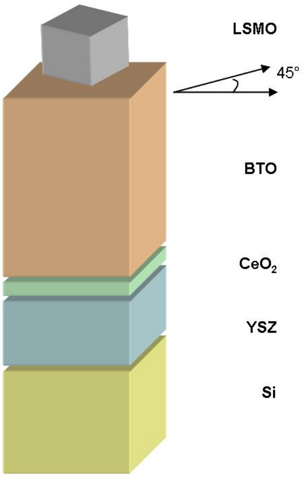

Figure 4.8. Sketch of the whole multilayer structure *BTO*-based *LSMO* films.

Probably due to its huge c-axis ($3.27nm$), the *BTO* is tilted by 0.6° from the normal. The *out-of-plane LSMO* axis itself is slightly tilted by 0.2° from the normal. *LSMO in-plane* axis are $0.3838nm$ and 0.3864 nm for $50nm$ and $25nm$ thick *LSMO* film, respectively. The *LSMO* c-axis is always elongated ($0.3880nm$ - $0.3893nm$ - $0.3914nm$) of about 0.18%, 0.52% and 1.06% for $50nm$, $25nm$ and $10nm$ *LSMO* thick layers.

Concluding, the *LSMO* top layer is compressively strained so that the *in-plane* lattice parameters are shortened and the *out-of-plane* parameter is elongated, for any considered *LSMO* thickness. The refined positions of the investigated *BTO* and *LSMO* peaks, together with the results of the least squares fit, are reported in Tabs. 6.8, 6.9, 6.10.

4.2.2. Morphological properties of LSMO films on $BTO/CeO_2/YSZ/Si$

Fig. 4.9 show *AFM* images in tapping mode of $50nm$ and $10nm$ thick *LSMO* films grown on *BTO*-based buffered silicon. In contrast to what I typically obtained on *STO* substrates, the films were rough showing RMS roughnesses in the $7-12nm$ range depending on the $LSMO$ thickness. Aggregates were indeed observed all over the $LSMO$ surface. They are much larger in the $10nm$ thick film than for the $50nm$ thick film, which could be due to a better self organisation of the $LSMO$ structure during its growth when the thickness is increased. The defective areas are probably due to a deviation from the nominal stoichiometry of Bi in the BTO layer underneath the $LSMO$ layer, as revealed by *electron dispersive spectroscopy* (EDS)[1] (Fig. 4.10). It is probable that the Bi content is not totally transferred from the target to the film. The subsequent growth of $LSMO$ on this non homogeneous layer is therefore perturbated.

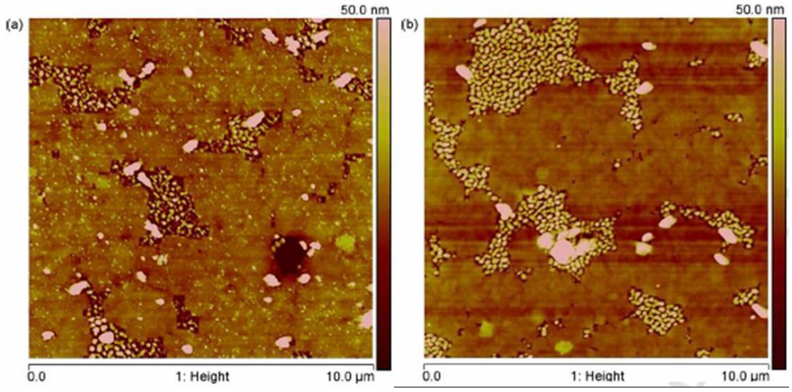

Figure 4.9. $10\mu m \times 10\mu m$ AFM images in the tapping mode of the $LSMO$ films on *BTO-based* buffered Si substrates for two $LSMO$ thicknesses: *(a)* $50nm$ thick $LSMO$; *(b)* $10nm$ thick $LSMO$.

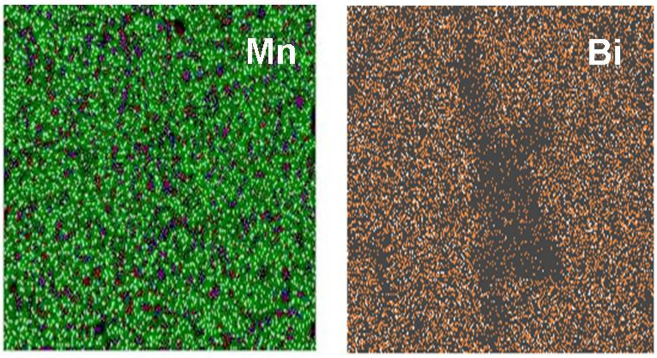

Figure 4.10. EDS measurement performed at $10keV$ on the *BTO-based* $LSMO$ ($50nm$ thick) sample.

4.2.3. Transport and magnetic properties of LSMO films on $BTO/CeO_2/YSZ/Si$

The BTO layer thickness plays an important role in the transport properties of the $LSMO$ thin films. The resisitivity of $50nm$ thick $LSMO$ films is plotted in Fig. 4.11*(a)* as a function of the temperature for BTO layer thickness in the $5-60nm$ range. Both the resistivity and the temperature of maximum resistance (T_P), sensitively vary as shown in the inset of Fig. 4.11*(a)*. Moreover, the AFM measurements (Fig. 4.9) suggest a BTO thickness thick enough in order to enable a continuous BTO layer to be formed. However, it has to be not too thick to perturbate the subsequent $LSMO$ growth. I found that the optimal layer thickness is $20nm$ for BTO. Fig. 4.11*(b)* shows the resistance versus temperature plots for $LSMO$ films

---

[1] This measurements was performed at the *CRISMAT - ENSICAEN* laboratory in Caen.

of different thickness deposited on $20nm$ thick BTO on CeO_2 / YSZ - buffered Si. A high value of T_P, i.e. $390K$, was measured for the $50nm$ thick films. As the $LSMO$ film thickness was decreased to $25nm$ and $10nm$, T_P was reduced to $365K$ and $356K$, respectively.

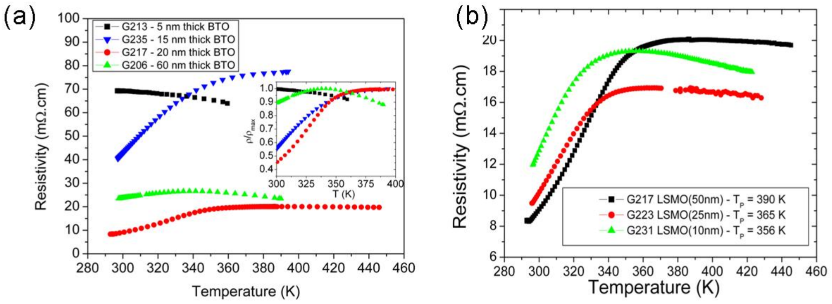

Figure 4.11. Resistivity vs. temperature characteristics of $LSMO$ films on BTO / CeO_2 / YSZ / Si (001) for different BTO thickness in $5-60nm$ range *(a)*. Resistivity vs. temperature characteristics of $LSMO$ films on BTO / CeO_2 / YSZ / Si (001) for $10nm$, $25nm$ and $50nm$ thick $LSMO$ thin films *(b)*.

A Curie temperature (T_C) of $355K$, $340K$ and $315K$ for the $50nm$, $25nm$ and $10nm$ thick $LSMO$, respectively, was found by magnetization measurements (Fig. 4.12)^2. The inset of Fig. 4.12 shows the $M-H$ loops recorded by applying the magnetic field along the in-plane diagonal of the $LSMO$ cell $((110)_{LSMO} \parallel (100)_{Si})$ for all the considered thicknesses.

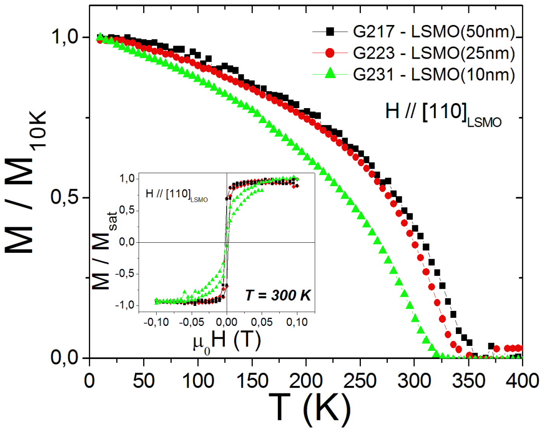

Figure 4.12. Saturation magnetization of $LSMO$ as function of the temperature for three values of thickness of $LSMO$. Inset shows the magnetic hysteresis cycles of $LSMO$ at $300K$.

Tab. 4.4 summarizes the properties of $LSMO$ on BTO-based buffered Si compared to typical values measured in $50nm$ thick $LSMO$ films deposited on STO substrates. Whereas they are close to bulk values in the latter case, the measured resistivities in $LSMO$ on BTO*-based* buffered silicon substrates are about 5 times higher and the measured saturation magnetization is about 3 times lower than expected. This deviation from the nominal value is indicating a non homogeneous $LSMO$, that in turn may be attributed to the inhomogeneity of the BTO layer, as shown by the EDS analysis (i.e., Fig. 4.10).

---

[2] performed at the *CRISMAT - ENSICAEN* laboratory in Caen.

LSMO thickness	Out-of-plane LSMO axis (nm)	ρ (mΩcm) @300K	T_C (K)	M_{sat}(μ_B/Mn_{site}) @10K	RMS roughness (5×5μm^2 AFM image) (nm)
50 nm on STO (001)	0,3865	2	345	3,7	0,3
10 nm	0,3914	12,8	315	1	10,1
25 nm	0,3893	10	340	1	7,7
50 nm	0,3880	9,2	355	1	12,5

Table 4.4. Summary of the properties of *LSMO* on *BTO*-based buffered *Si* as function of the thickness. T_C is the Curie temperature, T_P is the temperature of the maximal resistance, ρ is the resistivity, M_{sat} is the saturation magnetization of the *LSMO* layer.

4.3. STO-based LSMO samples

I fabricated the *LSMO / STO /* CeO_2 */ YSZ / Si* (*STO*-based) *LSMO* multilayers following the deposition conditions reported in Tab. 4.3. The growth temperature and the oxygen pressure for the under top *STO* layer deposition were optimized at 720°C and $10^{-2}mbar$. The deposition conditions used for *LSMO* were the same for the growth on standard (001) *STO* substrates, i.e. the substrate temperature was 720°C and the oxygen pressure was $0.35mbar$ (Tab. 4.3). Soon after *LSMO* deposition, a $700mbar$ oxygen pressure was introduced in the deposition chamber and the films were cooled to ambient temperature at 10°C/min. The typical layer thicknesses used in this study were $10-50nm$, $50-80nm$, $10nm$ and $130nm$ for *LSMO*, *STO*, CeO_2 and *YSZ*, respectively.

4.3.1. Structural properties of LSMO films on $STO/CeO_2/YSZ/Si$

I define the same reference frame as in the case of *BTO*-based multilayers ($[100]_{Si}\|\hat{x}$, $[010]_{Si}\|\hat{y}$, $[001]_{Si}\|\hat{z}$, $\hat{x}$ and $\hat{y}$ lie in the substrate plane, and $\hat{z}$ is perpendicular to it). I performed ω-scans around symmetrical and asymmetrical crystallographic reflections in order to check the crystal quality of each layer. *FWHMs* of the asymmetrical $(103)_{LSMO-STO}$ and $(113)_{YSZ-Si}$ were always $\sim 1°$ (Fig. 4.13*(left)*) demonstrating good degree of epitaxy of each layer. Moreover, the *FWHM* of the symmetrical (002) *LSMO* peak is smaller than what was obtained on the same reflection of the *LSMO* grown on *BTO*-based multilayers. Resorting to $\theta-2\theta$ *XRD* measurements, I proved the $(00l)$ orientation of all layers, as shown in Fig. 4.13*(right)*.

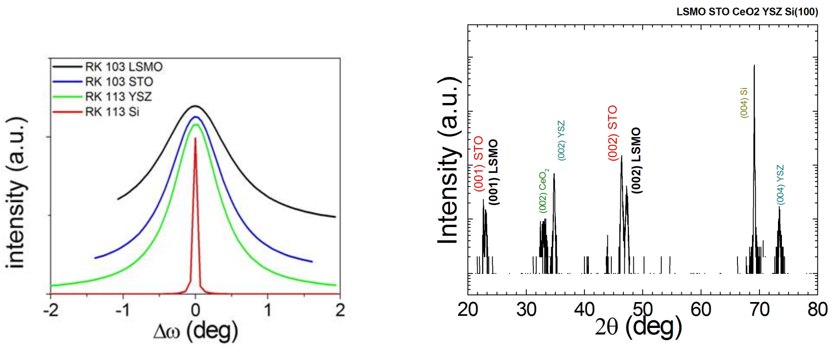

Figure 4.13. Left panel: ω-scans around the $(103)_{LSMO}$, $(103)_{STO}$, $(113)_{YSZ}$ and $(113)_{Si}$ relections of the $50nm$ *STO-based LSMO* samples. Right panel: X-ray diffractogram in the $\theta-2\theta$ configuration of a $50nm$ *LSMO* film deposited on $STO/CeO_2/YSZ/Si$ in the optimized deposition conditions of Tab. 4.3.

The ϕ-scan measurements around the $(103)_{LSMO}$, $(103)_{STO}$, $(113)_{YSZ}$ and $(113)_{Si}$ crystallographic peaks demonstrated the in-plane alignment of each layer (Fig. 4.14). Moreover, no spurious phase was identified just as in the case of BTO-based.

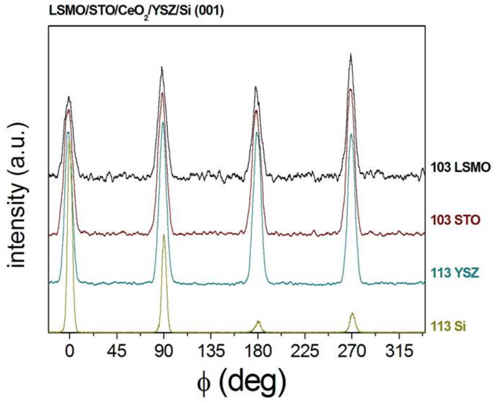

Figure 4.14. ϕ-scan of the *STO-based LSMO* ($50nm$ thick) sample.

I also performed XRD lattice mappings around the symmetrical $(00l)$ and the asymmetrical (113), (1121) and (103) diffraction peaks, allowing me to fully determine the crystal structure of the samples using a least mean square method. The $LSMO$ cell, as well as the STO, is rotated at 45° in respect to the Si (and YSZ) cell, determining a *diagonal-on-cube* growth. It results that $(001)_{LSMO} \parallel (001)_{STO} \parallel (001)_{YSZ} \parallel (001)_{Si}$ and $(100)_{LSMO} \parallel (100)_{STO} \parallel (110)_{YSZ} \parallel (110)_{Si}$ (Fig. 4.15).

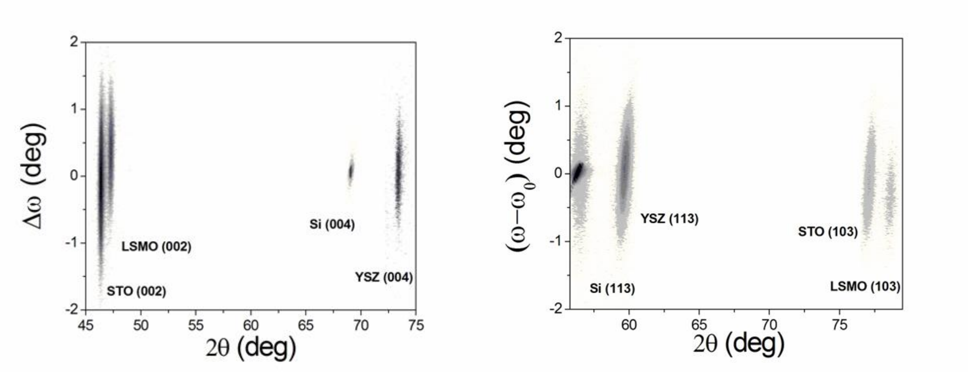

Figure 4.15. Symmetric (*top*) and asymmetric (*bottom*) XRD lattice mappings of STO-based $LSMO$ ($50nm$ thick) sample.

Analougsly to the BTO case, the pseudo cubic $LSMO$ cell is accommodated on cubic Si (or CeO_2 or YSZ) cell rotating in-plane its cell of 45°, i.e. $(100)_{LSMO} \parallel (100)_{STO} (\parallel (110)_{BTO}) \parallel (110)_{Si}$ and matching its side with the half diagonal of Si (see the sketch in Fig. 4.16).

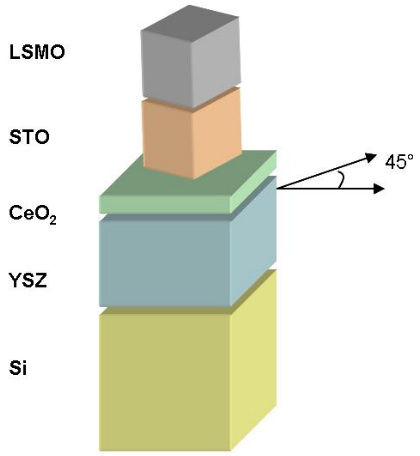

Figure 4.16. Sketch of the whole multilayer structure *STO*-based *LSMO* films.

The refined positions of the investigated *STO* and *LSMO* peaks are reported in Tabs. 6.11, 6.12, 6.13 for three samples of different *LSMO* thickness. The average *out-of-plane* parameter of *LSMO* films on *STO*-based buffered *Si* is 0.3845nm, 0.3848nm, and 0.3865nm, for a 50nm, 32nm and 10nm thick films, respectively. This means that the *LSMO* cell shows a slight ***in-plane compressive strain***, resulting in a slight c-axis expansion. It has to be compared to the value of 0.3865nm, which is typically measured on *LSMO* films on (001) *STO* substrates. The 50nm and 32nm thick *LSMO* are fully *in-plane* strained and matched with the *STO* underlayer (*in-plane* axis 0.3905nm). The *out-of-plane* axis is therefore compressed (0.3845 - 0.3848nm) of about 0.72% and 0.65% for the 50nm and 32nm *LSMO* thick layers, respectively.

4.3.2. Morphological properties of LSMO films on $STO/CeO_2/YSZ/Si$

Fig. 4.17*(left)* shows the *AFM* images of the *LSMO* (50nm thick) film surfaces grown using *STO* as the under top layer. The *STO-based* sample exhibits a clear columnar growth with a smoother surface ($RMS \approx 2,88nm$) in comparison with *BTO-based* multilayers ($RMS \approx 12nm$). However, as for the *BTO-based LSMO* previously discussed, the average roughness of the *LSMO* top layer is always higher than of *LSMO* films grown on (001) *STO* single crystal substrates ($RSM \sim 0.3nm$) (Sec. 3.2.2, Fig. 3.23) that usually show terraces indicating step flow growth. Also, the growth mode is different, that is, in the case of multilayers a 3D growth (i.e., free expansion of independent nuclei) is observed, at contrast with the case of the step flow regime observed for the growth on *STO* single crystals.

The choise of the under top *STO* thickness is of a great importance to avoid cracks at the *LSMO* surface, as shown in Fig. 4.17*(right)* for *STO* thickness above 80nm.

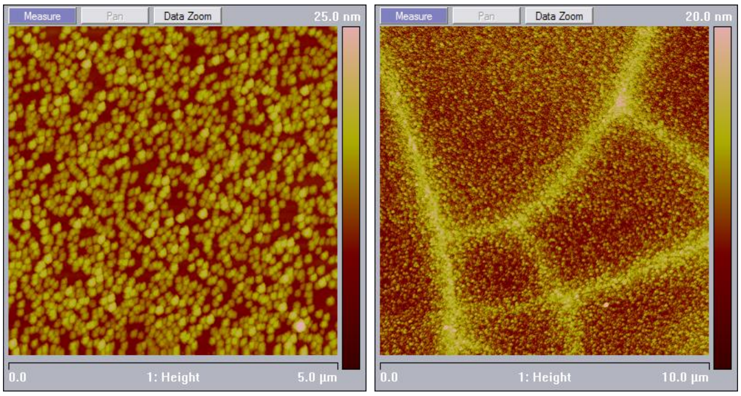

Figure 4.17. $5\mu m \times 5\mu m$ AFM images in the tapping mode of the $LSMO$ films ($50nm$ thick) on STO-based buffered Si for STO $50nm$ *(left)*. $10\mu m \times 10\mu m$ AFM images in the tapping mode of the $LSMO$ films ($50nm$ thick) on STO-based buffered Si for STO $80nm$ *(right)* thick.

4.3.3. Transport and magnetic properties of LSMO films on $STO/CeO_2/YSZ/Si$

Fig. 4.18*(left)* shows the temperature dependence of the $LSMO$ films with different thickness deposited on STO-based buffers. The low temperature resistivity of $50nm$ thick $LSMO$ ($\rho_0 \sim 0.7m\Omega cm$) is still one order of magnitude higher than that obtained for $LSMO$ grown on (001) STO single crystal ($\rho_0 \sim 0.08m\Omega cm$). I determined the Curie temperature by measuring the magnetization vs. temperature (Fig. 4.18*(right)*). The highest value of T_C was obtained for the $30nm$ thick sample ($T_C = 340K$) in comparison with $T_C = 320K$ for the thicker $LSMO$.

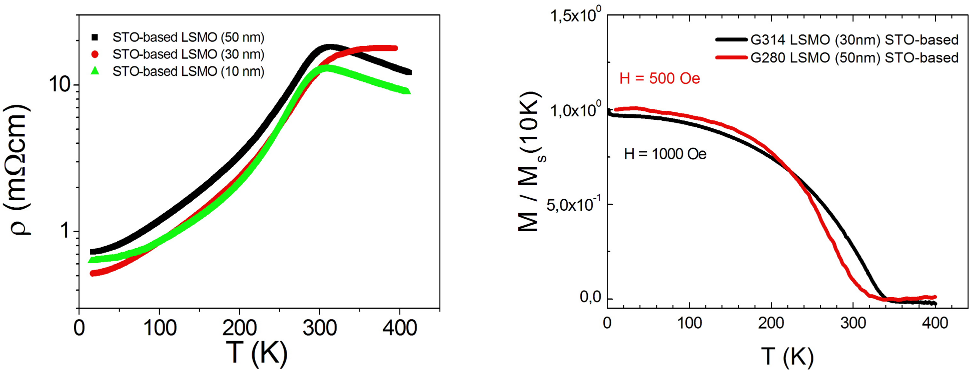

Figure 4.18. LEFT PANEL: Resistivity vs. temperature plots of $LSMO$ films on STO / CeO_2 / YSZ / Si (001) for $10nm$, $30nm$ and $50nm$ thick $LSMO$ thin films. RIGHT PANEL: Saturation magnetization vs. temperature.

4.4. Concluding remarks on LSMO films grown on buffered silicon

The best Curie temperature (T_C) values measured on these samples are $355K$ and $320K$, for the BTO-based and STO-based, respectively (Fig. 4.19*(left)*). This very high T_C value for films deposited on BTO buffers is mainly ascribed to the presence of compressive strain (Sec. 1.5). However, as already stated, compared them with $LSMO$ films deposited on STO single crystal substrates, the resistivities at low temperature are one order of magnitude higher (Fig. 4.19*(right)*), the saturation magnetization 3 times lower and the average roughness still higher.

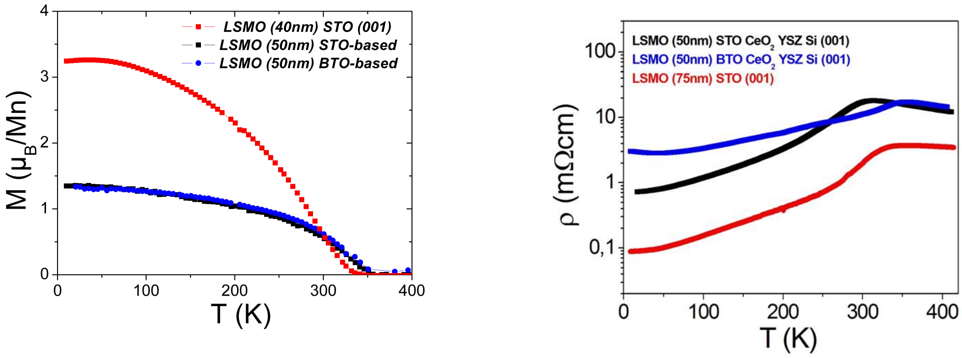

Figure 4.19. Magnetization vs. temperature *(left)* and resistivity vs. temperature *(right)* of *LSMO* grown on *BTO-based*, *STO-based* and *STO* single crystal substrate.

To complete the characterization of the *LSMO* multilayers, low frequency noise measurements were performed at the *GREYC* laboratory. In Fig. 4.20 the normalized Hooge parameter (α_H/n) (see Eq. 2.4) is reported for $25nm$ thick *LSMO* films on buffered silicon substrates and for *LSMO* films of different thicknesses deposited on *STO* and vicinal substrates for comparison. α_H/n values of these multilayers were found in the $9 \times 10^{-29} - 2 \times 10^{-27} m^3$ range, while the values measured in *LSMO* of the same thickness deposited on standard (001) *STO* and on vicinal were in the $5 \times 10^{-31} - 1 \times 10^{-28} m^3$ range. The noise level is therefore found to be one or two orders of magnitude higher than what was typically measured in the best *LSMO* films deposited on *STO* single crystals [4, 67, 116, 117]. Moreover, the measured noise level of *STO*-based is always lower than what measured on *BTO*-based *LSMO*. This feature confirms a dependence of the electronic noise on the crystal quality and surface morphology of the films. In fact, the rocking curves and the *AFM* scans demonstrated that the *LSMO* grown on *STO*-based always showed smaller *FWHM* and average roughness than the *LSMO* deposited on *BTO*-based.

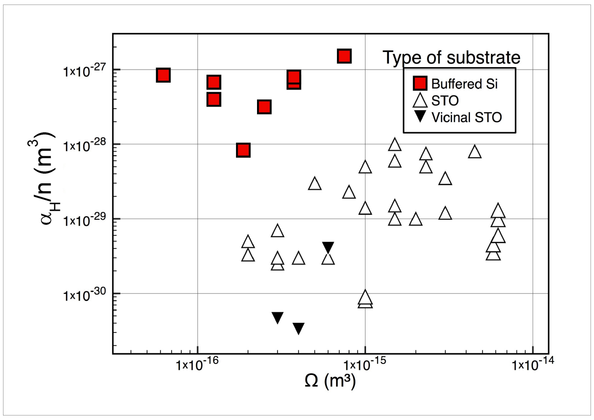

Figure 4.20. Normalized Hooge parameter values (α_H/n) of $42nm$ thick *LSMO* films grown onto vicinal (001) *STO* substrates (black triangle) compared to those obtained on *LSMO* films on (001) *STO* and buffered Silicon substrates of the same thickness.

Tab. 4.5 shows the main results obtained for the multilayers studied in this chapter compared to the best results found in literature. To be noted the reasonable high *TCR*, close to what obtained for *LSMO* deposited on *STO* single crystal and the lower α_H/n values that the multilayers show in respect to what obtained by Kim *et al.* on similar samples [75].

Ref.	*Composition*	$T(K)$	$TCR(K^{-1})$	$\alpha_H/n(m^3)$
p.w.	$La_{0.7}Sr_{0.3}MnO_3/\ STO$	300	+0.030	9×10^{-31}
p.w.	$La_{0.87}Sr_{0.13}MnO_3/\ STO$	290	+0.049	$\sim 10^{-31}$
[78]	$La_{0.7}(Pb_{0.63}Sr_{0.37})_{0.3}MnO_3/\ LAO$	300	+0.074	3×10^{-27}
[76]	$La_{0.72}Sr_{0.28}MnO_3/\ STO$	300	+0.025	2.2×10^{-32}
p.w.	$La_{0.7}Sr_{0.3}MnO_3/$ buffered *Si*	300	+0.028	9×10^{-29}
[75]	$La_{0.7}(Sr, Ca)_{0.3}MnO_3/$ buffered *Si*	294	+0.044	1.6×10^{-26}

Table 4.5. *TCR* coefficients, *Hooge normalized parameters* a_H/n at $30Hz$ and $300K$ of *LSMO* films of different composition compared with other materials used as room temperature thermometers. p.w. = present work.

Concluding this chapter, I obtained *LSMO* films of overall good quality that are considering as already suitable for use in device fabrication on both the considered multilayered structures grown on silicon substrates, i.e. *BTO*-based and *STO*-based *LSMO*. These promising results constitute the first step toward the integration of the oxides compounds with the conventional electronics at *GREYC*, with particular reference to the fabrication of *IR* detectors on *Si* membranes.

Chapter 5

Transport and magnetic properties of LSMO films

The *CMR* effect in manganites is explained by the interplay between the *DE* term that promotes the hopping of the carriers, and the strong interaction between electrons and lattice distortions (see Chap. 1). The strong sensitivity to the magnetic field in *LSMO* is found (in the doping range $0.2 < x < 0.5$) at temperatures around the ferromagnetic-paramagnetic transition (FPT) (Curie temperature T_C) that is close to the temperature T_P where a peak in the resistivity marks the metal-insulator transition (*MIT*) [118]. The interplay between the Mn magnetic moments alignment and the metallic behaviour is usually explained by invoking the *DE* interaction [15], that, however, only qualitatively accounts for the properties around the combined FPT and *MIT* [33]. As shown by many experimental results [33, 118], other interactions, mainly the coupling of the charge carriers with lattice, cooperate to drive the *MIT* and the *CMR* effect. Actually a Jahn-Teller distortion of the oxygen octahedron can lead to the trapping of the charge carriers (*polaron*) influencing the transport properties in the high temperature phase. In these compounds the *MIT* is affected by the crystal structure also because of the dependence of the $Mn - Mn$ electron transfer matrix element on the $Mn - O - Mn$ bond angle whose variation is a function of the radii of La^{3+} and Sr^{2+} cations [119].

The comprehension of the role of the strain due to lattice mismatch between the substrate and the film is an essential issue for any possible application of manganite films. Indeed, it has been found that properties such as the temperature T_C, the resistivity, the transport and magnetic anisotropies, the magnetoresistance, and the spin and orbital order structure are sensitive to the *epitaxial strain* [37, 38, 39, 40]. The effect of the epitaxial strain is different from that of the hydrostatic or chemical pressure, since *in-plane* strain generally leads to an *out-of-plane* strain of different sign (Sec. 1.5). The effects induced by the substrate are able to influence the tendency toward phase separation, induce inhomogeneities in films, and cause new electronic behaviours not found in bulk materials of the same composition [41, 42]. Actually, the strain affects so many quantities that it could be used to control the properties of interest by depositing films on various substrates, changing the deposition conditions and the postannealing procedure, and varying the thickness [50]. Moreover, most technological applications involve films, and films typically have a large biaxial strain because of lattice mismatch with the substrate.

Many effects of the strain in the *CMR* materials are well known. As an example, the magnetic anisotropies in thin films have been interpreted in terms of the stress due to the substrate [5, 115, 120, 121]. By depositing films on vicinal substrates we can also control the arrangement of the magnetic domains [100], as it will be discussed in Chap. 6.

In this chapter I will focus the attention on the *MIT* and on the phase separation (PS) that occurs around the room temperature in *LSMO* films (Fig. 5.1). Due to the relevance of the strain induced by the substrate and/or by the buffer layers on the electronic and magnetic properties in such compounds, the behaviour of the T_C versus strain in *LSMO* films is investigated and interpreted in the framework of the current theory [43].

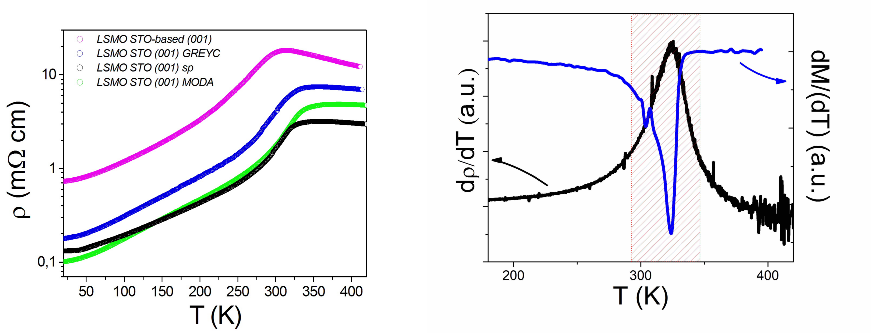

Figure 5.1. Left panel: $\rho(T)$ of the *LSMO* films grown on (001) *STO* and on *STO*-based substrates by sputtering and laser ablation. Right panel: $d\rho/dT$ and dM/dT remark the *PS* region (coloured) around the *MIT* and *FPT*.

5.1. Electrical transport in LSMO

In the low temperature region, i.e. fully inside the *FM* phase, several T-power laws have been proposed to fit the experimental $\rho(T)$. The law $\rho = \rho_0 + aT^2$, with ρ_0 residual resistivity, has been proposed to fit the data of single crystals in the low temperature range [118, 122]. For the majority spin electrons, the temperature dependence of the resistivity due to the electron-electron (*el-el*) scattering would provide the T^2 dependence. However, the T^2 term is much larger than expected for this type of scattering [118]. Another source for the T^2 behaviour could be the scattering involving a spin-flip process (magnon scattering) [123], but in a truly half ferromagnetic metal (*HFM*) system this process is suppressed since there is a band gap at the Fermi energy for one of the spin channels (high spin polarization, see Sec. 1.2). On the other hand, the scattering that involves two spin-flip processes gives a $T^{9/2}$ dependence [124], that is in disagreement with experimental data. Therefore, in order to explain the behaviour of ρ, it has been argued that in single crystals at intermediate temperatures the observed contribution could reflect the reappearance of minority spin states that become accessible to thermally excited magnons [118]. Of course, this single magnon process becomes possible only if the spin polarization strongly decreases from unity with increasing T.

In any case, in single crystals some experiments have found variations in the temperature scaling of ρ from T^2 to T^3 behaviour, that is interpreted in terms of spin fluctuations (anomalous single magnon scattering) process [125]. In *LCMO* systems the electrical resistivity below T_C has been fitted also by a $T^{2.5}$ dependence [126]. This nonconventional result has been interpreted in these nearly *HFM* compounds taking into account a finite density of states of the minority spins at Fermi energy and their Anderson localization [127]. The spin-flip scattering involving single magnons gives in fact a $T^{2.5}$ temperature dependence of the resistivity as result of the exact solution of the linear response equation.

In conclusion, the transport properties at low T in films are considered to be strongly influenced by the single magnon scattering.

In order to assess the properties of the *LSMO* films that I grew, I studied the resistivity vs. temperature behaviour of the samples characterized in Chaps. 3 and 4 following the procedure reported in [20]. Thus, the $\rho(T)$ plots in the low temperature region, i.e. fully inside the *FM* phase, of all the samples were been fitted by the following function

$$\rho_{FM} = \rho_0 + AT^\alpha \tag{5.1}$$

with ρ_0, the constant A, and α free parameters. Here ρ_0 is the residual resistivity that is considered as a measure of the effective disorder, and AT^α a generic T-power law which can simulate different scattering processes.

Typical values of the residual resistivity (ρ_0) are always less than $1m\Omega cm$ in the $LSMO$ films grown on STO single crystal substrates as reported in the Chap. 3. Otherwise, the anomalous large value found in $LSMO$ films grown on BTO-based buffered Si substrates ($\rho_0 \sim 3m\Omega cm$) is acribed to the grain boundary resistance. As observed by Gupta *et al.* [128], even grains of the order of $10\mu m$ have strong effects on both ρ_0 and $\rho(T)$ at low temperatures. In fact, due to the scattering at grain boundaries, the ρ_0 becomes higher and $\rho(T)$ power law changes, too. The topographies show that the $LSMO$ films grown on STO may be regarded as single crystals, i.e. no grain boundary region is evident in this case. This idea is enforced by TEM measurements (Fig. 3.34) that do not reveal any structural defects (see Sec. 3.2). On the contrary, inhomogeneities and grains are found on the surface of $LSMO$ grown on BTO-based buffered silicon (see Sec. 4.2.2). The films grown on BTO buffers have other anomalies: a broad maximum in the $\rho(T)$ at T_C, a minimum ρ at $\sim 50K$, a high α_H/n value. For all these reasons, I did not include the measurements performed on such samples in the following analysis.

In Fig. 5.2 I plot the resistivity measurements and the corresponding fits to Eq. 5.1 of the representative $LSMO$ films grown onto STO substrates and STO-based buffer in the $20K - 100K$ range of temperature. The $20K$ lower bound was chosen in order to avoid the effects due to the upturn of $\rho(T)$ at low T due to localization [118]. In Tab. 5.1 I report the parameters ρ_0 and α defined in Eq. 5.1 as they resulted from the fit procedures. A is always of the order of $10^{-9}\Omega cmK^{-\alpha}$. The fit provides an excellent approximation of the experimental data (R^2 very close to 1) and the uncertainty of the fit parameters results in $\Delta\rho_0 = \pm 0.01m\Omega cm$ and $\Delta\alpha = \pm 0.1$.

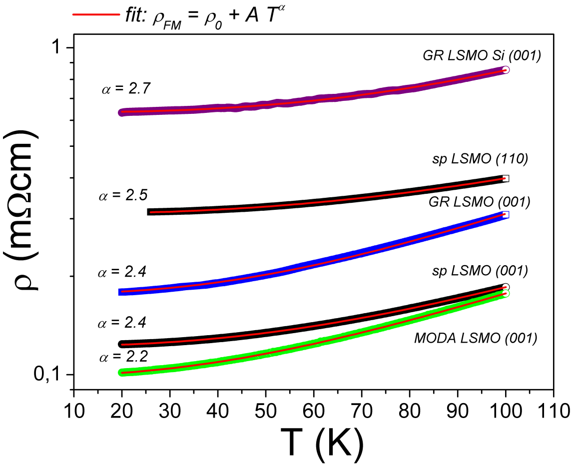

Figure 5.2. Resistivity measurements and the corresponding fits of representative samples in the range of temperature $20 - 100K$.

The comparison of the data in Tab. 5.1 suggests the following considerations on the reliability of the values of the fit parameters. First of all, the statistical error on ρ_0 can be considered negligible. The overall error is due to the experimental uncertainty on the geometrical factor in the four probe resistivity measurement, that is a systematic error that does not affect the estimation of α. Also the choice of the lower limit of the temperature range deserves attention, because of the shallow upturn of resistivity at low temperature. The analysis of the data leads to the conclusion that an overall uncertainty $\Delta\alpha = \pm 0.1$ stems from the different possible choices of the temperature range, and it is the uncertainty of the whole procedure (measurement and fit session). Other experimental and statistical effects are in fact negligible. As an instance, the error due to the thermal coupling of the samples (i.e., the finite value of dT/dt during the measurements, with consequent shift of temperature between sample and thermometer) is well below 0.1 in all measurements.

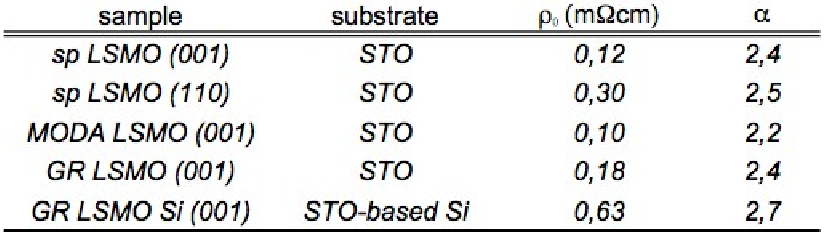

sample	substrate	ρ_0 (mΩcm)	α
sp LSMO (001)	*STO*	*0,12*	*2,4*
sp LSMO (110)	*STO*	*0,30*	*2,5*
MODA LSMO (001)	*STO*	*0,10*	*2,2*
GR LSMO (001)	*STO*	*0,18*	*2,4*
GR LSMO Si (001)	*STO-based Si*	*0,63*	*2,7*

Table 5.1. Fit results on *LSMO* samples obtained from different growth techniques analyzed in the $20-100K$ range of temperatures.

An alternative model, based on the relation $\rho(T) = \rho_0 + AT^2 + BT$ does not provide an acceptable fit. This result points out that the gradual variation of α cannot be ascribed to a combination of different power laws, as previously assumed [126]. In Fig. 5.2 I show the evidence of a correlation between the residual resistivity and fitting parameter α. In the case of *LSMO* films produced by M.O.D.A., ρ_0 is among the lowest values ever reported in literature for *LSMO*, and α is not far from the value of single crystals. All other samples deposited on *STO* show α close to 2.5. This behaviour, as previously pointed out, finds a natural explanation within a theory that considers the role of the disorder in nearly *HFM* systems [127]. The case of *LSMO* grown on buffered *Si* is instead similar to that of less ordered samples [20, 125]. All these samples have $\rho_0 < 1m\Omega cm$ and α value equal to 2.5 within the estimated error bar. The data show a slight deviation from $T^{2.5}$ dependence for both high and low ρ_0. In particular, for $\rho_0 \geq 0.6m\Omega cm$ the α exponent approaches the value 3. The value $\alpha = 3$ has been previously interpreted as due to an anomalous single magnon scattering, that is proportional to the one-electron bandwidth of the e_g carriers [125]. With increasing the strength of the disorder, it is possible that the effective bandwidth of the itinerant charge carriers gets reduced. Finally in the regime of small disorder $\rho_0 \leq 0.1m\Omega cm$ the α exponent tends toward the value 2 that is characteristic of single crystals.

I will now analyze the transport properties at high temperature (Fig. 5.3) pointing out the strong interplay between disorder and electron-phonon (*el-ph*) coupling in determining the insulating phase. The transport properties in the *PI* phase (Sec. 1.3) are typically described in terms of polaronic conduction stressing the role of the *el-ph* interaction in driving the *MIT* [118]. For $T > T_P$ the resistivity is characterized by an activated behaviour described by the following law

$$\rho_{PI} = \rho_\infty exp\left\{\frac{E_0}{k_B T}\right\} \tag{5.2}$$

with the activation energy E_0 of the order of $0.1-0.2eV$. However, the electrical conduction in *LSMO* in the high temperature phase can go from the regime described by Eq. 5.2, that is paramagnetic insulating (*PI*), to a paramagnetic metallic (*PM*) regime, where $\frac{d\rho}{dT} > 0$, for samples characterized by a very low amount of disorder.

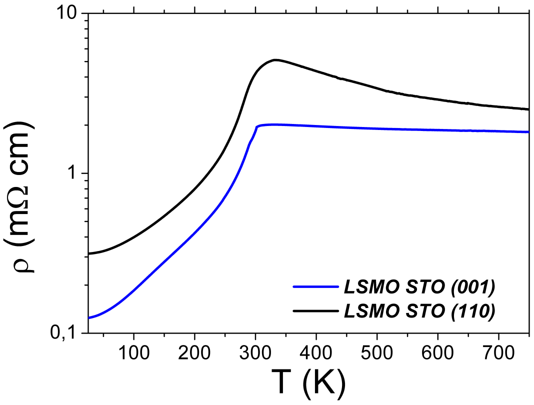

Figure 5.3. Resistivity vs. temperature for typical *LSMO* films grown by sputtering on (001) and (110) *STO*. The high temperature $\rho(T)$ were recorded in air, with mechanically pressed electrical contacts.

In order to interpret the transport properties in the whole range of T, I resorted to the model reported in [20], based on the phase separation scenario [118, 41], that yealds:

$$\rho(T) = \rho_{FM} \cdot f + \rho_{PI} \cdot (1 - f) \tag{5.3}$$

where ρ_{FM} is given by Eq. 5.1 and ρ_{PI} is the resistivity of the high temperature phase (Eq. 5.2). The function f represents the volume fraction of the FM regions in the system while $(1 - f)$ represents the paramagnetic one [129]. This function has a value equal to unity at low temperatures, it is decreasing with increasing T and it goes to zero in the PI phase.

The fitting functions in the low and high temperature region, given by Eqs. 5.1 and 5.2, respectively, are extrapolated to the whole temperature range, so the distribution function f is extracted using for $\rho(T)$ in Eq. 5.3 the experimental data. The samples in Fig. 5.3 have residual resistivities smaller than $1m\Omega cm$, therefore at low temperature the temperature dependence of ρ is dominated by the $T^{2.5}$ contribution. At high T both film resistivities show an activated behaviour, so the best two-parameter fit is given by Eq. 5.2. The *LSMO* grown on (110) *STO* shows a sharp maximum in the resistivity that in the range $500K - 800K$ is well described by Eq. 5.2 with $\rho_\infty \propto \sqrt{T}$ and an activated energy E_0 equal to $64.37meV$. Instead, the the *LSMO* grown on (001) *STO* is on the verge of the metallic phase. In fact the resistivity is weakly decreasing and the activation energy is an order of magnitude smaller than that of (110) *LSMO*. In conclusion, I can confirm that the different behaviour of the resistivities of two samples correlates with the decrease of the residual resistivity, so that the samples with lower ρ_0 show better metallic behaviour at the high temperature. Finally, these data seem to confirm the possible coexistence of two phases in a wide range around T_C: the first one is insulating, and it is characterized by localized states; the second one is metallic, with delocalized states.

A further, direct evidence of the *PS* in *LSMO* can be achieved by resorting to *STM* measurements in the conductance map mode. In this mode of operation, the false color in the map is a measure of the conductance of the junction beween the *STM* tip and the sample. The maps must be recorded at fixed junction voltage and after disconnecting the *STM* feedback [42]. The conductance maps confirm the existence of inhomogeneities at the Curie temperature. In Fig. 5.4 I report two conductance maps, recorded at $77K$ and $300K$ respectively. The sample is a *LSMO* film deposited by sputtering on a (110) *STO*. The map of tunneling conductance in Fig. 5.4, taken at different temperature values, reproduces in light color the highly conductive regions, that according to the present understanding are ferromagnetic, while dark regions are insulating and hence paramagnetic [42]. A naive approach within the Stoner-Wohlfarth model would then suggest that the separated, ferromagnetic regions, behave as ferromagnetic nanoparticles, and therefore possess an enhanced coercive field until, reducing the temperature, the percolation of ferromagnetic regions is complete [42].

At $77K$, well below T_C and therefore fully in the ferromagnetic state, dI/dV maps do not show evidence of inhomogeneities on any measured sample (Fig. 5.4*(a)*). In contrast, maps at room temperature, carried out at $297K$, just below T_C, systematically show islands with sharply different spectroscopic features (Fig. 5.4*(b)*). It is interesting to note that the tunneling dI/dV values recorded at $77K$ are close to the values observed in the $297K$ maps in the light gray regions.

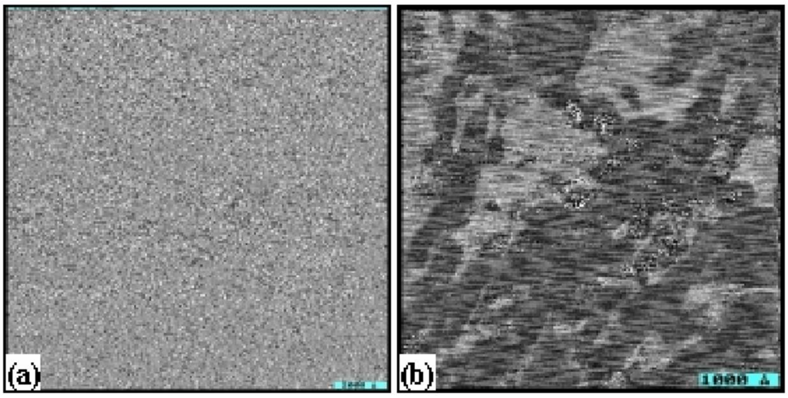

Figure 5.4. Tunnel conductance maps at $77K$ (a) and at $300K$ (b) of the $LSMO$ film deposited onto (110) STO substrate [42].

The coexistence of high and low conductivity regions at room temperature is also demonstrated by the $I-V$ characteristic performed by STS in the conductive and insulating regions (brigh and dark in Fig. 5.4*(b)*) (Fig. 5.5).

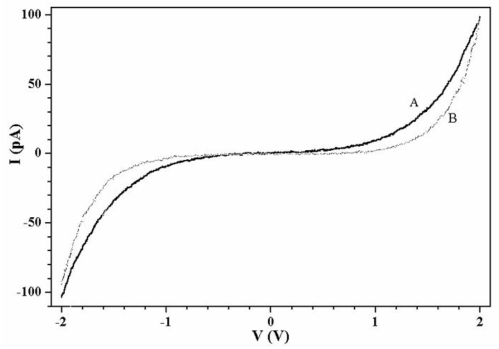

Figure 5.5. $I-V$ characteristic performed by STS on the conductive *(A)* and insulating *(B)* region of Fig. 5.4*(b)* (bright and dark, respectively). The voltage $V = 1.5V$ was chosen to record the map in Fig. 5.4 to enhance the contrast.

5.2. Dependence of T_C on strain in LSMO films

In the following, I interpret the results obtained on $LSMO$ films grown on STO single crystal substrates deposited by different techniques and on silicon buffered substrates fabricated using the laser ablation technique in the framework of the current theory of the strain dependence of T_C [43, 41].

5.2.1. LSMO films grown on STO

The equation that links T_C to the bulk (ε_B) and biaxial strain (ε^*), discussed in Chap. 1 and defined by Eqs. 1.17, 1.18, is

$$T_C(\varepsilon_B, \varepsilon^*) = T_C^0[1 - a\varepsilon_B - b\varepsilon^{*2}] \tag{5.4}$$

where T_C^0 is the Curie temperature of the unstrained *LSMO*.

I evaluated by a fitting procedure T_C^0, a, and b for *LSMO* samples grown on (001) *STO* and compared them with the results found in literature. In all the cases T_C is evaluated by the $M(T)$ plot.

In Fig. 5.6 the values of the volume strain ε_B, the Jahn Teller strain ε^* and the Curie temperature T_C of the *LSMO* samples grown on (001) *STO* are plotted vs. film thickness.

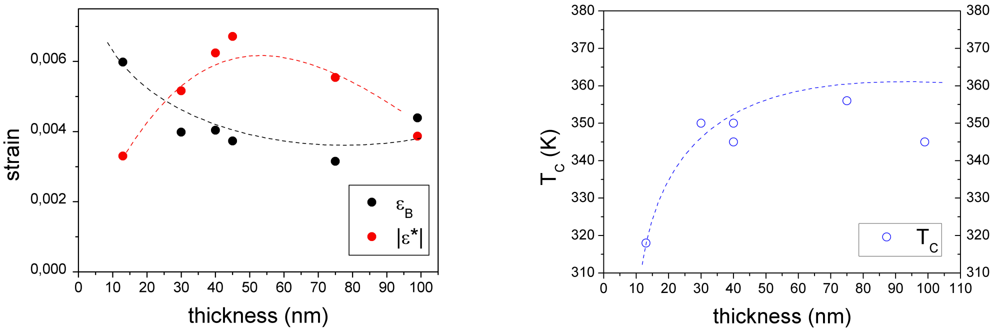

Figure 5.6. Plot of the volume strain ε_B, the Jahn Teller strain ε^* (*left*) and the Curie temperature T_C (*right*) of the *LSMO* samples grown on (001) *STO* vs. film thickness.

I excluded by the plot the data for sputtered films, whose behaviour is anomalous, probably due to a slightly variable and uncontrolled oxygen content.

Fitting the Eq. 1.16 using the data reported in Tab. 5.2 I determined the bulk Curie temperature $T_C^0 = 363K$, $a = \frac{1}{T_C^0}\frac{dT_C}{d\varepsilon_B} = 12$ and $b = \frac{1}{T_C^0}\frac{d^2T_C}{d\varepsilon^{*2}} = 1000$. The former is consistent with the predicted theoretical value of ~ 15 [43] for *CMR* materials with a strong *el-ph* coupling. The large value of $\Delta = 2b$, that is found ranging from 1000 to 2000 in the Ref. [44, 43, 130], reveal the importance of the *JT* distortions in such material. In fact, a biaxial strain as small as 1% leads to a reduction of 10% in T_C (ΔT_C in Tab. 5.2).

LSMO STO (001) pld	LSMO thickness (nm)	[100]-axis (nm)	[001]-axis (nm)	ε[001] (%)	ε[100] (%)	ε(b) (%)	ε* (%)	Tc (K)	ΔTc (K)
GREYC	30	0,3902	0,3862	-0,28	0,75	0,40	-0,52	350	-13
GREYC	40	0,3905	0,3865	-0,21	0,83	0,40	-0,62	345	-18
GREYC	75	0,3900	0,3857	-0,41	0,70	0,32	-0,55	345	-18
GREYC	99	0,3900	0,3867	-0,15	0,70	0,41	-0,43	350	-13
MODA	13	0,3905	0,3880	0,18	0,83	0,60	-0,33	318	-45
MODA	45	0,3905	0,3853	-0,52	0,83	0,37	-0,67	335	-28

Table 5.2. Lattice parameters and strain values of *LSMO* films grown on *STO* single crystal substrates utilized for the strain calculations. $\varepsilon_{[001]}$ and $\varepsilon_{[100]}$ represent the *out-of-plane* and *in-plane* strain components, respectively, while ε_B is the *bulk compression* and ε^* is the *biaxial strain*. T_C values were determined experimentally by magnetic measurements. $\Delta T_C = T_C - T_C^0$ has been obtained after the fitting.

5.2.2. LSMO films grown on buffered Si

In *YSZ-based LSMO* multilayers (Secs. 4.2 and 4.3), the strain induced by the under top layer (*BTO* or *STO*) affects the *LSMO* top layer properties as it happens in the case of *LSMO* grown on single crystal substrates. Due to the different mismatches the *LSMO* cell is subject to a *compressive* (or *tensile*) strain if it is grown on *BTO*- (or *STO*-) based buffer.

The *in-plane* and the *out-of-plane* lattice parameters of the considered multilayers are listed in Tab. 5.3.

	LSMO thickness	out-of-plane axis (nm)	in-plane axis (nm)	ε[001] (%)	ε[100] (%)	ε(b) (%)	ε * (%)	Tc (K)	ΔTc (K)	ρ (mΩcm) @ 300K
BTO-based	50 nm	0,3880	0,3838	0,18	-0,90	-0,54	0,54	355	10	10,0
BTO-based	25 nm	0,3893	0,3864	0,52	-0,23	0,02	0,37	340	-5	9,2
STO-based	50 nm	0,3845	0,3906	-0,72	0,85	0,33	-0,79	320	-25	10,0
STO-based	32 nm	0,3848	0,3905	-0,65	0,83	0,34	-0,74	340	-5	11,0
STO (001)	40 nm	0,3858	0,3905	-0,39	0,83	0,42	-0,61	345	0	2,0

Table 5.3. Lattice parameters and strain components of the *LSMO* top layers for *BTO*- and *STO-based* samples compared with *LSMO* grown on *STO* (001) single crystal substrate. The considered unstrained *LSMO* bulk lattice constant is $0.3873nm$. $\varepsilon_{[001]}$ and $\varepsilon_{[100]}$ represent the *out-of-plane* and *in-plane* strain components, respectively, while ε_B is the *bulk compression* and ε^* is the *biaxial strain*. $\Delta T_C = T_C - T_C^0$ has been obtained after the fitting. ρ_{300K} is the room temperature resistivity calculated from the $\rho(T)$ curves.

Fitting the data reported in Tab. 5.3 by Eq. 1.16, I determined the bulk Curie temperature $T_C^0 = 345K$, $a = \frac{1}{T_C^0}\frac{dT_C}{d\varepsilon_B} = 5$ and $b = \frac{1}{T_C^0}\frac{d^2T_C}{d\varepsilon^{*2}} = 313$. The value of a is much less than obtained for *LSMO* deposited on *STO* single crystals. However, Thiele *et al.* [130] reported a value of 6.0 for *LSMO* films deposited on piezoelectric substrates while Eom *et al.* [44] found 2.2 considering *LSMO* films grown on *STO*, *LAO*, *NGO* and *LSAT* substrates. Furthermore, b is found to be less than what otained for *LSMO* grown onto *STO* single crystals, demonstrating a weaker *JT* distortion.

5.3. Magnetic properties of LSMO films

In the following, I synthesize the results of the basic magnetic characteristic of the films, as evaluated by the usual $M - H$ hysteresis loops.

5.3.1. LSMO films grown on STO

As discussed in Sec. 3.3, both in-plane axes of films grown on (001) STO are fully strained to match the substrate while the vertical axis is somewhat shortened. According to the general rule observed for $LSMO$, that the positive strain results in an easy magnetization direction, the ***easy*** axes in films deposited on (001) STO are aligned with the principal in-plane directions [100] and [010], while the ***hard*** axis is aligned to the vertical (***out-of-plane***) [001]. The data reported in Fig. 5.7*(left)*) confirm this statements, and are in full agreement with reported results [27].

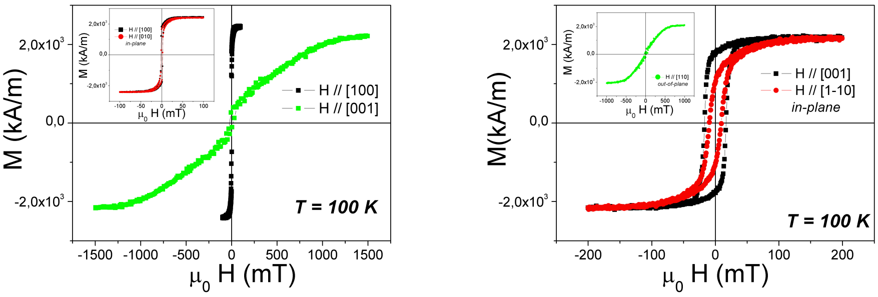

Figure 5.7. Left panel: $M(H)$ at $100K$ for a $LSMO$ film grown on (001) STO. Inset: $M(H)$ loop with H applied along the two *in-plane* directions. Right panel: $M(H)$ at $100K$ for a $LSMO$ film grown on (110) STO. Inset: $M(H)$ loop with H applied along the [110] *out-of-plane* axis.

The case of (110) STO substrates is different. In fact, the different strain mechanism induced by the substrate leads to ***in-plane*** anisotropy [120, 25]. Thus, two inequivalent ***in-plane*** directions of magnetization exists. Fig. 5.7*(right)* shows the hysteresis loops at $100K$ for a sample grown on (110) STO, with the field aligned along the two ***in-plane*** principal axes. The easy axis is parallel to the [001] direction, while the $[1\bar{1}0]$ is a hard axis, characterized by a smaller hysteresis and a higher saturation field. The free energy of the system can be written in this case:

$$E = E_{ex} + Kcos^2\theta - M \cdot H \tag{5.5}$$

where K is the ***in-plane*** anisotropy constant, θ is the angle between the magnetization vector M and the (001) easy direction, and E_{ex} is the exchange energy (Sec. 1.4). K can be determined by considering the loop with the external field H applied along the hard axis of magnetization. The equilibrium condition $\frac{\partial E}{\partial \theta}\,|_{H=H_S}= 0$ yields $K_{(@T=100K)} = -M_S H_S/2 = -2.7 \times 10^4 J/m^3$ with $H_S = 100mT$ the saturation field in the hard direction. In terms of the magnetostriction constant λ (Sec. 1.4) and strain ε (Secs. 1.1.1, 1.5), the induced anisotropy can be written as $K_{stress} = -3\lambda\varepsilon Y/2$ where Y is Young's modulus [22]. Assuming that $\lambda_{(@T=100K)} = 2.2 \times 10^{-5}$ [25] and $Y = 5 \times 10^{11}\ N/m^2$ [28] yields $\varepsilon = 0.8\%$, which corresponds to the film/substrate lattice misfit. The $M(H)$ loop with field applied along the [110] direction, i.e., perpendicular to the film plane, is shown in the inset of Fig. 5.7*(right)* for a $30nm$ thick film. The measured anisotropy field of $H_K \sim 0.7T$ is equal to the demagnetizing field $\mu_0 M_S = 0.69T$ within less than 2% of accuracy. The agreement indicates that, to within $2.7 \times 10^2 J/m^3$, there is no perpendicular uniaxial anisotropy.

In Fig. 5.8 I compare the $M(H)$ loops at $100K$ and at $300K$ for a sample grown on (110) *STO*. The field is aligned to the $[1\bar{1}0]$ direction in this case. It is found that H_C decreases from $17mT$ at $100K$ to $6mT$ at $300K$. This noticeable reduction of the loop width with temperature is indicative of an enhanced mobility of the *DW*s, that is due to a thermal activation mechanism. This effect may be partially contrasted by the phase separation that takes place in a temperature region around the Curie temperature, and that it is demonstrated by scanning tunneling measurements (Fig. 5.4).

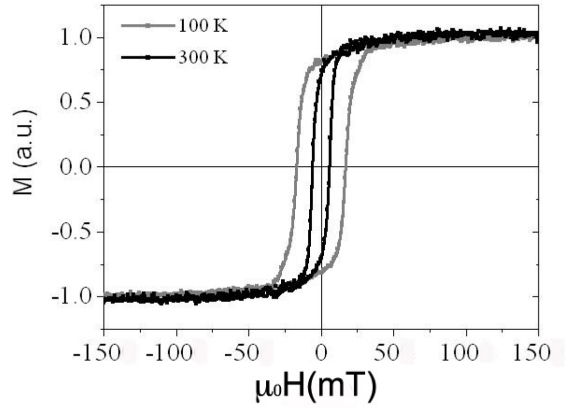

Figure 5.8. $M(H)$ for a *LSMO* film on (110) *STO* at $100K$ and $300K$.

Conluding, the magnetic properties of such samples confirm that *LSMO* has strong *magnetostrictive effects*. The results can be interpreted in the framework of the fundamental mechanisms of ferromagnetic ordering in manganites, i.e. by the double exchange [32]. The ferromagnetic coupling is determined by the nature of the $Mn - O - Mn$ bonds, that are affected by the strain. The details of cell deformation are however different for samples grown on (110) and (001) *STO* (see Fig. 1.4). In the former case, the tensile biaxial stress acts by applying a shear stress to the *LSMO* cell. Shear is instead absent in the latter case. Therefore, the $Mn - O$ bond length and on the $Mn - O - Mn$ angles are modified in different ways. In particular, the distance between nearest neighbors Mn cations along the $[1\bar{1}0]$ direction is scarcely modified in the strained *LSMO* grown on (110) *STO*, because the stress does not change the length of the [100] and [010] axes, but instead their angle. Thus, the in-plane anisotropy of (110) samples can be explained assuming that the magnetostrictive effect depends on the axes length, and only to a minor extent on cell angles. Therefore, the in-plane easy axis is expected to lye along the [001] direction, that is an elongated axis, as it is in fact observed, while the $[1\bar{1}0]$ is comparatively harder.

5.3.2. LSMO films grown on buffered Si

Finally, I studied the magnetic in-plane anistropy induced on the *LSMO* by the under top layer, *BTO* and *STO*, along the $[100]_{LSMO}$ (side of the *LSMO* cell) and $[110]_{LSMO}$ (in-plane diagonal of the *LSMO* cell). The $M(H,T)$ loops of the *BTO*- and *STO*-based *LSMO* sample, $50nm$ thick, are shown in (Fig. 5.9). These measurements were performed by applying the magnetic field (H) along the $[110]_{Si} \parallel [100]_{LSMO}$ and $[100]_{Si} \parallel [110]_{LSMO}$ at $10K$ and at $300K$. Analyzing them, I only revealed slight difference in the low temperature coercive magnetic field H_C^{LT} values along the two different directions ($18.6mT$ along the $[100]_{LSMO}$ and $21.4mT$ along the $[110]_{LSMO}$) in the case of the *BTO*-based sample (Fig. 5.9*(left)*). In the case of the *STO*-based *LSMO* no *in-plane* anisotropy is found (Fig. 5.9*(right)*). At room temperature, the coercive field was $\sim 2mT$ in both cases. To conclude, I did not envisaged significant preferential direction of magnetization at room temperature. Moreover, at low temperature the grain diffusion at the surface could mask the effect of the *in-plane* anisotropy (inhomogeneities showed by the AFM images in Fig. 4.9).

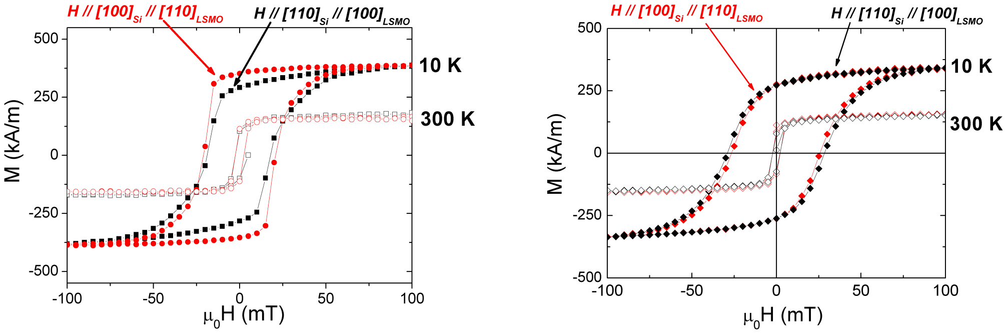

Figure 5.9. $M(H)$ loops in two *in-plane* crystallographic orientations for a $LSMO$ ($50nm$ thick) grown on BTO-based (*left*) and on STO-based (*right*) multilayer. The magnetization is recorded at $10K$ and $300K$ for each direction of the applied magnetic field (H).

Chapter 6

LSMO-based MR devices

As remarked in Sec. 1.2, *LSMO* is an almost perfect *half metal*, that is, the conduction band is mostly filled up with one orientation of spin. This can be exploited for spin injection application. In what follows, I discuss three differents experiments. The first one concerns *LSMO/Py* junctions. In the second I resort to vicinal *STO* substrate to induce *in-plane* anistropy in *LSMO* films. Finally, the third experiment is based on the fabrication of nanocostrictions. In all cases, the aim is to demonstrate the feasibility of magnetoresistive devices operating at low magnetic field (few mT).

6.1. Low field MR in LSMO/Permalloy interface

At the surface of all the magnetic materials, a thin layer with degraded (non magnetic) properties is usually present. The existence of such dead layer was demonstrated also for *LSMO*, by comparing the total magnetic moment of samples with different thickness [45]. Since in *LSMO* magnetism and transport properties are tightly bound, in this material the dead layer also affects the value of the electrical resistance.

Thus, the *dead layer* on the topmost of the *LSMO* film surface (see Sec. 1.5) can be exploited as a natural spacer at the interface, whether it is insulating or not, to obtain magnetoresistive devices (Fig. 6.1*(a)*). Unlike ferromagnetic metals, the thickness of the *dead layer* can be large enough to avoid magnetic exchange coupling between the manganite and a ferromagnetic counterelectrode deposited on it.

In this section, I show the study on the Current Perpendicular to Plane (*CPP*) magnetotransport behaviour of *LSMO* / $Ni_{80}Fe_{20}$ (*Permalloy* (*Py*)) in low magnetic fields. Due to the presence of a significantly thick *dead layer*, the layers only show a weak exchange coupling. The possibility of reversing the layers independently one of each other, can be exploited to fabricate magnetoresistive devices.

To this aim, I deposited *LSMO* films on (110) *STO* by *RF magnetron sputtering* as described in Sec. 3.1.1. The structural, transport and magnetic properties are discussed in Sec. 3.3 and Sec. 5.2. The thickness of the dead layer was estimated $\sim 5nm$ for these samples (Fig. 6.1*(b)*). The idea is that when a dead layer with thickness t_0 is present, the measured magnetic moment per unit area ($m\cdot t$) scales as $m\cdot t = M\cdot(t-t_0)$ being M the magnetization of the ferromagnetic *LSMO*.

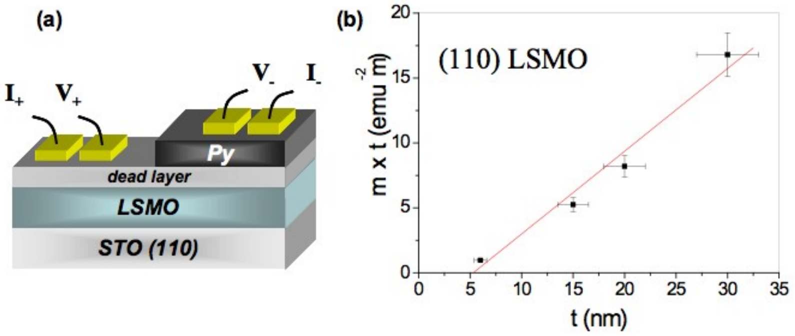

Figure 6.1. Schetch of the *Py / dead layer / LSMO* junction *(a)*; m vs. t for (110) sputtered *LSMO* films. *(b)*.

Polycrystalline $Ni_{80}Fe_{20}$ *Permalloy* (Py) layer was deposited by a DC sputtering technique at room temperature in a separate system in Ar atmosphere of $P_{Ar} = 5 \times 10^{-3} mbar$ on the *LSMO* film. It was found to be $fcc(111)$ textured. The rate of deposition was $0.1 nms^{-1}$. During the growth, a magnetic field of $50mT$ was applied in the plane of the film and along the *easy* axis [001] of the underlying *LSMO*, in order to induce an *easy* axis for the *Py* in the same direction.

The considered optimal thickness for *LSMO* and *Py* layers is $30nm$ and $10nm$, respectively. The $M(H)$ loop of the bilayer does not show a double coercivity at room temperature (Fig. 6.2). This is because the coercive field of the *LSMO* is close to that of the *Py* at this temperature. When the temperature is lowered down to $T = 4.2K$, the coercive field of the manganite increases more than that of the metal, revealing the double coercivity behaviour of the bilayer.

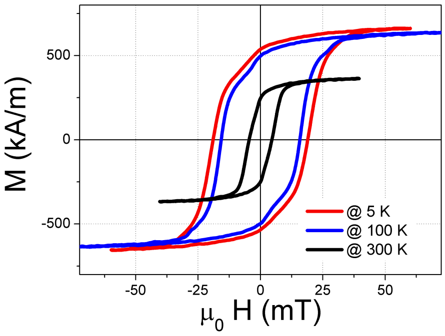

Figure 6.2. Magnetization vs. applied field of a bilayer *LSMO* ($30nm$) / *Py* ($10nm$) grown on (110) *STO*. The magnetic field was applied along the *in-plane* [001] easy axis.

By subtracting the $M(H)$ loop of an equivalent *LSMO* film from the $M(H)$ loop of the bilayer (Fig. 6.3), a coercivity of $3.6mT$ for the *Py* in the bilayer is estimated. This value is not far from a coercivity value of $3.2mT$ measured on a *Py* film of the same thickness at $4.2K$. Yet, the sharpness of the *Py* loop in the bilayer is smoothed as compared with that of the *Py* layer alone. The consequence of the smooth reversing of the *Py* magnetization is that the antiparallel (AP) configuration is not well established.

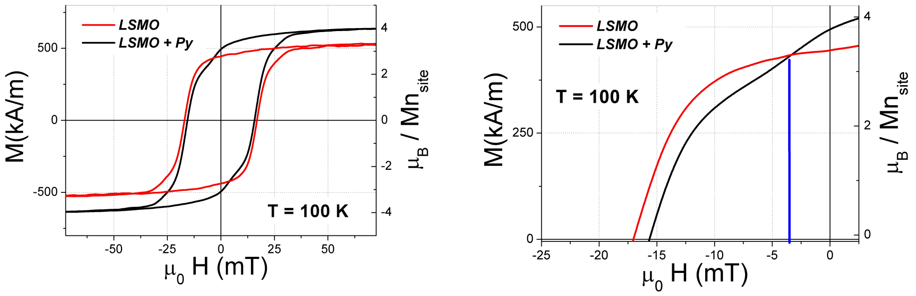

Figure 6.3. Left Panel: $M(H)$ loops of a $LSMO$ ($30nm$) film and of a $LSMO$ ($30nm$) / Py ($10nm$) bilayer at $T = 100K$. The magnetic field H is applied along the [001] easy axis. Right Panel: expanded region, showing the evaluation of the Py coercive field ($3.6mT$) in the bilayer.

The *CPP MR* of the bilayer as a function of the external applied magnetic field was measured at $T = 4.2K$ (Fig. 6.4(*left*)). Part of the *LSMO* surface was preserved uncovered to allow for electrical contacts, by resorting to a shadow mask during *Py* deposition. Four contacts were bonded in line with the easy axis of magnetization (see inset of Fig. 6.4*(left)*). The external magnetic field was applied in the same direction.

The $R(H)$ shows hysteresis with maximum peaks corresponding to the coercivity of the *LSMO*. It is not dependent on the bias current, in agreement with the measured linear dependence of the voltage (V) on the current (I). The maximum change in resistance, measured as $MR_{max} = -\Delta R/R_{H_C} = -\frac{[R(600Oe)-R(H_C)]}{R(H_C)}$, where H_C is the coercivity of the *LSMO*, is 1.7%.

The measured magnetoresistance cannot be attributed to the AMR effect of *Py*, even though values of the order of 1% can be achieved for this material, because in this case the maximum would have occurred at the coercivity of the *Py* in the bilayer. Moreover, the observed MR_{max} is too large to be attributed to the single *LSMO* layer. MR_{max} was, in fact, reported [121] not to be larger than 0.3% for *LSMO* epitaxial films in a range of magnetic field wider than the one utilized in this work. An AMR effect as large as 15% has been observed in polycrystalline *LSMO* films at low temperatures [121] because of spin-dependent scattering of polarized electrons at the grain boundaries. Although the x-ray analyses, performed before and after the deposition of *Py*, indicate a high degree of epitaxy of the *LSMO* films, the value of the AMR was checked in order to exclude any possible misinterpretation of the data. Fig. 6.4(*right*) shows the current in-plane *CIP-RH* curve of a $100nm$ wide patterned track. MR_{max} was always smaller than 0.3% as expected. In conclusion, the only AMR effect cannot explain the magnitude of the change of resistance measured on the bilayer.

An additional spin-dependent scattering of polarized electrons must be present at the *LSMO* / *Py* interface. Yet, if the bilayer were behaving as a spin valve, an abrupt increase of resistance should take place at the coercivity of the *Py*, while it increases smoothly. Also, $R(H)$ should saturate and reach a minimum in correspondence with the saturation field of the $M(H)$ loop of Fig. 6.2. The abrupt increase of resistance could be concealed by two effects. One is the previously discussed AMR effect. The other one is the not well-established AP configuration as suggested by the $M(H)$ loop. If the AP state is not well established, the reversing of the *LSMO* magnetization starts taking place when the *Py* magnetization has not saturated yet. As a consequence, the change of resistance is smaller and smoothed.

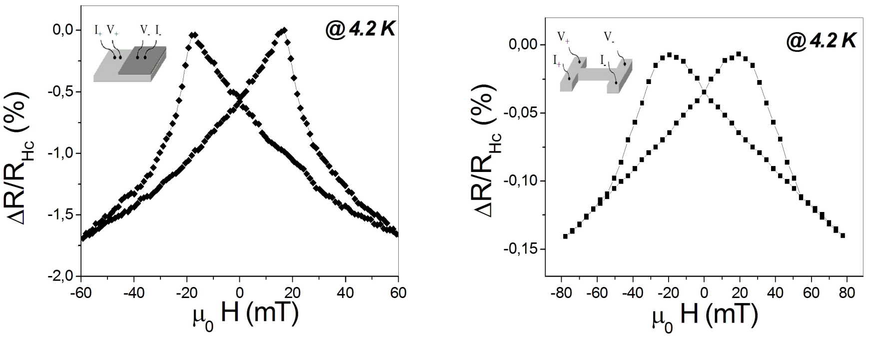

Figure 6.4. Left Panel: *CPP-RH* measured at $T = 4.2K$ with field applied along the *in-plane* [001] easy axis for a bilayer *LSMO* ($30nm$) / *Py* ($10nm$). Right Panel: *CIP-RH* measured at $T = 4.2K$ for a $30nm$ thick, $100\mu m$ wide, and $500\mu m$ long track of *LSMO* with field applied parallel to the current direction. The insets show the measurement configurations [5].

The *AMR* effect is easily suppressed by fabricating planar junctions. Thus, planar junctions were fabricated by processing the bilayer with a two-step lithography process. The bilayer was first patterned by Ar^+ ion milling into tracks $100\mu m$ wide and $500\mu m$ long with the associated connections and contact pads. The areas of the square junctions were defined in correspondence of the tracks by a second photolithographic step and milling of the uncovered *Py*. The etching rate of the layers had been previously calibrated to stop the milling at a few nanometers below the bilayer interface. The final configuration is shown in the inset of Fig. 6.5. The four contact measurement configuration allows the resistance, and hence the *AMR* of the wiring, to be suppressed. The junctions area were fabricated ranging from $30 \times 30\ \mu m^2$ to $100 \times 70\ \mu m^2$.

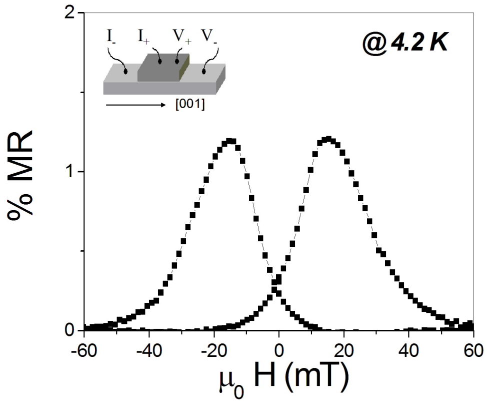

Figure 6.5. *CPP-RH* at $T = 4.2K$ of a junction with an area of $100 \times 70\ \mu m^2$. The magnetic field was applied along the *in-plane* [001] easy axis. The inset shows the measurement configuration. [5]

Fig. 6.5 shows the *CPP-RH* for a $100 \times 70\ \mu m^2$ junction. The shape is typical of a *pseudospin-valve* device with a flat base line. Moreover, increasing H from the negative lowest field value, the resistance does not change smoothly but an abrupt change occurs around the zero field value. This is reflected in a value of resistance at zero field which is much closer to the minimum value compared to the cases of Figs. 6.4(*left*) and 6.4(*right*). The change of resistance between the maximum value and the zero field value, $MR_0 = [R_{max} - R(0mT)]/R(0mT)$, is 0.95% compared to a change of $MR_{max} = 1.2\%$ as referred to the minimum value. The mismatch between MR_0 and MR_{max} is consistent with a not well-established AP state.

It is important to notice that the *CPP* resistance measurements are not affected by problems due to inhomogeneous current distributions that are known to give rise to large apparent *MR* ratios. This effect occurs for junctions with resistances of the electrodes in the junction area comparable to or higher than the junction resistance [131]. In the worst case of the largest junctions, the junction resistance is $R_J = 571\Omega$, whereas the square resistances of the electrodes are $R_{LSMO} = 40\Omega$ and $R_{Py} = 16\Omega$ corresponding to measured resistivities $\rho_{LSMO} \sim 1.2 \times 10^{-6}\Omega m$ and $\rho_{Py} \sim 1.6 \times 10^{-7}\Omega m$ at $4.2K$.

The change of *MR* is much smaller than predicted by Jullière's model previously described in Chap. 2 for tunneling junctions [81]. On the other hand, it has been widely demonstrated that Jullière's model does not apply to ferromagnetic metal/insulator/*LSMO* junctions. Moreover, the amplitude of the *MR* ratio, and even its sign, depends on the choice of the tunnel barrier. De Teresa *et al.* have observed [132] that if the insulating barrier is a lattice matched epitaxial oxide ($SrTiO_3$ or $Ce_{0.69}La_{0.31}O_{1.845}$), the *MR* ratio is negative ($R_{AP} \leq R_P$), whereas it is positive ($R_{AP} \geq R_P$), but much smaller than that predicted by the Jullière's model, when the barrier is a metal oxide. This seems to suggest that in the *LSMO*/*Py* bilayers, if an insulating barrier is present at the interface, it is formed in the metal layer because of oxygen diffusion from the manganite.

The low value of *MR* in these devices can be partially ascribed to a large boundary resistance that masks the effect. In *LSMO*/metal heterostructures, the series of bulk resistances and interface resistances through which the transport is not spin dependent inevitably reduces the measured change of *MR*. When normal metal layers are used as electrodes, the total resistance can be as high as to completely mask the *MR* effect [133]. In the *LSMO*/*Py* devices, the two ferromagnetic layers are themselves the electrodes of the junction. Therefore, only the resistance at the interface between the two ferromagnetic layers plays a role. Yet, this resistance is still rather large. This suggests an insulating nature of the topmost part of the magnetic *dead layer* [136]. The effect of the *dead layer* on the reduction of the *MR* is then twofold. While the metallic part of the *dead layer* works as a spin scattering region, the non-metallic one provides disordered spins at the interface which contribute to the spin depolarization. A reduction of the *dead layer* thickness, and in particular of the non-metallic region of it, could increase the *MR*. This reduction is limited by the necessity of keeping the layers magnetically decoupled.

In conclusion, in this section I reported on the magnetic and transport properties of *LSMO* / *Py* bilayer grown by sputtering on *STO* (110) substrates. The bilayers were used to fabricate devices operating in *CPP* mode. The devices show low field magnetoresistive effect. For the first time the *dead layer* of a manganite was used as an intrinsic spacer [5]. A suitable choice of the *dead layer* thickness should allow the fabrication of devices with high *MR* ratio in which any metal or insulating deposited spacer is needed. I can envisage a possible relevant improvement of the performances in the case of *LSMO* films deposited under optimal conditions for the control of surface properties, i.e. in the M.O.D.A. system.

6.2. Step induced in-plane anisotropy in vicinal LSMO films

Interesting magnetic properties, such as magnetic anisotropy, magnetization reversal mode, magnetic domain structures, or coercive field, can be changed and controlled by surfaces and interfaces when manganites are in the form of thin films. All the above mentioned magnetic properties are linked together. One of the ultimate goal for the design of devices is to be able to engineer them and one simple idea for that is to artificially modify the surface morphology of the ferromagnetic thin films (see Sec. 2.2.2).

Within this framework, in this section I report on the study of the magnetic and magetoresistance properties of *LSMO* films deposited on vicinal *STO* substrate as described in Secs. 3.2.2 and 3.2.2.3.

Longitudinal *Magneto-Optical Kerr Effect (MOKE)* microscopy was used at the *GREYC* lab for the investigation of the magnetic domain arrangement of vicinal *LSMO* films. The *MOKE* setup is described in detail in [134]. The films were patterned by *UV* photolithography and argon ion etching to form $50\mu m$ wide lines and varying lengths ($L = 100$, 150, 200 or 300 μm) depending on the voltage probes used (see the inset of Fig. 6.7).

Magnetic hysteresis loops are calculated by averaging the measured *MOKE* signals over the specified image area. Fig. 6.6 shows such cycles, measured on the $42nm$ thick *LSMO* films with the vicinal angle ranging from 2° to 10°, when H was applied parallel or perpendicular to the step directions. The loop of a $42nm$ thick *LSMO* film deposited on standard (001) *STO* substrate is added for comparison. As expected from simulations made by Zhao *et al.* [135], an easy direction is found when the field is applied along the steps and a hard direction when it is applied across the steps, i.e. the coercive field is maximum when the external field is along the step direction and minimum when the external field is perpendicular to the step direction. In the case of the vicinal 10° *LSMO*, in the easy direction, the coercitive field is $1.16mT$, which is much higher than on (001) *STO*, which is $0.27mT$ in the [110] or [$1\bar{1}0$] directions (Fig. 6.6).

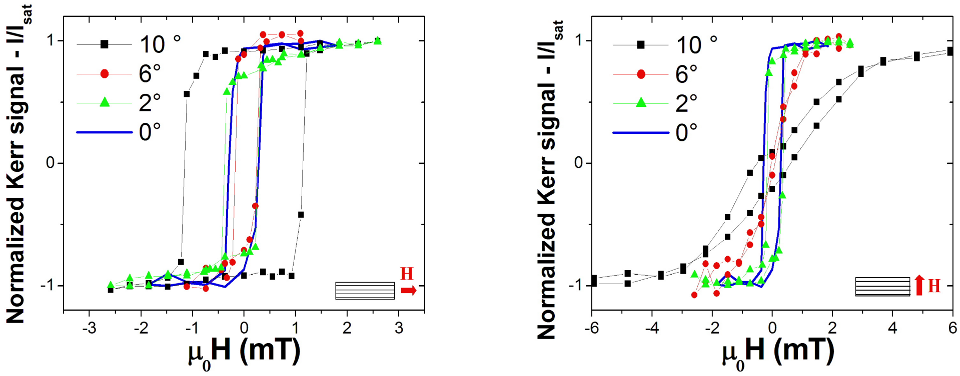

Figure 6.6. *MOKE* hysteresis loops measured at $300K$ on a patterned $42nm$ thick 10° vicinal *LSMO* film, with H applied parallel (*left*) or perpendicular (*right*) to the step directions (H always perpendicular to the patterned line) [100]. The loop of a $42nm$ thick *LSMO* film deposited on standard (001) *STO* substrate is added for comparison.

The *MOKE* hysteresis loops and imaging of the magnetic domains performed at $300K$ on this sample with the magnetic field applied along and across the steps directions are shown in Fig. 6.7. Black and white regions represent magnetic domains with magnetization of opposite direction. The domain arrangement was visualized by subtracting two images. An image was first acquired in an applied field higher than $8mT$, high enough for reaching the saturated state (i.e. with all domains pointing in the same direction), and then subtracted from a second image taken in an applied field lower than the coercive field in the transition region (for which some distribution of the domains is expected). If the magnetic field is applied parallel to the steps we can see magnetic domains with sharp and well defined *DW*s. In that case, the magnetization reversal proceeds by nucleation and propagation of the *DW*s. If the magnetic field is applied perpendicular to the steps, no magnetic domains can be observed and the rotation of the magnetization is coherent. The rotation of the magnetic domains by increasing the external magnetic field, both applied along and across the steps direction, i.e. easy and hard axis respectively, is shown in Fig. 6.7. These qualitative results confirm the different magnetic domain arrangement in vicinal and non-vicinal *LSMO* films as can be expected from the hysteresis loops.

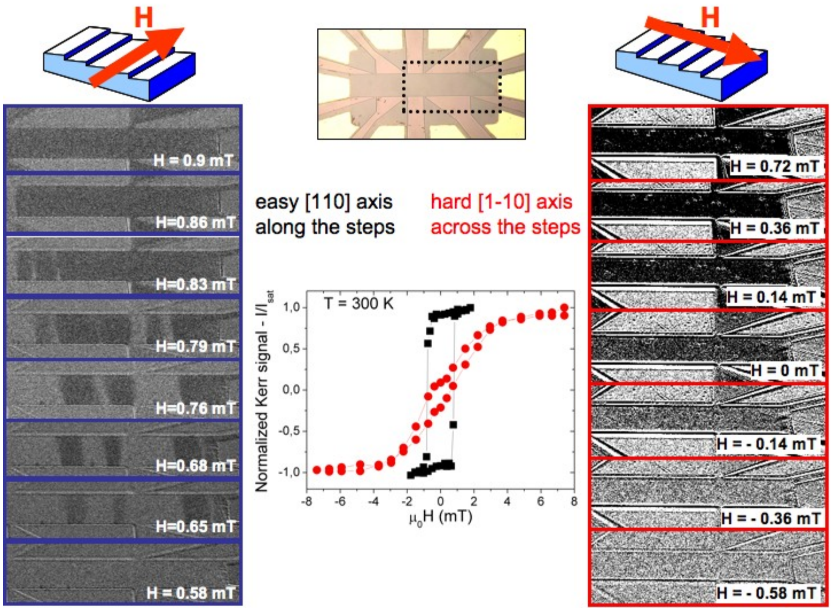

Figure 6.7. *MOKE* $M(H)$ loops and images of magnetic domains in $42nm$ thick films recorded with an applied magnetic field in the plane of the films parallel (easy [110] axis) and perpendicular (hard $[1\bar{1}0]$ axis) to the steps. Black and white regions represent magnetic domains with magnetization of opposite direction [100, 134].

Current-in-plane (*CIP*) magnetoresistance measurements were performed, at room temperature, under an external magnetic field applied parallel and perpendicular to the step edges, in the case of the 10° *LSMO* (Fig. 6.8). As expected, the steps, induced by the vicinality of the substrates, determine consistent *in-plane* anisotropy. Thus, when the current (I) flows trough the *LSMO* film along the $[1\bar{1}0]$ crystallographic direction, that is perpendicular to the steps, the *MR* effect is maximized.

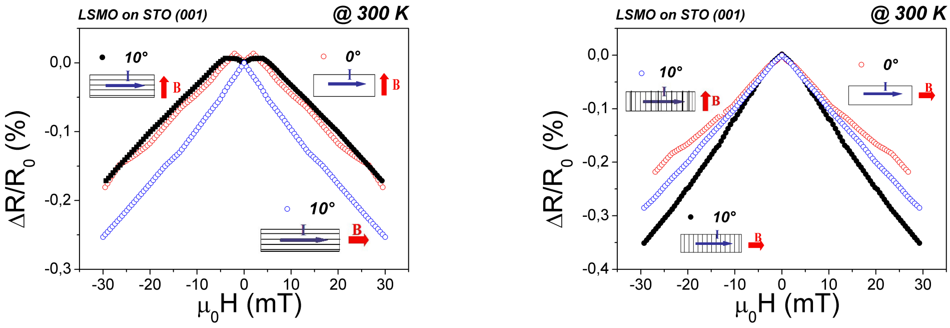

Figure 6.8. *CIP* magnetoresistance vs. external magnetic field (B) applied parallel and perpedicular to the steps of the $42nm$ thick *LSMO* film deposited onto (001) *STO* 10° tw $(1\bar{1}0)$. The current (I) is perpendicular to B *(left)* and parallel to B *(right)*. The case of non-vicinal *LSMO* film deposited onto standard (001) *STO* is also shown (red opened circle in figure). The measurements were performed at $300K$.

Depending on the direction of the magnetic field ($\vec{B} = \mu_0\vec{H}$), the *MR* changes. If the current (I) is parallel to the step edges the *MR* replies the behaviour of the non-vicinal *LSMO*, added for comparison in Fig. 6.8*(left)*. In such a case, the *MR* effect is less than

0.2%. If $I \parallel B$ and $\perp$ *steps*, the maximum MR is 0.37%. This enhancement of the MR is attributed to the DWs (Fig. 6.8*(right)*).

6.3. Double domain wall LSMO device

In this section, I report on the fabrication and characterization of a $LSMO$ device, based on the *domain walls* (DWs) between regions with different orientation of magnetization [137] (see Sec. 2.2.2). $LSMO$ films grown onto (110) STO single crystal substrates were fabricated by a *RF magnetron sputtering* technique using the deposition condition described in Chap. 3.

The films were then patterned into $5\mu m$ wide, $100\mu m$ long tracks parallel to the [001] easy magnetization axis (Fig. 6.9a) by standard UV lithography and Ar^+ ion milling. Any track is provided with connections and contact pads for standard four-points measurements. The samples were then processed in a dual-beam FIB/SEM with Ga^+ ion source. The tracks were narrowed down to $500nm$ with a beam current of $10pA$ to achieve $3\mu m$ long nano-bridges (Fig. 6.9b). The aspect ratio ($3\mu m \times 500nm$) of the narrowed bridges was chosen to enable pinning effect by shape anisotropy after the patterning of two symmetric constrictions at the bridge borders (Fig. 6.9c). The scanning electron microscope (SEM) images of the constrictions (Fig. 6.9d) indicate that, by using a beam current of $1pA$ (corresponding to a spot size of $7nm$), the rounding off due to the Gaussian profile of the FIB beam can be confined within a few nm for films with thickness up to $100nm$. Thus, two $LSMO$-based devices were fabricated performing constrictions of $30nm$ and $50nm$ wide.

In the following report of sample characterization, the external magnetic field is intended to be always applied parallel to the tracks, and therefore along the *easy* axis of magnetization.

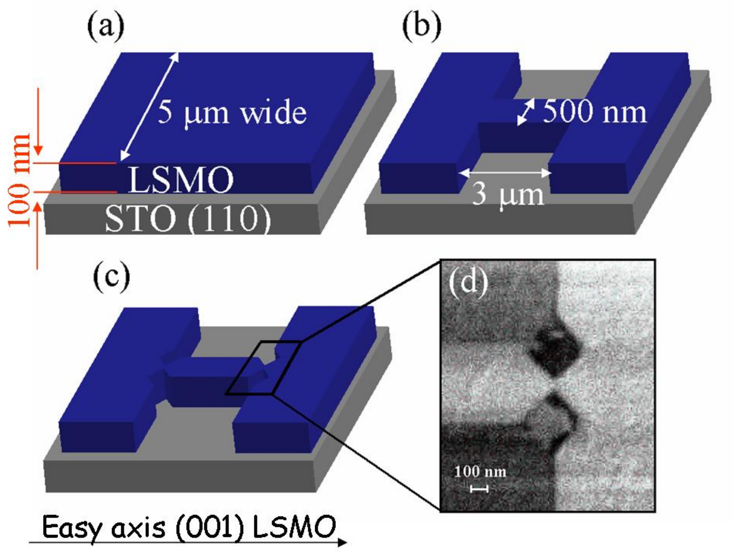

Figure 6.9. Schematic of the fabrication process: *(a)* Ar^+ ion milling of $5\mu m$ wide tracks; *(b)* *FIB* milling of $3\mu m$ long, $500nm$ wide bridges; *(c)* *FIB* milling of nanoconstrictions at the bridge borders; *(d)* *SEM* image of a patterned nanoconstriction [137].

Devices with $30nm$ wide constrictions showed a strong *non-linearity* of the *current-voltage* ($I-V$) characteristic in a wide range of temperatures (Fig. 6.10). The $I-V$ curves are well fitted by the Fowler-Nordheim equation [138] suggesting an electron tunnelling in such nanoconstrictions. In fact, the devices show tunnel barrier behaviour and a bias voltage higher than the barrier height has to be applied to enable current flow. The height ψ and width ω of this barrier can be determined by fitting the $I-Vs$ with the Fowler-Nordheim model [138]:

$$J = \frac{e^3}{8\pi h}\frac{1}{\psi}\left(\frac{V}{2\omega}\right)^2 exp\left(-\frac{8\pi\sqrt{2m}}{3eh}\frac{2\omega}{V}\psi^{3/2}\right) \tag{6.1}$$

where J is the current density, e is the electron charge, h is the Planck's constant and m is the free electron mass. The experimental data are fitted very well by Eq. 6.1 with the best fitting parameters as reported in the inset of Fig. 6.10. Moreover, the MR decreases with voltage, that is typical of TMR devices.

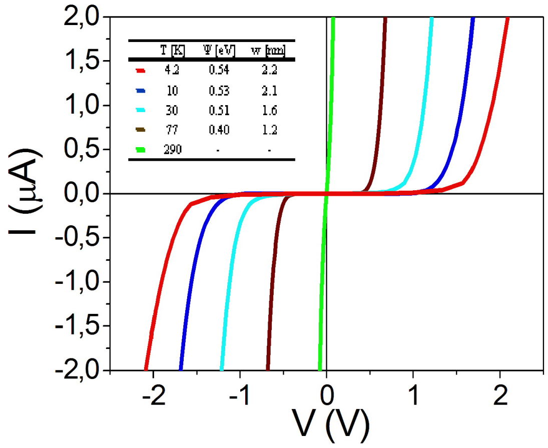

	T [K]	Ψ [eV]	w [nm]
🟥	4.2	0.54	2.2
🟦	10	0.53	2.1
🟦	30	0.51	1.6
🟫	77	0.40	1.2
🟩	290	-	-

Figure 6.10. $I-V$ characteristics measured on a device with $30nm$ wide constrictions in the low resistance state at different temperatures. Upper left inset reports the fitting parameters by Eq. 6.1 [137].

The behaviour of the wider constrictions ($50nm$) is different because the $I-V$ characteristics are *linear* and the MR is lower. The plot of magnetoresistance shows that for this device the depinning of the domain walls at the two nanoconstrictions is not simultaneous (Fig. 6.11). Moreover the hysteresis loop is not symmetric. This means that the direction of the current has influence on the pinning and depinning mechanisms, as also the current intensity does. This is not a classical behaviour, and it is a plausible manifestation of a spin torque acting on the domain walls because of spin injection. Finally, in such device, the current is able to switch the state of the device without the application of an external magnetic field (at $H = 0$, current density $J = 1.6 \times 10^{11} A/m$).

In conclusion, in this section it is experimentally demonstrated that spin valves based on DW resistivity can be switched by the application of either a magnetic field or an electrical current. The DW depinning threshold depends on the transverse anisotropy constant of the region toward which the DW is displaced. This suggests that, for transverse walls, the current threshold for DW motion can be simply controlled by changing the lateral track width on submicron scale. If the electrodes have significantly different magnetic anisotropies, the DW can be compressed by either an external field or a polarized current, resulting in an enhanced DW resistance. This possibility could be exploited for magnetic field sensors.

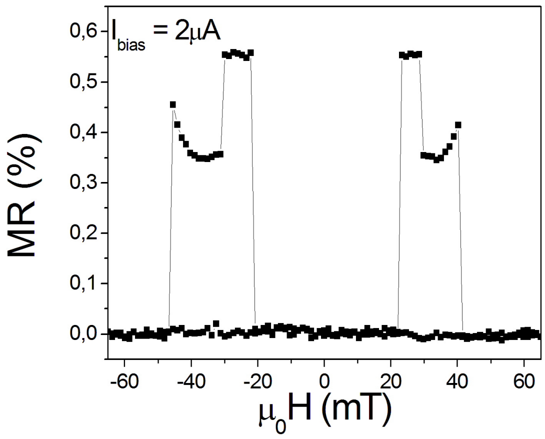

Figure 6.11. Change of R (normalized at the smallest resistance value) due to current-induced DW displacement for a device with $50nm$ wide constrictions after trapping DWs at the constrictions ($T = 4.2K$). [137].

Conclusions

The aim of this thesis was to demonstrate that the perovskitic manganite $La_{0.7}Sr_{0.3}MnO_3$ is an interesting candidate for the design and development of devices, with particular reference to room temperature bolometers and spintronics devices.

To develop this idea, it was first necessary to achieve the full control of the growth of epitaxial $La_{0.7}Sr_{0.3}MnO_3$ films. I employed three different deposition techniques (sputtering, *PLD* and *RHEED* assisted *PLD*), producing and characterizing a very large set of samples. I demonstrated that each technique can be successfully employed to get high quality samples, being the final results related to the level of control and of complexity of the considered process.

Since the physical properties of $La_{0.7}Sr_{0.3}MnO_3$ films are strongly dependent on the structure and microstructure, I characterized the samples by x ray diffraction, with particular attention devoted to the investigation of epitaxy and strain, and (in one case) by high resolution *TEM*. In view of the relevance of $La_{0.7}Sr_{0.3}MnO_3$ films surface for various applications and for the development of multilayer structure, *RHEED*, *LEED*, and *STM / AFM* analyses were also performed.

I investigated the transport and magnetic properties by $\rho(T)$, $M(T)$ and $M - H$ measurements performed in magnetometers or resorting to *MOKE*. The disposability of samples grown with different techniques gave in this case the unique opportunity to propose the interpretation of the data in terms of intrinsic material properties.

I faced the key problem of film growth on Si substrates by developing and comparing two different, complex multilayer structures, with the aim of demonstrating the feasibility of $La_{0.7}Sr_{0.3}MnO_3$ films with properties that are suited to the realization of room temperature bolometers, as demonstrated by the values of the relevant figures of merit. The results are in this respect very promising, indicating that the field is mature for the design and development of the first prototypes.

Finally, the successful design and realization of two different spintronics devices, based on concepts as the dead layer and the spin injection, demonstrated that the potentiality of $La_{0.7}Sr_{0.3}MnO_3$ in this fascinating field is mainly related to the capability to take advantage of its peculiar physical properties. The operating temperature still seems an issue, though. However, the experience of sample production under extremely high controlled conditions, achieved in M.O.D.A., indicates that the ultimate limit of performances is strictly bound to the quality of the bulk and of the surface of samples, demanding for a high technological environment for fabrication.

Acknowledgements

First, I would like to thank my academic supervisors, Prof. Umberto Scotti di Uccio, from the University of Cassino, who is an excellent teacher and friend, and Dr. Laurence Méchin, from the GREYC laboratory in Caen, who is a brilliant researcher and always helped me during my french stages. Without their guidance and perceptive discussions, I would have never finished my PhD study.

Thanks to Prof. G. Mascolo, Dr. C. Pagliuca and all of the researchers, technicians and students of the LAM lab of the University of Cassino, and to the coordinator, the director and the collegues of my PhD course. In particular, thanks to Stefania F. who helped me in many bureaucratic troubles.

I greatly appreciated all the professors, researchers, students and secretary staff of the GREYC lab in Caen who kindly received me and helped me for all I needed. From the first moment they put me in a friendly environment. In particular, I would like to thank the professors Stefan Flament, Silvana Mercone, Jean Marc Routure, Bruno Guillet, Chantal Gunther, and the PhD Mohammed Saib and Carlo Barone.

I due special thanks to the CNR-INFM Coherentia professors, researchers and PhD students of the MODA laboratory in Naples, Fabio Miletto, Milan Radovic, Alessia Sambri, Nathascia Lampis, Marco Salluzzo, Roberto di Capua, Gabriella de Luca, Antonio Ruotolo, Gianpiero Pepe, Gianrico Lamura, and the director Ruggero Vaglio. The work concerning the Coherentia activities that I am presenting here would not be possible without their excellent work and their great experience.

I would like to thank my whole family, that supports me in spirit and mind. I wish to name also my *new* beautiful niece Nadia.

Special thanks to Davide and Antonio, for their never-forgettable support.

Finally, I will never forget the endless support by Viola who has been encouraging me since the beginning of this three-years PhD. She shared with me the life experience in Normandy and she is largely determining my happiness.

Paolo

Appendix

This Appendix contains the detailed structural data as determined by x ray diffraction performed on *LSMO* films grown onto (001)- and (110)-oriented *STO* single crystal substrates (reported in Chap. 3), *YSZ*-buffered silicon (reported in Chap. 4) and *STO* vicinal substrates (reported in Chap. 6.2).

Structure of LSMO grown on STO substrates

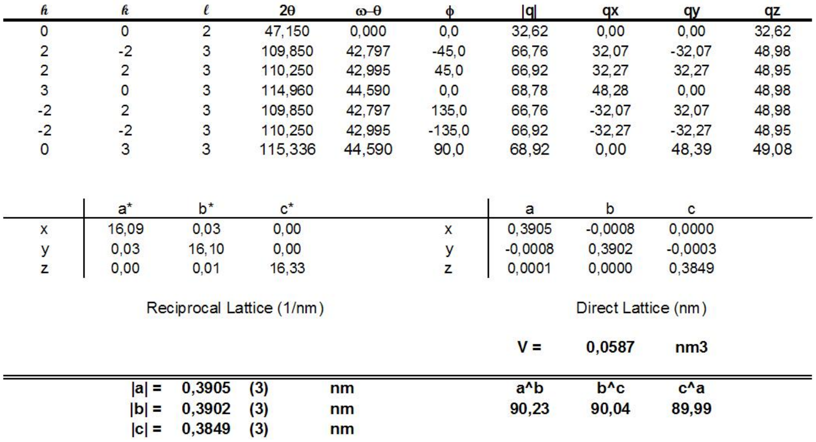

ℎ	𝓀	ℓ	2θ	ω-θ	ϕ	|q|	qx	qy	qz
0	0	2	47,150	0,000	0,0	32,62	0,00	0,00	32,62
2	-2	3	109,850	42,797	-45,0	66,76	32,07	-32,07	48,98
2	2	3	110,250	42,995	45,0	66,92	32,27	32,27	48,95
3	0	3	114,960	44,590	0,0	68,78	48,28	0,00	48,98
-2	2	3	109,850	42,797	135,0	66,76	-32,07	32,07	48,98
-2	-2	3	110,250	42,995	-135,0	66,92	-32,27	-32,27	48,95
0	3	3	115,336	44,590	90,0	68,92	0,00	48,39	49,08

	a*	b*	c*		a	b	c
x	16,09	0,03	0,00	x	0,3905	-0,0008	0,0000
y	0,03	16,10	0,00	y	-0,0008	0,3902	-0,0003
z	0,00	0,01	16,33	z	0,0001	0,0000	0,3849

Reciprocal Lattice (1/nm) Direct Lattice (nm)

V = 0,0587 nm3

|a| =	**0,3905**	**(3)**	**nm**	**a^b**	**b^c**	**c^a**
|b| =	**0,3902**	**(3)**	**nm**	**90,23**	**90,04**	**89,99**
|c| =	**0,3849**	**(3)**	**nm**			

Table 6.1. Data (experimental angles and reciprocal space vectors) and least squares fit results for 32nm thick *LSMO* on (001) *STO*, where c is *out-of-plane* and a, b are the *in-plane* lattice parameters. Figures in round brackets are errors from the fit procedure.

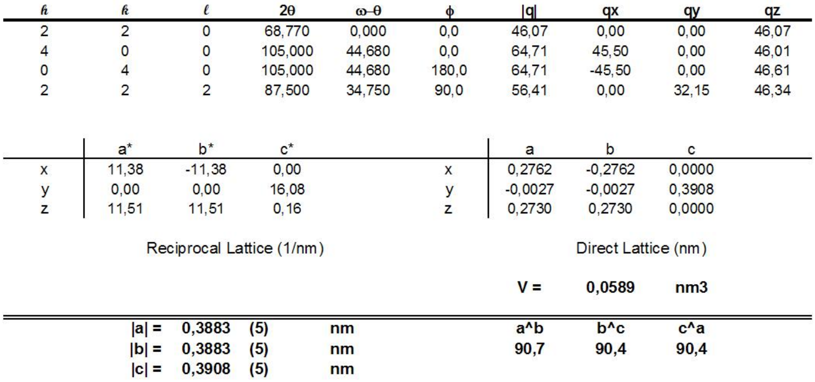

ℎ	𝓀	ℓ	2θ	ω-θ	ϕ	|q|	qx	qy	qz
2	2	0	68,770	0,000	0,0	46,07	0,00	0,00	46,07
4	0	0	105,000	44,680	0,0	64,71	45,50	0,00	46,01
0	4	0	105,000	44,680	180,0	64,71	-45,50	0,00	46,61
2	2	2	87,500	34,750	90,0	56,41	0,00	32,15	46,34

	a*	b*	c*		a	b	c
x	11,38	-11,38	0,00	x	0,2762	-0,2762	0,0000
y	0,00	0,00	16,08	y	-0,0027	-0,0027	0,3908
z	11,51	11,51	0,16	z	0,2730	0,2730	0,0000

Reciprocal Lattice (1/nm) Direct Lattice (nm)

V = 0,0589 nm3

|a| =	**0,3883**	**(5)**	**nm**	**a^b**	**b^c**	**c^a**
|b| =	**0,3883**	**(5)**	**nm**	**90,7**	**90,4**	**90,4**
|c| =	**0,3908**	**(5)**	**nm**			

Table 6.2. Data (experimental angles and reciprocal space vectors) and least squares fit results for 51nm thick *LSMO* on (110) *STO*, where a, b, c are the lattice parameters. Figures in round brackets are errors from the fit procedure.

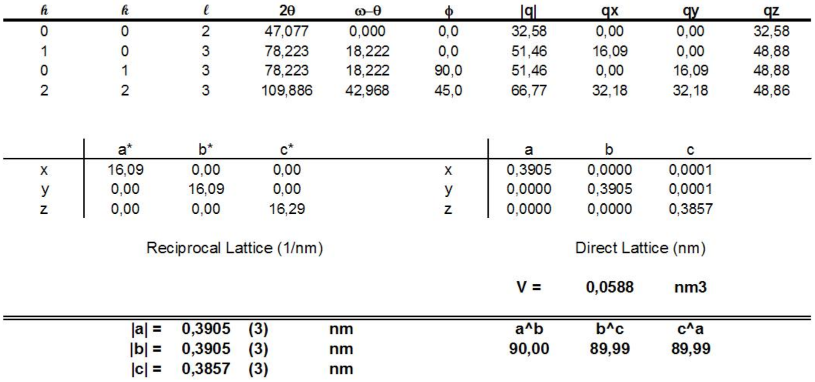

h	k	ℓ	2θ	ω–θ	φ	$\lvert q\rvert$	qx	qy	qz
0	0	2	47,077	0,000	0,0	32,58	0,00	0,00	32,58
1	0	3	78,223	18,222	0,0	51,46	16,09	0,00	48,88
0	1	3	78,223	18,222	90,0	51,46	0,00	16,09	48,88
2	2	3	109,886	42,968	45,0	66,77	32,18	32,18	48,86

	a*	b*	c*		a	b	c
x	16,09	0,00	0,00	x	0,3905	0,0000	0,0001
y	0,00	16,09	0,00	y	0,0000	0,3905	0,0001
z	0,00	0,00	16,29	z	0,0000	0,0000	0,3857

Reciprocal Lattice (1/nm) Direct Lattice (nm)

V = 0,0588 nm3

|a| = 0,3905 (3) nm
|b| = 0,3905 (3) nm
|c| = 0,3857 (3) nm

a^b	b^c	c^a
90,00	89,99	89,99

Table 6.3. Data (experimental angles and reciprocal space vectors) and least squares fit results for 75nm thick *LSMO* on (001) *STO*, where c is *out-of-plane* and a, b are the *in-plane* lattice parameters. Figures in round brackets are errors from the fit procedure.

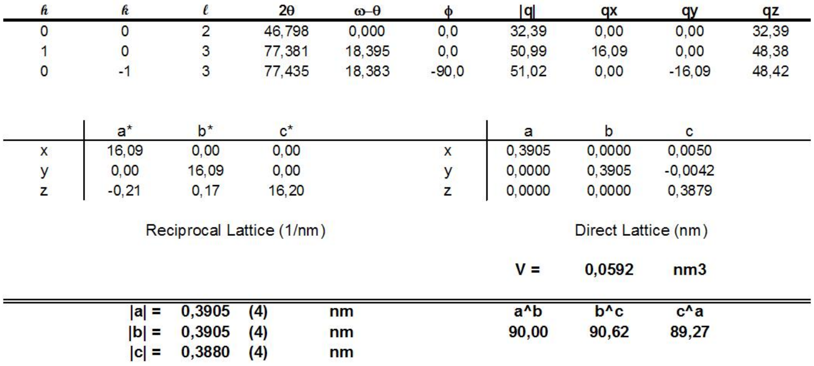

h	k	ℓ	2θ	ω–θ	φ	$\lvert q\rvert$	qx	qy	qz
0	0	2	46,798	0,000	0,0	32,39	0,00	0,00	32,39
1	0	3	77,381	18,395	0,0	50,99	16,09	0,00	48,38
0	-1	3	77,435	18,383	-90,0	51,02	0,00	-16,09	48,42

	a*	b*	c*		a	b	c
x	16,09	0,00	0,00	x	0,3905	0,0000	0,0050
y	0,00	16,09	0,00	y	0,0000	0,3905	-0,0042
z	-0,21	0,17	16,20	z	0,0000	0,0000	0,3879

Reciprocal Lattice (1/nm) Direct Lattice (nm)

V = 0,0592 nm3

|a| = 0,3905 (4) nm
|b| = 0,3905 (4) nm
|c| = 0,3880 (4) nm

a^b	b^c	c^a
90,00	90,62	89,27

Table 6.4. Data (experimental angles and reciprocal space vectors) and least squares fit results for *LSMO* (13nm thick) on (001) *STO*, where c is *out-of-plane* and a, b are the *in-plane* lattice parameters. Figures in round brackets are errors from the fit procedure.

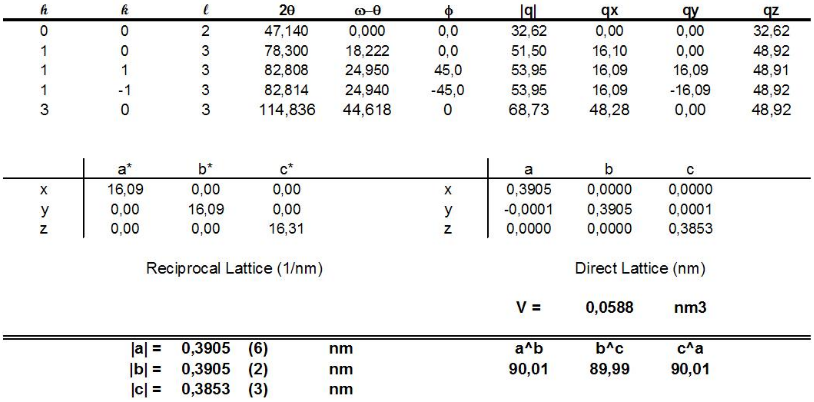

h	k	ℓ	2θ	ω–θ	φ	$\lvert q\rvert$	qx	qy	qz
0	0	2	47,140	0,000	0,0	32,62	0,00	0,00	32,62
1	0	3	78,300	18,222	0,0	51,50	16,10	0,00	48,92
1	1	3	82,808	24,950	45,0	53,95	16,09	16,09	48,91
1	-1	3	82,814	24,940	-45,0	53,95	16,09	-16,09	48,92
3	0	3	114,836	44,618	0	68,73	48,28	0,00	48,92

	a*	b*	c*		a	b	c
x	16,09	0,00	0,00	x	0,3905	0,0000	0,0000
y	0,00	16,09	0,00	y	-0,0001	0,3905	0,0001
z	0,00	0,00	16,31	z	0,0000	0,0000	0,3853

Reciprocal Lattice (1/nm) Direct Lattice (nm)

V = 0,0588 nm3

|a| = 0,3905 (6) nm
|b| = 0,3905 (2) nm
|c| = 0,3853 (3) nm

a^b	b^c	c^a
90,01	89,99	90,01

Table 6.5. Data (experimental angles and reciprocal space vectors) and least squares fit results for *LSMO* (45nm thick) on (001) *STO*, where c is *out-of-plane* and a, b are the *in-plane* lattice parameters. Figures in round brackets are errors from the fit procedure.

Structure of LSMO grown on vicinal STO substrate

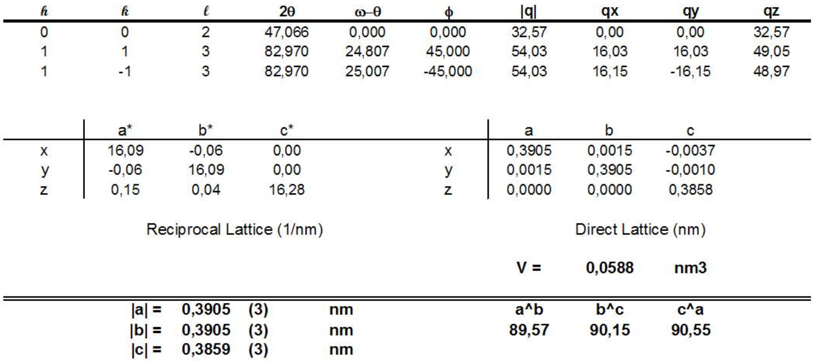

h	k	ℓ	2θ	ω–θ	φ	|q|	qx	qy	qz
0	0	2	47,066	0,000	0,000	32,57	0,00	0,00	32,57
1	1	3	82,970	24,807	45,000	54,03	16,03	16,03	49,05
1	-1	3	82,970	25,007	-45,000	54,03	16,15	-16,15	48,97

	a*	b*	c*			a	b	c
x	16,09	-0,06	0,00		x	0,3905	0,0015	-0,0037
y	-0,06	16,09	0,00		y	0,0015	0,3905	-0,0010
z	0,15	0,04	16,28		z	0,0000	0,0000	0,3858
	Reciprocal Lattice (1/nm)					Direct Lattice (nm)		
						V =	**0,0588**	**nm3**

|a| =	**0,3905**	**(3)**	**nm**	**a^b**	**b^c**	**c^a**
|b| =	**0,3905**	**(3)**	**nm**	**89,57**	**90,15**	**90,55**
|c| =	**0,3859**	**(3)**	**nm**			

Table 6.6. Data (experimental angles and reciprocal space vectors) and least squares fit results for 10° vicinal *LSMO* 42*nm* thick, where *c* is *out-of-plane* and *a*, *b* are the *in-plane* lattice parameters. Figures in round brackets are errors from the fit procedure.

Structure of buffered Si multilayers

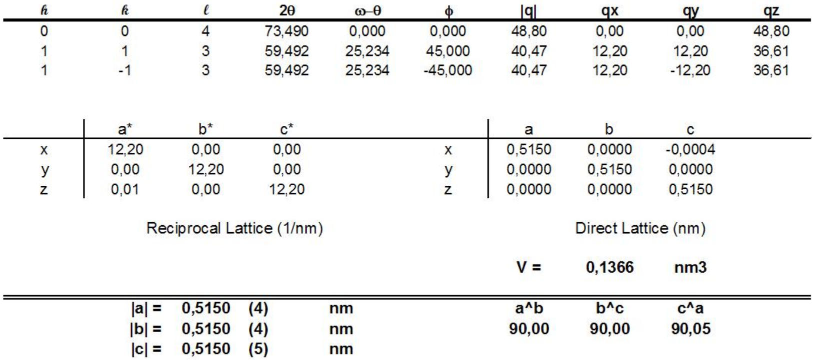

h	k	ℓ	2θ	ω–θ	φ	|q|	qx	qy	qz
0	0	4	73,490	0,000	0,000	48,80	0,00	0,00	48,80
1	1	3	59,492	25,234	45,000	40,47	12,20	12,20	36,61
1	-1	3	59,492	25,234	-45,000	40,47	12,20	-12,20	36,61

	a*	b*	c*			a	b	c
x	12,20	0,00	0,00		x	0,5150	0,0000	-0,0004
y	0,00	12,20	0,00		y	0,0000	0,5150	0,0000
z	0,01	0,00	12,20		z	0,0000	0,0000	0,5150
	Reciprocal Lattice (1/nm)					Direct Lattice (nm)		
						V =	**0,1366**	**nm3**

|a| =	**0,5150**	**(4)**	**nm**	**a^b**	**b^c**	**c^a**
|b| =	**0,5150**	**(4)**	**nm**	**90,00**	**90,00**	**90,05**
|c| =	**0,5150**	**(5)**	**nm**			

Table 6.7. Data (experimental angles and reciprocal space vectors) and least squares fit results for the *YSZ* layer (130*nm* thick), where *c* is out-of-plane and *a*, *b* are the *in-plane* lattice parameters. Figures in round brackets are errors from the fit procedure.

h	k	ℓ	2θ	$\omega-\theta$	ϕ	|q|	qx	qy	qz
0	0	16	44,345	0,000	0,000	30,78	0,00	0,00	30,78
1	1	21	64,509	22,258	45,000	43,53	11,66	11,66	40,29
1	-1	21	64,509	22,258	-45,000	43,53	11,66	-11,66	40,29

	a*	b*	c*		a	b	c
x	11,66	0,00	0,00	x	0,5389	0,0000	0,0323
y	0,00	11,66	0,00	y	0,0000	0,5389	0,0000
z	-0,12	0,00	1,92	z	0,0000	0,0000	3,2657

Reciprocal Lattice (1/nm) Direct Lattice (nm)

V = 0,9485 nm3

				a^b	b^c	c^a
|a| =	**0,5389**	**(4)**	**nm**	**90,00**	**90,00**	**89,43**
|b| =	**0,5389**	**(3)**	**nm**			
|c| =	**3,2659**	**(5)**	**nm**			

Table 6.8. Data (experimental angles and reciprocal space vectors) and least squares fit results for the *BTO* layer (20*nm* thick) of the *BTO-based LSMO* film, where *c* is *out-of-plane* and *a*, *b* are the *in-plane* lattice parameters. Figures in round brackets are errors from the fit procedure.

h	k	ℓ	2θ	$\omega-\theta$	ϕ	|q|	qx	qy	qz
0	0	2	47,118	0,000	0,000	32,60	0,00	0,00	32,60
3	0	3	116,112	45,290	0,000	69,22	49,19	0,00	48,69
0	3	3	116,112	45,200	90,000	69,22	0,00	49,11	48,77
1	0	3	77,690	18,575	0,000	51,16	16,30	0,00	48,50
-1	0	3	77,690	18,575	180,000	51,16	-16,30	0,00	48,50

	a*	b*	c*		a	b	c
x	16,37	-0,01	0,01	x	0,3838	0,0000	-0,0008
y	0,00	16,37	0,00	y	0,0002	0,3838	-0,0015
z	0,03	0,06	16,19	z	-0,0002	0,0000	0,3880

Reciprocal Lattice (1/nm) Direct Lattice (nm)

V = 0,0571 nm3

				a^b	b^c	c^a
|a| =	**0,3838**	**(4)**	**nm**	**89,98**	**90,23**	**90,14**
|b| =	**0,3838**	**(3)**	**nm**			
|c| =	**0,3880**	**(5)**	**nm**			

Table 6.9. Data (experimental angles and reciprocal space vectors) and least squares fit results for the *LSMO* film 50*nm* thick deposited on *BTO-based* multilayer, where *c* is *out-of-plane* and *a*, *b* are the *in-plane* lattice parameters. Figures in round brackets are errors from the fit procedure.

h	k	ℓ	2θ	$\omega-\theta$	ϕ	|q|	qx	qy	qz
0	0	2	46,622	0,000	0,000	32,28	0,00	0,00	32,28
3	0	3	115,400	45,030	0,000	68,95	48,78	0,00	48,73
0	3	3	115,400	45,030	90,000	68,95	0,00	48,78	48,73

	a*	b*	c*		a	b	c
x	16,26	0,00	0,00	x	0,3864	0,0000	-0,0025
y	0,00	16,26	0,00	y	0,0000	0,3864	-0,0025
z	0,10	0,10	16,14	z	0,0000	0,0000	0,3893

Reciprocal Lattice (1/nm) Direct Lattice (nm)

V = 0,0581 nm3

				a^b	b^c	c^a
|a| =	**0,3864**	**(4)**	**nm**	**90,00**	**90,36**	**90,36**
|b| =	**0,3864**	**(4)**	**nm**			
|c| =	**0,3893**	**(5)**	**nm**			

Table 6.10. Data (experimental angles and reciprocal space vectors) and least squares fit results for the *LSMO* film 25*nm* thick deposited on *BTO-based* multilayer, where *c* is *out-of-plane* and *a*, *b* are the *in-plane* lattice parameters. Figures in round brackets are errors from the fit procedure.

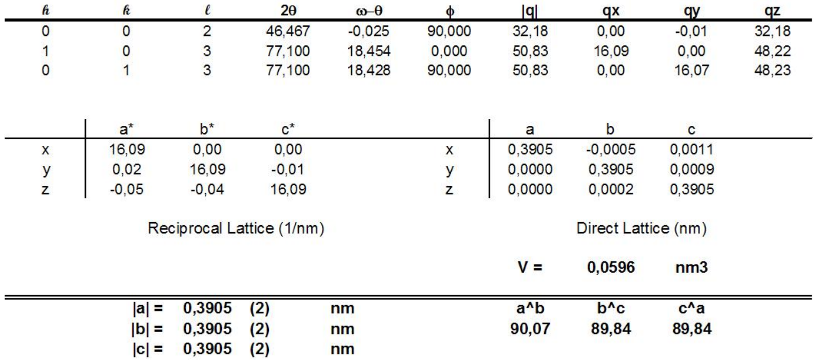

h	k	ℓ	2θ	ω–θ	ϕ	|q|	qx	qy	qz
0	0	2	46,467	-0,025	90,000	32,18	0,00	-0,01	32,18
1	0	3	77,100	18,454	0,000	50,83	16,09	0,00	48,22
0	1	3	77,100	18,428	90,000	50,83	0,00	16,07	48,23

	a*	b*	c*
x	16,09	0,00	0,00
y	0,02	16,09	-0,01
z	-0,05	-0,04	16,09

Reciprocal Lattice (1/nm)

	a	b	c
x	0,3905	-0,0005	0,0011
y	0,0000	0,3905	0,0009
z	0,0000	0,0002	0,3905

Direct Lattice (nm)

V = 0,0596 nm3

|a| = 0,3905 (2) nm
|b| = 0,3905 (2) nm
|c| = 0,3905 (2) nm

a^b	**b^c**	**c^a**
90,07	**89,84**	**89,84**

Table 6.11. Data (experimental angles and reciprocal space vectors) and least squares fit results for the *STO* under top layer (50*nm* thick) of the *STO-based LSMO* film 50*nm* thick, where *c* is *out-of-plane* and *a*, *b* are the *in-plane* lattice parameters. Figures in round brackets are errors from the fit procedure.

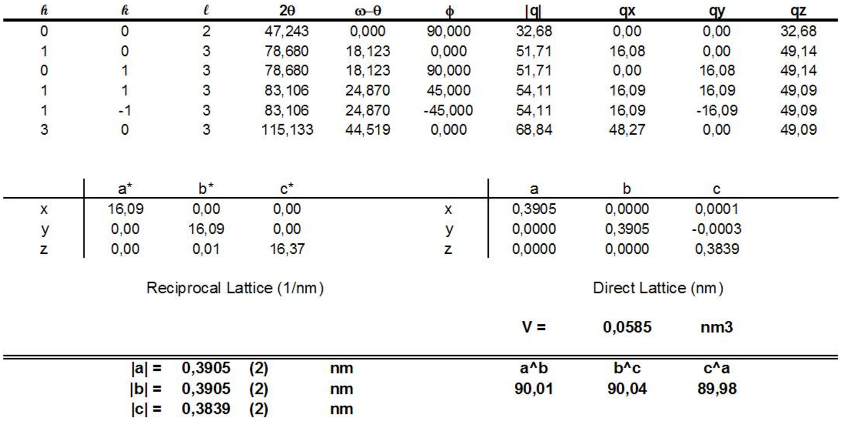

h	k	ℓ	2θ	ω–θ	ϕ	|q|	qx	qy	qz
0	0	2	47,243	0,000	90,000	32,68	0,00	0,00	32,68
1	0	3	78,680	18,123	0,000	51,71	16,08	0,00	49,14
0	1	3	78,680	18,123	90,000	51,71	0,00	16,08	49,14
1	1	3	83,106	24,870	45,000	54,11	16,09	16,09	49,09
1	-1	3	83,106	24,870	-45,000	54,11	16,09	-16,09	49,09
3	0	3	115,133	44,519	0,000	68,84	48,27	0,00	49,09

	a*	b*	c*
x	16,09	0,00	0,00
y	0,00	16,09	0,00
z	0,00	0,01	16,37

Reciprocal Lattice (1/nm)

	a	b	c
x	0,3905	0,0000	0,0001
y	0,0000	0,3905	-0,0003
z	0,0000	0,0000	0,3839

Direct Lattice (nm)

V = 0,0585 nm3

|a| = 0,3905 (2) nm
|b| = 0,3905 (2) nm
|c| = 0,3839 (2) nm

a^b	**b^c**	**c^a**
90,01	**90,04**	**89,98**

Table 6.12. Data (experimental angles and reciprocal space vectors) and least squares fit results for the *LSMO* film 50*nm* thick deposited on *STO-based* multilayer, where *c* is *out-of-plane* and *a*, *b* are the *in-plane* lattice parameters. Figures in round brackets are errors from the fit procedure.

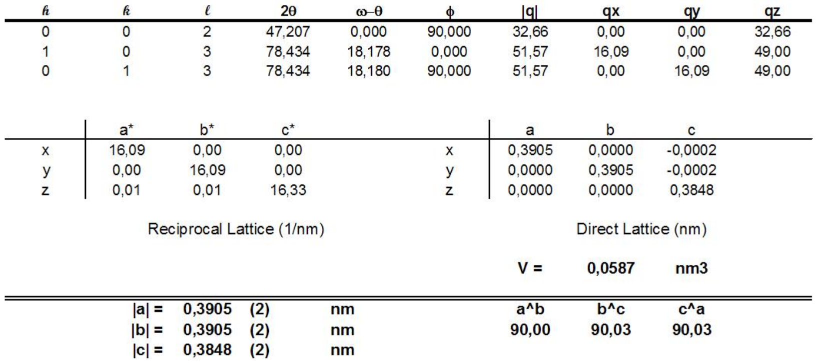

h	k	ℓ	2θ	ω–θ	ϕ	|q|	qx	qy	qz
0	0	2	47,207	0,000	90,000	32,66	0,00	0,00	32,66
1	0	3	78,434	18,178	0,000	51,57	16,09	0,00	49,00
0	1	3	78,434	18,180	90,000	51,57	0,00	16,09	49,00

	a*	b*	c*
x	16,09	0,00	0,00
y	0,00	16,09	0,00
z	0,01	0,01	16,33

Reciprocal Lattice (1/nm)

	a	b	c
x	0,3905	0,0000	-0,0002
y	0,0000	0,3905	-0,0002
z	0,0000	0,0000	0,3848

Direct Lattice (nm)

V = 0,0587 nm3

|a| = 0,3905 (2) nm
|b| = 0,3905 (2) nm
|c| = 0,3848 (2) nm

a^b	**b^c**	**c^a**
90,00	**90,03**	**90,03**

Table 6.13. Data (experimental angles and reciprocal space vectors) and least squares fit results for the *LSMO* film 32*nm* thick deposited on *STO-based* multilayer, where *c* is *out-of-plane* and *a*, *b* are the *in-plane* lattice parameters. Figures in round brackets are errors from the fit procedure.

List of Figures

List of Tables

Bibliography

[1] M. N. Baibich, J. M. Broto, A. Fert, F. Nguyen Van Dau, P. Etienne, G. Creuzet, A. Friederich and J. Chazelas, *Phys. Rev. Lett.* 61, 2472 (1988)

[2] S. Jin, T. H. Tiefel, M. Mc Cormack, R. A. Fastnacht, R. Ramesh and L. H. Chen, *Science* 264, 413 (1994)

[3] G. A. Prinz, *Science* 282, 1660 (1998)

[4] L. Méchin, J.M. Routoure, B. Guillet, F. Yang, S. Flament, D. Robbes, R.A. Chakalov, *Appl. Phys. Lett.* 87, 204103 (2005)

[5] A. Ruotolo, A. Oropallo, F. Miletto Granozio, P. Perna and U. Scotti di Uccio, *Appl. Phys. Lett.* 88, 252504 (2006)

[6] S. A. Wolf, D. D. Awschalom, R. A. Buhrman, J. M. Daughton, S. von Molnar, M. L. Roukes, A. Y. Chtchelkanova, D. M. Treger, *Science* 294, 1488 (2007)

[7] G. H. Jonker and J. H. Van Santen, *Physica* 16, 337 (1950); J. H. Van Santen and G. H. Jonker, Physica 16, 599 (1950); G. H. Jonker, *Physica* 20, 1118 (1954)

[8] H. Y. Hwang, S.-W. Cheong, P. G. Radaelli, M. Marezio, and B. Batlogg, *Phys. Rev. Lett.* 75(5), 914 (1995)

[9] Q. Huang, A. Santoro, J. W. Lynn, R. W. Erwin, J. A. Borchers, J. L. Peng and R. L. Greene, *Phys. Rev. B* 55, 14987 (1997)

[10] J. Rodriguez-Carvajal, M. Hennion, F. Moussa, A. H. Moudden, L. Pinsard and A. Revcolevschi, *Phys. Rev. B* 57, R3189 (1998)

[11] A-M. Haghiri-Gosnet and J-P. Renard, *J. Phys. D: Appl. Phys.* 36, R127-R150 (2003)

[12] H. Hazama, T. Goto, Y. Remoto, Y. Tapioca, A. Asamitsu, and Y. Tokura, *Phys. Rev. B* 62, 15012, (2000)

[13] D.M. Edwards *"Ferromagnetism and electron-phonon coupling in the manganites"*, cond-mat/0201558 (2002)

[14] P. Perna, Thesis in Physics, *"Effect of electron-phonons in manganites"*, Università "Federico II" di Napoli, (2003)

[15] C. Zener, *Phys. Rev.* 82, 403 (1951)

[16] P.G. de Gennes *"Effect of double exchange in magnetic crystal", Phys. Rev.* 118, 141 (1960)

[17] P.W. Anderson and H. Hasegawa, *"Considerations on double exchange", Phys. Rev.* 100(2), 675 (1955)

[18] J.B. Goodenough, *Phys. Rev.* 100, 564 (1955)

[19] A. Urushibara, Y. Moritomo, T. Arima, A. Asamitsu, G. Kido and Y. Tokura, *Phys. Rev. B* 51, 14103 (1995)

[20] S. Mercone, C. A. Perroni, V. Cataudella, C. Adamo, M. Angeloni, C. Aruta, G. De Filippis, F. Miletto, A. Oropallo, P. Perna, A. Yu. Petrov, U. Scotti di Uccio, and L. Maritato, *Phys. Rev. B* 71, 064415 (2005)

[21] S. Blundell, *"Magnetism in condensed matter", Oxford University Press* (2001)

[22] B. D. Cullity, Introduction to Magnetic Materials Addison-Wesley, Reading, MA (1972)

[23] A. Hubert and R. Schäfer, Magnetic domains: the analysis of magnetic microstructures, *Springer* (1998)

[24] Z.-H. Wang, G. Cristiani, H.-U. Habermeier, *Appl. Phys. Lett.* 82, 3731 (2003)

[25] K. Steenbeck, T. Habisreuther, C. Dubourdieu, and J. P. Sénateur, *Appl. Phys. Lett.* 80, 3361 (2002)

[26] O. Song, C.A. Ballentine and R.C. Ohandley, *Appl. Phys. Lett.* 64, 2593-2595 (1994)

[27] M. Koubaa, A. M. Haghiri-Gosnet, R. Desfeux, Ph. Lecoeur, W. Prellier, and B. Mercey, *J. Appl. Phys.* 93 (9), 5227 (2003)

[28] American Institute of Physics Handbook, edited by D. E. Gray McGraw-Hill, New York (1972)

[29] L.D. Landau and E.M. Lifshitz, *Phys. Z. Sowjetunion* 8, 153-169 (1935)

[30] C. Kittel, *Rev. Mod. Phys.* 21, 541-583 (1949)

[31] E.C. Stoner and E.P. Wohlfarth, *Phil. Trans. Roy. Soc.* A 240, 599-642 (1948)

[32] E. Dagotto, *Nanoscale Phase Separation and Colossal Magnetoresistance*, Springer Berlin (2003)

[33] A.J. Millis, P.B. Littlewood and B.I. Shraiman, *Phys. Rev. Lett.* 74(25), 5144 (1995)

[34] R. Von Helmolt, J. Wecker, B. Holzapfel, L. Schultz and K. Samwer, *Phys. Rev. Lett.* 71, 2331 (1993)

[35] J. N. Eckstein, I. Bozovic, J. O'Donnell, M. Onellion, and M. S. Rzchowski, *Appl. Phys. Lett.* 69 (9), 1312 (1996)

[36] R. Potter, *Phys. Rev. B* 10 (11), 4626 (1974); T.R. Mc Guire, R. Potter, *IEEE Transaction Mag.* 11 (4), 1018 (1975)

[37] W. Prellier, M. Rajeswari, T. Venkatesan, and R.L. Greene, *Appl. Phys. Lett.* 75, 1446 (1999)

[38] R. Shreekala, M. Rajeswari, R.C. Srivastava, K. Ghosh, A. Goyal, V.V. Srinivasu, S.E. Lofland, S.M. Bhagat, M. Downes, R.P. Sharma, S.B. Ogale, R.L. Greene, R. Ramesh, T. Venkatesan, R.A. Rao, and C.B. Eom, *Appl. Phys. Lett.* 74, 1886 (1999)

[39] W. Prellier, A. Biswas, M. Rajeswari, T. Venkatesan, and R.L. Greene, *Appl. Phys. Lett.* 75, 397 (1999)

[40] M. Izumi, Y. Ogimoto, Y. Konishi, T. Manako, M. Kawasaki, and Y. Tokura, *Mater. Sci. Eng. B* B84, 53 (2001)

[41] C. A. Perroni, V. Cataudella, G. De Filippis, G. Iadonisi, V. Marigliano Ramaglia, and F. Ventriglia, *Phys. Rev. B* 68, 224424 (2003)

[42] R. Di Capua, C. A. Perroni, V. Cataudella, F. Miletto Granozio, P. Perna, M. Salluzzo, U. Scotti di Uccio, and R. Vaglio, *J. Phys.: Condens. Matter* 18, 8195-8204 (2006)

[43] A. J. Millis, et al., *J. Appl. Phys.* 83 (3), 1588 (1998)

[44] F. Tsui, M.C. Smoak, T.K. Nath and C.B. Eom, *Appl. Phys. Lett.* 76 (17), 2421-2423 (2000)

[45] J. Z. Sun, D. W. Abraham, R. A. Rao, and C.B. Eom, *Appl. Phys. Lett.* 74, 3017 (1999)

[46] L. Abad, B. Martinez, and L. Balcells, *Appl. Phys. Lett.* 87, 212502 (2005)

[47] D.C. Worledge and T.H. Geballe, *Appl. Phys. Lett.* 76, 900 (2000)

[48] A. Plecenik, K. Fröhlich, J. P. Espinós, J. P. Holgado, A. Halabica, M. Pripko, and A. Gilabert, *Appl. Phys. Lett.* 81, 859 (2002)

[49] A. Abrutis, V. Plausinaitiene, V. Kubilius, A. Teiserskis, Z. Saltyte, R. Butkute, J. P. Senateur, *Thin Solid Films* 413, 32 (2002)

[50] C. Kwon, K.-C. Kim, M.C. Robson, J.Y. Gu, M. Rajeswari, T. Venkatesan, and R. Ramesh, *J. Appl. Phys.* 81, 4950 (1997)

[51] S.P. Chen, *J. Mater. Sci.* 13, 8148 (1998)

[52] B. Stäuble-Pümpin, B. Ilge, V.C. Matijasevic, P.M.L.O. Scholte, A.J. Steinfort and F. Tuinstra, *Surf. Sci.* 369, 313 (1996)

[53] F. Wang, M. Badaye, K. Ogawa and T. Morishita, *Appl. Surf. Sci.* 90, 123 (1995)

[54] R. Sum, R. Lüthi, H.P. Lang and H.-J. Güntherodt, *Physica C* 235-240, 621 (1994)

[55] N. Ikemiya, A.. Kitamura, S. Hara, *J. Cryst. Growth* 160, 104 (1996)

[56] T. Matsumoto, H. Tanaka, K. Kouguchi, T. Kawai and S. Kawai, *Surf. Sci.* 312, 21 (1994)

[57] H. Tanaka, T. Matsumoto, T. Kawai and S. Kawai, *Jpn. J. Appl. Phys.* 32, 1405 (1993)

[58] H. Tanaka, T. Matsumoto, T. Kawai and S. Kawai, *Surf. Sci.* 318, 29 (1994)

[59] Y. Liang and D.A. Bonell, *Surf. Sci.* 310, 128 (1994)

[60] Y. Liang, J.B. Rothman and D.A. Bonell, *J. Vac. Sci. Technol.* A12, 2276 (1994)

[61] M. Kawasaki, K. Takahashi, T. Maeda, R. Tsuchiya, M. Shinohara, O. Ishiyama, T. Yonezawa, M. Yoshimoto and H. Koinuma, *Science* 226, 1540 (1994)

[62] P.A.W. van der Heide, Q.D. Jiang, Y.S. Kim and J.W. Rabalais, *Surf. Sci.* 473, 59 (2001)

[63] R.K. Kawakami, E.J. Escorcia-Aparicio, Z.Q. Qiu, *Phys. Rev. Lett.* 77, 2570 (1996)

[64] R.A. Hyman, A. Zangwill, M.D. Stiles, *Phys. Rev. B* 58, 9276 (1998)

[65] T. Venkatesan, *et al.*, *Phil. Trans. R. Soc. London A* 356, 1661 (1998)

[66] J.-H. Kim and A. M. Grishim, *Appl. Phys. Lett.* 87, 033502 (2005)

[67] F. Yang, L. Méchin, J.-M. Routoure, B. Guillet, R.A. Chakalov, *J. Appl. Phys.* 99, 024903 (2006)

[68] A. Lisauskas, S. I. Khartsev, A. Grishin, *Appl. Phys. Lett.* 77(5), 756 (2000)

[69] P.L. Richards, *J. Appl. Phys.* 76(1) 1-24 (1994)

[70] L. Méchin, J.-C. Villégier and D. Bloyet, *J. Appl. Phys.* 81(10), 7039 (1997)

[71] A. Rogalski, *J. Appl. Phys.* 93(8), 4355 (2003)

[72] A. D. Semenov, *LLE Review* 87, 134 (2004)

[73] T. K. Cheng, S. D. Brorson, et al., *Appl. Phys. Lett.* 57(10), 1004 (1990); A. Rousse, C. Rischel, et al., *Nature* 410, 65 (2001)

[74] F. N. Hooge, *Phys. Lett. A* 29A, 139 (1969)

[75] J.-H. Kim, S. I. Khartsev, and A. M. Grishin, *Appl. Phys. Lett.* 82 (24), 4295 (2003)

[76] A. Palanisami., R.D. Merithew, M.B. Weissman, M.P. Warusawithana, F.M. Hess, J.N. Eckstein, *Phys. Rev. B* 66, 092407 (2002)

[77] B. Raquet, J.M.D. Coey, S. Wirth, S. von Molnar, *Phys. Rev. B* 59, 12435 (1999)

[78] A. Lisauskas, A. Lisauskas, S.I. Khartsev, J. Low Temp. Phys. 117, Nos. 5/6 1647 (1999); A.M. Grishin, V. Palenskis, *Mat. Res. Soc. Symp. Proc.* 574, 365 (1999)

[79] P.C. Shan, Z. Çelik-Butler, D.P. Butler, A. Janhanzeb, C.M. Travers, W. Kula, R. Sobolewski, *J. Appl. Phys.* 80 (12), 7118 (1996)

[80] V.Y. Zerov, V.G. Malyarov, *J. Opt. Technol.* 68 (12), 939 (2001)

[81] M. Jullière, *Phys. Lett.* 54A, 225 (1975)

[82] M. Bowen, M. Bibes, A. Barthélémy, J.-P. Contour, A. Anane, Y. Lemaitre, and A. Fert, *Appl. Phys. Lett.* 82, 233 (2003)

[83] M. Mathews, F.M. Postma, J.C. Lodder, R. Jansen, G. Rijnders, D.H. Blank, *Appl. Phys. Lett.* 87, 242507 (2005)

[84] P. Bruno, *Phys. Rev. Lett.* 83, 2425 (1999)

[85] J. Wolfman, A. M. Haghiri-Gosnet, B. Raveau, C. Vieu, E. Cambril, A. Cornette, and H. Launois, *J. Appl. Phys.* 89 (11), 6955 (2001)

[86] O. Céspedes, S. M. Watts, and J.M.D. Coey, K. Dörr, M. Ziese, *Appl. Phys. Lett.* 87, 083102 (2005)

[87] O. Céspedes, E. Clifford, and J.M.D. Coey, *J. Appl. Phys.* 97, 064305 (2005)

[88] C. Ruster, T. Borzenko, C. Gould, G. Schmidt, and L.W. Molenkamp, X. Liu, T. J.Wojtowicz, and J. K. Furdyna, Z.G. Yu and M. E. Flattè, *Phys. Rev. Lett.* 91, 216602 (2003)

[89] T. Arnal, A.V. Khvalokvskii, M. Bibes, Ph. Lecoeur, A.-M. Haghiri-Gosnet, and B. Mercey, *Phys. Rev. B* 75, 220409(R) (2007)

[90] S.M. Liu, et al., *Physica B* 353, 238 (2004)

[91] I. Bergenti, V. Dediu, M. Cavallini, E. Arisi, A. Riminucci, C. Taliani, *Current Applied Physics* 7, 47 (2007)

[92] W. Goh et al., *J. Appl. Phys.* 97, 073905 (2005)

[93] U. Scotti di Uccio, B. Davidson, R. Di Capua, F. Miletto Granozio, G. Pepe, P. Perna, A. Ruotolo, M. Salluzzo, *J. of All. and Comp.* 423, 228-231 (2006)

[94] D.B. Chrisey, G.K. Hubler, *Pulsed laser deposition of thin films*, John Wiley & Sons (1994)

[95] A. Sambri, S. Amoruso, X. Wang, M. Radovic', F. Miletto Granozio, and R. Bruzzese, *Appl. Phys. Lett.* 91, 151501 (2007)

[96] G. Rijnders, *"The Initial Growth of Complex Oxides: Study and manipulation"*, Doctoral Thesis, University of Twente, (2001)

[97] G. Koster, G.J.H.M. Rijnders, D.H.A. Blank, H. Rogalla, *Appl. Phys. Lett.* 74, 3729 (1999)

[98] M. Horn-VonHoegen, Z. Kristallogr. 214, 591 (1999)

[99] F. Miletto Granozio, F. Ricci, U. Scotti di Uccio, and J. C. Villagier, *Phys. Rev. B* 57, 6173 (1998)

[100] L. Méchin, P. Perna, M. Saïb, C. Barone, J.-M. Routoure, S. Flament, Ch. Simon, *Acta Physica Polonica A* 111(1) 63-70 (2007)

[101] J.-L. Maurice, F. Pailloux, A. Barthelemy, O. Durand, D. Imhoff, R. Lyonnet, A. Rocher and J. P. Contour, *Phil. Mag.* 83 (28), 3201 (2003)

[102] W. Xiang, R. Dong, D. Lee, S. Oh, D. Seong, and H. Hwanga, *Appl. Phys. Lett.* 90, 052110 (2007)

[103] Yoo, et al., *Appl. Phys. Lett.* 82, 4125 (2003); Yoo, et al., J*pn. J. Appl. Phys.* 45, 1788 (2006)

[104] G. Delhaye, C. Merckling, M. El-Kazzi, G. Saint-Girons, M. Gendry, Y. Robach, and G. Hollinger, *J. Appl. Phys.* 100, 124109 (2006)

[105] H. F. Tian, H. X. Yang, H. R. Zhang, Y. Li, H. B. Lu, and J. Q. Li, *Phys. Rev. B* 73, 075325 (2006)

[106] L. Méchin, J.C.Villégier, D. Bloyet, *Appl. Phys. Lett.* 70 (1), 123 (1996)

[107] R.A. McKee, F.J. Walker, M.F. Chisholm, *Phys. Rev. Lett.* 81, 3014 (1998)

[108] X.Y. Zhou, J. Miao, J.Y. Dai, H.L. W. Chan, C.L. Choy, Y. Wang, Q. Li, *Appl. Phys. Lett.* 90, 012902 (2007)

[109] L. Méchin, P. Perna, C. Barone, J.-M. Routoure, Ch. Simond, *Mater. Sci. Eng. B* 144, 73–77 (2007)

[110] A.K. Pradhan, et al., *J. Appl. Phys.* 100, 033903 (2006)

[111] A. K. Pradhan, et al., *Appl. Phys. Lett.* 86, 012503 (2005)

[112] J.-H. Kim, et al., *J. Appl. Phys.* 99, 014903 (2006)

[113] J.-H. Kim, A.M. Grishin, H.H. Radamson, *Thin Solid Films* 515, 411-415 (2006)

[114] J. Fontcuberta, et al., *Appl. Phys. Lett.* 74 (12), 1743 (1999)

[115] Z. Trajanovic, et al., *Appl. Phys. Lett.* 69 (7), 1005 (1996)

[116] C. Barone, A. Galdi, S. Pagano, O. Quaranta, L. Méchin, J.-M. Routoure, and P. Perna, *Rev. Sci. Instrum.* 78, 093905 (2007)

[117] J.-M. Routoure, L. Méchin, D. Fadil, C. Barone, S. Mercone, P. Perna, and S. Flament, *AIP Conf. Proc.* 922, 229 (2007)

[118] M. B. Salamon and M. Jaime, *Rev. Mod. Phys.* 73, 583 (2001)

[119] H. Y. Hwang, T. T. M. Palstra, S-W. Cheong, and B. Batlogg, *Phys. Rev. B* 52, 15046 (1995)

[120] Y. Suzuki, H. Y. Hwang, S. W. Cheong, and R. B. van Dover, *Appl. Phys. Lett.* 71, 140 (1997)

[121] X. W. Li, A. Gupta, Gang Xiao, and G. Q. Gong, *Appl. Phys. Lett.* 71, 1124 (1997)

[122] G. J. Snyder, R. Hiskes, S. DiCarolis, M. R. Beasley, and T. H. Geballe, *Phys. Rev. B* 53, 14 434 (1996); G. Li, H.-D. Zhou, S. J. Feng, X.-J. Fan, and X.-G. Li, *J. Appl. Phys.* 92, 1406 (2002)

[123] I. Mannari, *Prog. Theor. Phys.* 22, 335 (1959)

[124] K. Kubo and N. Ohata, *J. Phys. Soc. Jpn.* 33, 21 (1972)

[125] T. Akimoto, Y. Moritomo, A. Nakamura, and N. Furukawa, *Phys. Rev. Lett.* 85, 3914 (2000)

[126] P. Schiffer, A. P. Ramirez, W. Bao, and S.-W. Cheong, *Phys. Rev. Lett.* 75, 3336 (1995)

[127] X. Wang and X.-G. Zhang, *Phys. Rev. Lett.* 82, 4276 (1999)

[128] A. Gupta and J. Z. Sun, *J. Magn. Magn. Mater.* 200, 24 (1999); A. Gupta, G. Q. Gong, Gang Xiao, P. R. Duncombe, P. Lecouer, P. Trouilloud, Y. Y. Wang, V. P. Dravid, and J. Z. Sun, *Phys. Rev. B* 54, R15 629 (1996) and references therein

[129] C. A. Perroni, G. De Filippis, V. Cataudella, and G. Iadonisi, *Phys. Rev. B* 64, 144302 (2001)

[130] C. Thiele, K. Dörr, O. Bilani, J. Rödel, and L. Schultz, *Phys. Rev. B* 75, 054408 (2007)

[131] R. J. M. van de Veerdonk, J. Nowak, R. Meservey, J. S. Moodera, and W. J. M. de Jonge, *Appl. Phys. Lett.* 71, 2839 (1997)

[132] J. M. De Teresa, A. Barthélémy, A. Fert, J. P. Contour, F. Montaigne, and P. Seneor, *Science* 286, 507 (1999)

[133] M. Ziese, S. Sena, C. Shearwood, H. J. Blythe, M. R. J. Gibbs, and G. A. Gehring, *Phys. Rev. B* 57, 2963 (1998)

[134] M. Saïb, Doctoral Thesis, University of Caen-Basse Normandie (2007), http://tel.archives-ouvertes.fr/tel-00179291/fr/

[135] D. Zhao, F. Liu, D.L. Huber, M.G. Lagally, *Appl. Phys. Lett.* 91, 3150 (2002)

[136] R. P. Borges, W. Guichard, J. G. Lunney, and J. M. D. Coey, *J. Appl. Phys.* 89, 3868 (2001)

[137] A. Ruotolo, A. Oropallo, F. Miletto Granozio, G.P. Pepe, P. Perna, U. Scotti di Uccio, and D. Pullini, *Appl. Phys. Lett.* 91, 132502 (2007)

[138] R.H. Fowler and L.W. Nordheim, *Proc. Roy. Soc.* (London) 119, 173 (1928)

Manganiti a colossale magnetoresistenza per applicazioni nel campo della sensoristica

Paolo PERNA

Riassunto della tesi

Il premio 2007 Nobel nella fisica è stato assegnato ad A. Fert e P. Grünberg, per aver scoperto nel 1988 l'effetto della gigante magnetoresistenza in multilayers ferromagnetici (A. Fert, et al., Phys. Rev. Lett. 61, 2472 (1988), P. Grünberg et al., Phys. Rev. B 39, 4828 (1989)), inaugurando una nuova tecnologia, la spintronica, ossia spin-elettronica. Come indicato dal nome stesso, la spintronica è basata sul concetto che l'informazione possa essere trasportata non soltanto dalla carica, ossia dalla corrente elettrica, ma anche dagli spin degli elettroni.

Sebbene i dispositivi spintronici siano attualmente impiegati nell'elettronica convenzionale (come testine di lettura magnetiche per hard disk, memorie magnetiche ad accesso variabile, ecc.), la potenzialità di questa tecnologia non è ancora completamente sviluppata lasciando spazio ad una ricerca sia fondamentale che applicativa.
In questo contesto, una delle principali attività è la ricerca di nuovi materiali con proprietà adeguate.

Insieme ad altri materiali, gli ossidi perovskitici di manganese ferromagnetici risultano essere materiali molto promettenti. Inoltre, facendo ricorso alla tecnologia di fabbricazione di film sottili epitassiali è possibile integrare gli ossidi perovskitici sia con l'elettronica convenzionale basata sul silicio sia con l'elettronica innovativa basata su materiali ossidi.
Gli ossidi perovkitici di manganese hanno suscitato grande interesse della comunità scientifica allorquando l'effetto della colossale magnetoresistenza è stato scoperto nei film sottili. Questo effetto consiste in una forte riduzione della resistenza elettrica sotto l'effetto di un campo magnetico applicato. Purtroppo, quest'effetto si ha soltanto per alti campi magnetici, rendendo di fatto difficile l'applicazione di questa tecnologia. Tuttavia, le manganiti possiedono altre caratteristiche interessanti.

In questa tesi, discuto in particolare di quanto segue:

1. le maganiti mostrano una forte variazione di resistività intorno alla temperatura di Curie. Ciò può essere utlizzato per applicazioni come i sensori di temperatura o bolometri. Il coefficiente di temperatura della resistenza (TCR), definito come $TCR = \frac{1}{\rho}\frac{d\rho}{dT}$ che è molto elevato nelle manganiti, è una figura di merito molto importante nell'ambito dei dispositivi bolometrici.
2. le manganiti sono eccellenti half-metal, ossia gli elettroni liberi sono quasi completamente polarizzati in spin; ciò è essenziale quando si vuole impiegarli per alimentare con una corrente polarizzata in spin nei dispositivi spintronici. La polarizzazione di spin, definita come $P = \frac{N_\uparrow(E_F) - N_\downarrow(E_F)}{N_\uparrow(E_F) + N_\downarrow(E_F)}$ è quasi del 100% nelle manganiti rendendo un elevato valore di magnetoresistenza (MR) definita come $MR = \frac{R_H - R_0}{R_0}$.

In questo contesto, il mio lavoro sperimentale è stato dedicato allo studio della manganite $La_{0.7}Sr_{0.3}MnO_3$ (LSMO), che è un robusto ferromagnete, con la più alta temperatura di Curie (T_C) fra le maganiti. In fig. 1 è mostrata la curva di R(T) e M(T) per un film di LSMO ed in fig. 2 lo schema della densità degli stati (DOS) per una manganite ed un normale ferromagnete.

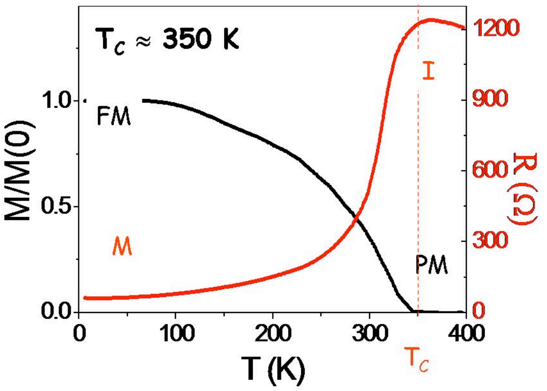

Figura 1 R(T) e M(T) per un film di LSMO depositato su STO (110).

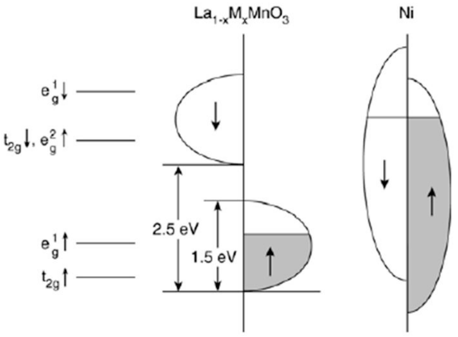

Figura 2 DOS del LSMO e del Ni.

Le applicazioni tecnologiche richiedono altresì un altissimo controllo del processo di crescita di film sottili epitassiali. Per questo motivo ho utilizzato diverse tecniche di deposizione (sputtering, ablazione laser, ablazione laser assistita da RHEED, ossia diffrazione elettronica ad alta energia), e di indagine delle proprietà fisiche dei film e dei multilayers realizzati. Infine presento dei prototipi di dispositivi atti a dimostrare la funzionalità del LSMO nell'ambito della spintronica.

Questo lavoro ha richiesto l'utilizzo di molte tecniche sperimentali differenti ed è stato possibile soltanto grazie alla cooperazione tra le due istituzioni che hanno coordinato questo PhD, ossia l'università di Cassino (Italia) ed il laboratorio GREYC - Università di Caen/Basse Normandie (Francia) ed il laboratorio MODA del CNR/INFM Coherentia Napoli (Italia).

Film sottili di LSMO

Le prestazioni finali dei dispositivi basati su film di manganiti dipendono dalla capacità di fabbricare i film epitassiali di alta qualità. Esistono numerosi metodi per fabbricare film di ossidi. Ad ogni modo, i metodi fisici di deposizione, quali lo sputtering e l'ablazione laser, risultano i più adatti a realizzare film epitassiali e rendono possibile un notevole controllo della crescita dei film.

Lo sputtering è una tecnica molto utilizzata nei processi industriali data la possibilità di depositare su grandi aree e per i bassi costi, ma di contro manifesta una bassa flessibilità poiché soltanto pochi parametri di deposizione possono essere direttamente controllati. D'altra parte l'ablazione laser è una tecnica molto adatta quando si vogliono depositare strati di materiali diversi in sequenza, il che indubbiamente rappresenta un notevole vantaggio nella fabbricazione di dispositivi. Tuttavia, le piccole aree di deposizione rendono l'ablazione laser una tecnica principalmente dedicata alla ricerca fondamentale.

In questo lavoro, ho fabbricato film sottili di LSMO sui substrati differenti di singolo cristallo usando la tecnica dello sputtering e dell'ablazione laser assistita da RHEED nel laboratorio CNR-INFM Coherentia M.O.D.A. a Napoli. Inoltre, nel laboratorio GREYC a Caen ho fabbricato film di LSMO su substrati di singolo cristallo e su substrati di silicio utilizzando una tecnica di deposizione laser pulsata (PLD).
In primo luogo, ho dedicato particolare attenzione all'ottimizzazione dei parametri di deposizione al fine di ottenere film di alta qualità. Dunque, ho studiato la struttura, le proprietà di trasporto, magnetiche e morfologiche dei film facendo ricorso a diverse tecniche sperimentali sia in-situ che ex-situ, seguendo gli obiettivi delle applicazioni descritte sopra.
In questo capitolo, descrivo le tecniche suddette e le proprietà dei film di LSMO cresciuti su substrati di $SrTiO_3$ (STO) in diverse orientazioni cristallografiche, (001) e (110), e su substrati di STO vicinali. In quanto segue mostro le proprietà più rappresentative dei film di LSMO depositati su STO (001).

Proprietà di superficie

Per studiare le superfici dei campioni ho fatto ricorso alla diffrazione elettronica ad alta energia (RHEED) ad incidenza radente, disponibile al laboratorio di M.O.D.A. a Napoli, che permette di avere un'elevata sensibilità alla superficie. Questa tecnica è usata come tecnica di controllo in-situ per studiare la crescita dei film durante la deposizione. Essa fornisce informazioni sulla disposizione periodica degli atomi di superficie. Le oscillazioni tipiche di RHEED effettuate durante la crescita del LSMO su un substrato di STO (001) sono illustrate in fig. 3.

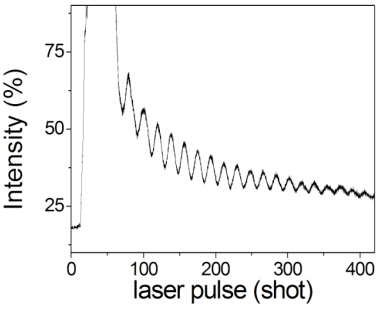

Figura 3 Oscillazioni RHEED della riflessione (0,0) sulla superficie del LSMO depositato su STO (001).

Proprietà strutturali

Ho eseguito misure di diffrazione a raggi X per l'indagine strutturale dei campioni di LSMO, depositati mediante le tecniche menzionate sopra. Le analisi di XRD sono state compiute usando un diffrattometro a due-assi in geometria Bragg-Brentano. Ho effettuato misure di rocking e misure ad incidenza radente per controllare la qualità cristallografica dei campioni. I piccoli valori di FWHM ottenuti risultano entro la risoluzione del diffrattometro dimostrando l'alta qualità strutturale dei campioni (fig. 4). Inoltre, le oscillazioni a bassi angoli ottenute da misure standard θ-2θ dimostrano la bassa rugosità superficiale. Una tipiche misura θ-2θ intorno alla riflessione (002) è illustrata in fig 4.

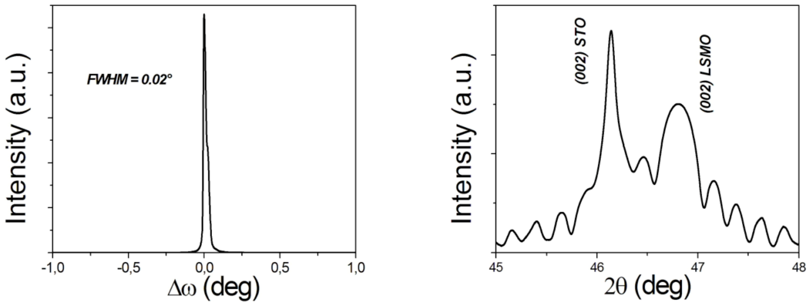

Figura 4 Rocking curve e θ-2θ di un film di LSMO su STO (001).

Proprietà morfologiche

Ho studiato la morfologia de film realizzando le misure di microscopia a forza atomica (AFM) e a scansione tunnel (STM). Come si evince dalle Fig. 5 i film di LSMO depositati su substrati di STO (001) sono atomicamente piatti, mostrando una rugosità dell'ordine del parametro reticolare, anche per film di spessore fino 75nm. Inoltre, microscopie a scansione tunnel su aree più piccole (500x500nm^2) mostrano terrazze di 80nm di larghezza.

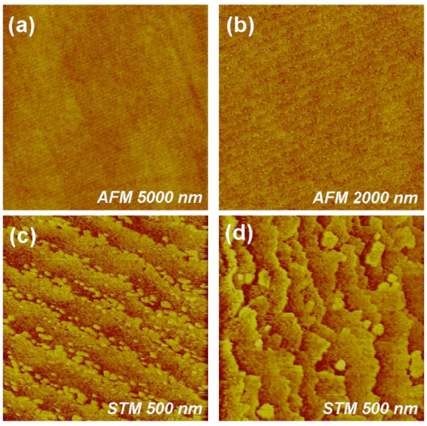

Figura 5 AFM e STM di un film di LSMO su STO (001) di spessore 75nm.

Proprietà di trasporto

In fig. 6 è mostrato il comportamento della resistenza in funzione della temperatura e della magnetizzazione in funzione della temperatura per tre campioni di LSMO depositati su un substrato di STO (001) ottenuti mediante sputtering, PLD e nell'ablazione assistita da RHEED. Tali film mostrano resistività residue molto basse e una temperatura di Curie sempre al di sopra della temperatura ambiente, che indicano un'elevata qualità dei film.

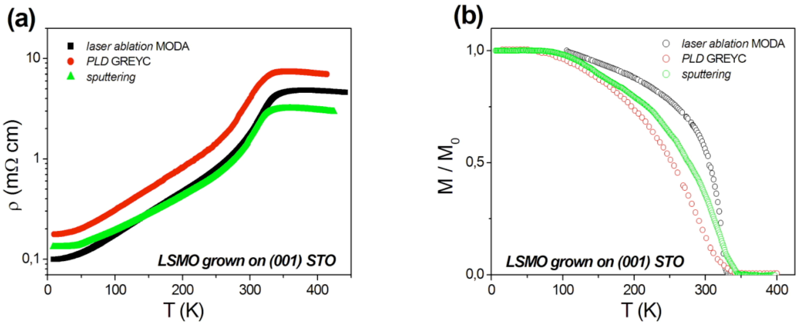

Figura 6 R(T) e M(T) dei film di LSMO su STO (001) ottenuti con 3 diverse tecniche di deposizione.

Film sottili di LSMO depositati su substrati di silicio

Per rispondere all'esigenza industriale di una tecnologia a basso costo, la realizzazione di film sottili su substrati di silicio risulta essere un primo passo fondamentale per l'integrazione con l'elettronica convenzionale. Nonostante la difficoltà di depositare film di ossidi epitassiali su substrati di silicio a causa della presenza di ossido di silicio amorfo sulla superficie del silicio, della diffusione di ossigeno alle alte temperature di deposizione del LSMO e dei differenti coefficienti di espansione termica del silicio e del LSMO, è possibile ricorrere all'utilizzo di buffers al fine di creare una barriera di diffusione tra il Si ed il LSMO. La tecnica della PLD è inoltre la più indicata per realizzare strutture a multistrato. A tal fine ho realizzato 2 differenti multilayer, ossia LSMO/$Bi_4Ti_3O_{12}$ (BTO)/CeO_2/YSZ/Si e $SrTiO_3$/CeO_2/YSZ/Si, che chiamerò rispettivamente BTO-based e STO-based. Ho dunque ottimizzato le condizioni di crescita di ogni layer per ottenere film di LSMO di buona qualità cristallografica, superfici piatte ed alte temperature di Curie.
In fig. 7 sono illustrate le curve θ-2θ dei multilayer descritti sopra, dimostrando sempre un'ottima epitassia.

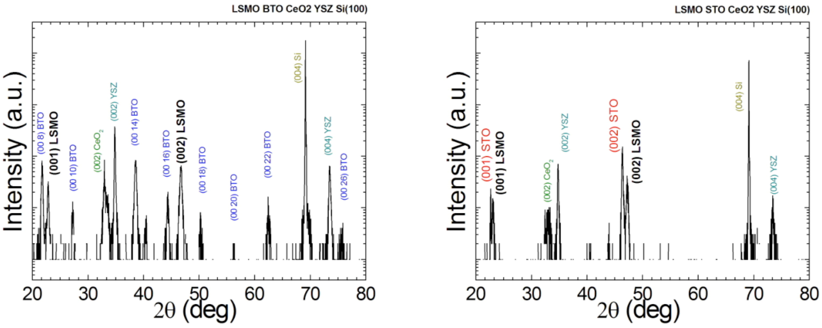

Figura 7 θ-2θ dei multilayer BTO-based (sx) e STO-based (dx).

In fig. 8 sono illustrate le curve di R(T) dei multilayers a confronto con il comportamento della resistività in funzione della temperatura di un campione di LSMO depositato su singolo cristallo di STO (001).

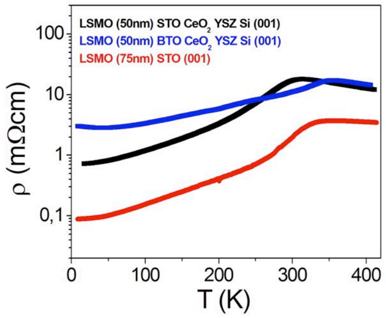

Figura 8 Resistività in funzione della temperatura dei multilayer BTO- e STO-based a confronto con LSMO su STO (001)

Proprietà di trasporto e magnetiche di film sottili di LSMO

L’oggetto di questo capitolo è lo studio delle proprietà di trasporto e magnetiche dei film di LSMO realizzati nelle diverse fasi che caratterizzano questi materiali al variare della temperatura. Dunque, considero la transizione metallo-isolate (MIT) e la separazione (PS) tra la fase ferromagnetica ed la paramagnetica. In fig. 9 sono mostrate le curve di resistività in funzione della temperatura di 2 campioni di LSMO depositati su STO (001) e su STO (110).

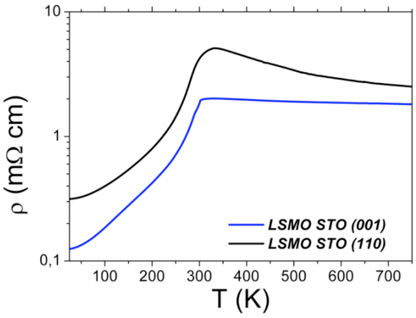

Figura 9 Resistività in funzione della temperatura di film sottili di LSMO su STO (001) e su STO (110).

Per interpretare le proprietà di trasporto, ho considerato un modello basato sulla separazione:

$$\rho = \rho_{FM} \cdot f + \rho_{PI} \cdot (1 - f)$$

dove $\rho_{FM} = \rho_0 + A \cdot T^{\alpha}$ con $\alpha \approx 2.5$

e $\rho_{PI} = \sqrt{T} \exp\left\{ E_0 / k_B T \right\}$ con $E_0 \approx 65 meV$ energia di attivazione.

La funzione f rappresenta la frazione di volume delle regioni FM del sistema mentre (1-f) rappresenta la frazione di volume delle regioni paramagnetiche.

Lo strain indotto dal substrato agisce fortemente sulle proprietà di trasporto del LSMO. Per questo motivo risulta importante studiare le relazioni tra la temperatura di Curie e lo strain. Di seguito interpreto queste relazioni nell’ambito della teoria corrente proposta da Millis et al. L'equazione che collega T_C alla strain di bulk massa (ε_B) ed allo strain biassiale (ε^*) è:

$$T_C(\varepsilon) = T_0 \cdot (1 - a\varepsilon_B - b\varepsilon^{*2})$$

dove T_0 è la temperatura di Curie del LSMO non soggetto a strain. In tutti i casi la temperatura di Curie è valutata dalle misure di M(T). In fig. 10 sono graficati i valori dello strain di bulk e dello strain biassiale dovuto all'effetto Jahn-Teller e della temperatura di Curie in funzione dello spessore dei film di LSMO depositati su substrati di STO (001). Ho determinato la temperatura di Curie dalla procedura di fit T_0=363K, $a = \frac{1}{T_0}\frac{dT_C}{d\varepsilon_B} \approx 12$ e $b = \frac{1}{T_0}\frac{d^2T_C}{d\varepsilon^{*2}} \approx 1000$.

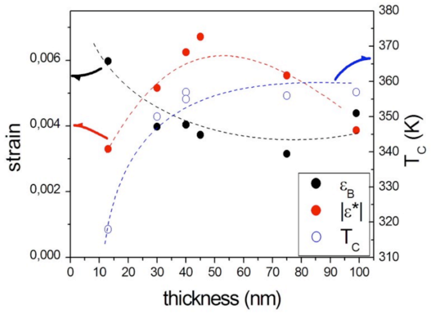

Figura 10 Andamento dello strain e della temperatura di Curie in funzione dello spessore dei film di LSMO su STO (001).

Dispositivi spintronici basati su film di LSMO

Gli effetti di CMR e di AMR nelle manganites richiedono campi magnetici abbastanza grandi (dell'ordine dei Tesla). Quindi, per applicazioni tecnologiche si rendono necessari dispositivi che sfruttano effetti magnetoresistivi con l'appplicazione di bassi campi magnetici, come valvola di spin e giunzioni magnetiche.

In questa tesi, discuto tre differenti esperimenti. Il primo interessa giunzioni Py/LSMO depositato su STO (110) sfruttando il dead-layer, ossia uno strato non magnetico che si forma sulla superficie di ogni materiale ferromagnetico, come spacer tra i 2 strati ferromagnetici. In fig. 11 è riportata la curva di magnetoresistenza tunnel misurata su questo tipo di dispositivo.

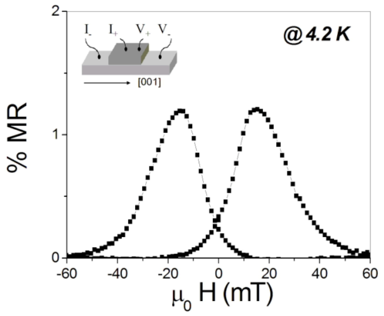

Figura 11 MR del dispositivo LSMO/Py.

Il secondo esperimento riguarda film di LSMO depositati su substrati vicinali di STO (001). Poichè gli step indotti dalla vicinalità del film inducono un'anisotropia uniassiale è possibile amplificare l'effetto magnetoresistivo applicando bassi campi magnetici parallelamente e perpendicolarmente ai suddetti step (fig. 12).

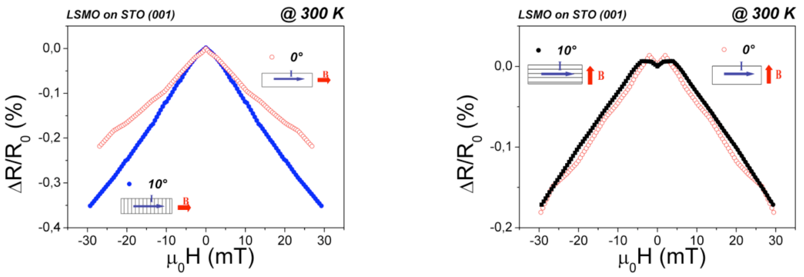

Figura 12 MR di un film di LSMO depositato su un substrato vicinale 10° di STO (001).

L'ultimo esperimento riguarda la fabbricazione di giunzioni magnetiche su film di LSMO cresciuti su substrati di STO (110) realizzando nanocostrizioni. La curva di MR ottenuta è riportata in fig. 13.

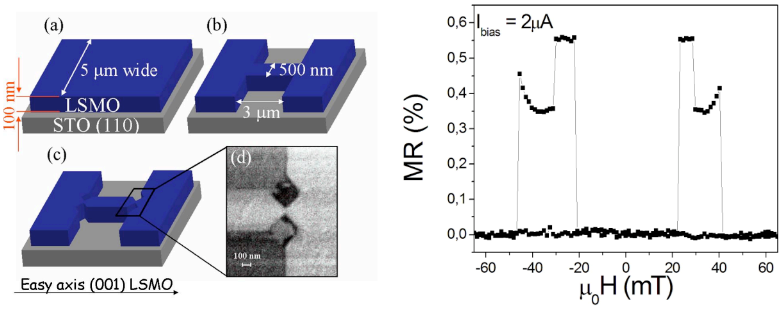

Figura 13 MR di una doppia parete di dominio realizzata mediante nanocostrizioni su un film di LSMO cresciuto su STO (110).

Manganites à colossale magnétorésistance pour la réalisation de capteurs

Paolo PERNA

Résumé

Le prix Nobel de physique 2007 a été attribué à A. Fert et P. Grünberg, pour avoir découvert en 1988 l'effet de la magnétoresistance géante dans des multicouches ferromagnétiques (A. Fert *et al.*, Phys. Rev. Lett. 61. 2472 (1988), P. Grünberg *et al*, Phys. Rev. B 39, 4828 (1989)). Ils ont ouvert tout un champ de recherche nouveau, la spintronique, ou électronique de spin. Comme son nom l'indique, la spintronique est basée sur le fait que l'information est non seulement transportée par la charge des électrons de conduction, mais également leur spin.

Même si certains dispositifs spintroniques sont actuellement utilisés dans l'électronique conventionnelle (dans les têtes de lecture magnétiques pour disques durs, les mémoires magnétiques, etc), la potentialité de cette technologie n'est pas encore complètement développée. Elle offre de nombreuses perspectives en recherche fondamentale ou appliquée.

Dans ce contexte, une des principales activités est la recherche de nouveaux matériaux aux propriétés optimisées. Les oxydes de manganèse à valence mixte, également appelés manganites, sont des matériaux très prometteurs. En outre, en utilisant les technologies de fabrication de films minces épitaxiés, il est potentiellement possible d'associer ces oxydes de structure pérowskite soit avec une électronique conventionnelle basée sur le silicium soit avec une électronique innovante basée sur des oxydes. Les manganites ont suscité un très grand intérêt de la communauté scientifique quand l'effet de la magnétorésistance colossale a été découvert dans les films minces. Cet effet consiste en une forte réduction de la résistance électrique sous l'effet d'un champ magnétique appliqué. Malheureusement, cet effet existe seulement pour des forts champs magnétiques, ce qui rend difficile les applications directes de cette technologie, mais nécessite la réalisation d'hétérostructures ou de dispositifs plus complexes.

Dans ce travail de thèse, j'ai plus particulièrement considéré deux propriétés intéressantes pour la réalisation de capteurs :

1. les manganites montrent une forte variation de résistivité ρ autour de la température de Curie. Cela peut être exploité pour des applications comme les capteurs de température ou les bolomètres. Le coefficient de température de la résistance (TCR), défini comme $TCR = \frac{1}{\rho}\frac{d\rho}{dT}$ définit la sensibilité du thermomètre. Il est assez élevé dans les manganites, ce qui rend ces matériaux prometteurs pour la réalisation de bolomètres.
2. les manganites sont des excellents demi-métaux, ce qui signifie que les électrons libres sont presque entièrement polarisés en spin ; cela est essentiel lorsqu'on veut les utiliser pour alimenter des dispositifs spintroniques avec un courant polarisé en spin. La polarisation de spin, définie comme $P = \frac{N_\uparrow(E_F) - N_\downarrow(E_F)}{N_\uparrow(E_F) + N_\downarrow(E_F)}$ est proche de 100% dans les manganites. Cela conduit à une valeur élevée de magnétorésistance (MR) définie comme $MR = \frac{R_H - R_0}{R_0}$.

J'ai concentré mon travail expérimental à l'étude de la composition $La_{0.7}Sr_{0.3}MnO_3$ (LSMO), qui est ferromagnétique, avec une température de Curie (T_C) de l'ordre de 360 K, ce qui permet d'envisager sont utilisation à température ambiante. La figure 1 présente des courbes typiques de résistance R(T) et d'aimantation M(T) en fonction de la température pour des films de LSMO. Le schéma de la densité d'état (DOS) pour une manganite et un matériau ferromagnétique normal est rappelé dans la figure 2.

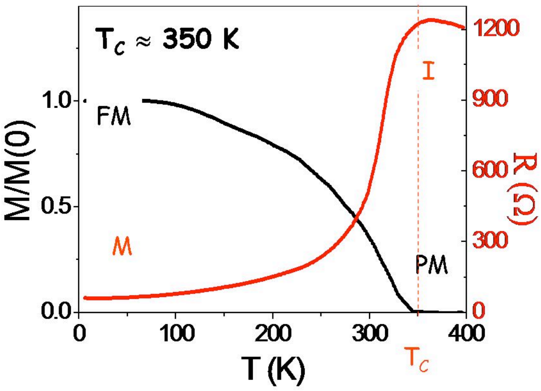

Figure 1 : Caractéristiques typiques de résistance R(T) et d’aimantation M (T) en fonction de la température pour des films de LSMO déposés sur STO (110).

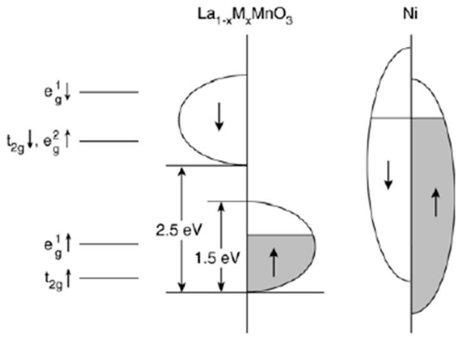

Figure 2 : densité d’état (DOS) de LSMO et Ni.

Les applications technologiques demandent un très grand contrôle des procédés de croissance épitaxiée de films minces. Dans ce but, j'ai utilisé différentes techniques de dépôt (pulvérisation cathodique, ablation laser, ablation laser assistée de RHEED – *Reflected High Electron Energy Diffraction*), et caractérisé de façon détaillée les propriétés physiques des films et des multicouches réalisés. A la fin de ce travail, je présente la réalisation de prototypes de dispositifs permettant de montrer l’intérêt de LSMO dans le domaine des capteurs.

Ce travail a nécessité l'utilisation de beaucoup de techniques expérimentales différentes et a été possible seulement grâce à la coopération entre les deux institutions qui ont coordonné cette thèse, c'est-à-dire l'université de Cassino (Italie) et le laboratoire GREYC - Université de Caen Basse- Normandie (France), ainsi que le laboratoire MODA de CNR/INFM Coherentia à Naples (Italie).

Les couches minces de LSMO

Les qualités finales des dispositifs basés sur les films de manganites dépendent de façon évidente de la capacité à fabriquer les films épitaxiés de haute qualité. Il existe de nombreuses méthodes pour fabriquer des films épitaxiés d'oxydes. Parmi celles-ci, les méthodes physiques de dépôt, telles que la pulvérisation cathodique et l'ablation laser pulsée (PLD – *Pulsed Laser Deposition*), se révèlent être les plus adaptées pour réaliser des couches minces épitaxiées en rendant possible le contrôle de la croissance des films.

La pulvérisation cathodique est une technique très utilisée dans les procédés industriels car elle donne la possibilité de déposer sur des grandes surfaces à relativement bas coût, mais peu de paramètres de dépôt peuvent être directement contrôlés. L'ablation laser est une technique très adaptée lorsqu'on veut déposer des couches de matériaux différents en séquence, ce qui présente un avantage considérable dans la fabrication de dispositifs. Toutefois, la petite surface de dépôt qu'il est possible d'obtenir par ablation laser rend cette technique principalement dédiée à la recherche fondamentale.

Dans ce travail, j'ai fabriqué des films minces de LSMO sur différents substrats monocristallins de $SrTiO_3$ (STO) en employant la technique de pulvérisation cathodique et d'ablation laser assistée de RHEED au laboratoire de CNR-INFM Coherentia M.O.D.A. à Naples. En outre, au laboratoire GREYC à Caen, j'ai fabriqué des films minces de LSMO sur des substrats monocristallins de STO et de silicium en utilisant une technique de dépôt par ablation laser pulsée. Tout d'abord, j'ai porté une grande attention à l'optimisation des conditions de dépôt afin d'obtenir des films de grande qualité. J'ai étudié la structure, les propriétés de transport, magnétiques et morphologiques des films en utilisant différentes techniques expérimentales in-situ (dans M.O.D.A.) ou ex-situ, avec pour objectifs les applications décrites dans le dernier chapitre. Dans le chapitre 3, je décris les techniques expérimentales utilisées et les propriétés des films de LSMO déposés sur des substrats de STO de différentes orientations cristallographiques : (001), (110), et vicinaux. Dans la suite, je vais présenter les propriétés les plus représentatives des films de LSMO déposés sur substrat de STO (001).

Propriétés de surface

Pour étudier les propriétés de surface des échantillons, j'ai utilisé la diffraction électronique à haute énergie (RHEED) en incidence rasante, disponible au laboratoire M.O.D.A. à Naples, qui permet d'avoir une sensibilité élevée à la surface. Cette technique est employée comme technique de contrôle in-situ pour étudier la croissance des films pendant le dépôt. Elle fournit des informations sur la disposition périodique des atomes de surface. Des oscillations typiques de RHEED obtenues pendant la croissance de LSMO sur un substrat de STO (001) sont présentées en fig. 3.

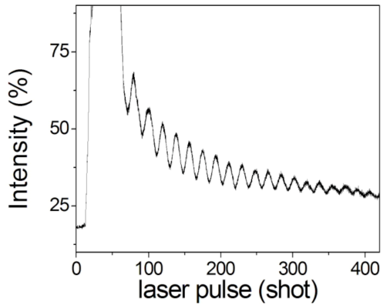

Figure 3 : Oscillations RHEED de la réflexion (0,0) à la surface d'un film de LSMO déposé sur STO (001).

Propriétés structurales

J'ai effectué des mesures de diffraction de rayons X (XRD – *X-Ray Diffraction*) pour l'analyse structurale des échantillons de LSMO. Les analyses XRD ont été effectuées en employant un diffractomètre à deux axes en géométrie Bragg- Brentano. Des mesures de *rocking curve* et des mesures en incidence rasante ont permis de révéler la grande qualité cristallographique des échantillons. Les largeurs des pics à mi-hauteur (FWHM - *Full Width at Half Maximum*) mesurées étaient limitées par la résolution du diffractomètre (fig. 4). En outre, les oscillations observées lors des mesures en configuration standard θ-2θ sont caractéristiques d'une très faible rugosité de surface. Des mesures typiques en configuration ω-scan autour de la réflexion (002) (*rocking curve*) et θ-2θ sont présentées en figure 4.

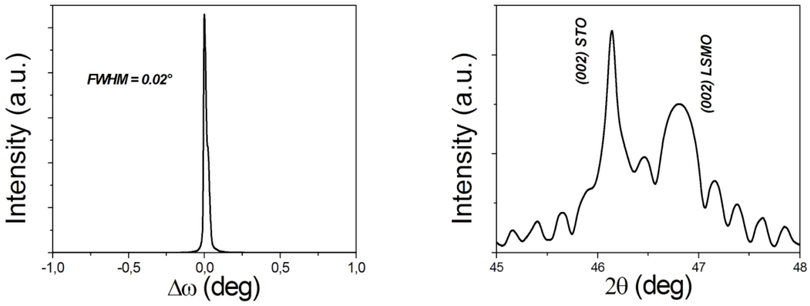

Figure 4 : Rocking curve et θ-2θ typiques d'un couche mince de LSMO sur STO (001).

Propriétés morphologiques

J'ai étudié la morphologie des films en réalisant des mesures de microscopie à force atomique (AFM) et à effet tunnel (STM). Comme le montre la figure 5, les films de LSMO déposés sur des substrats de STO (001) sont atomiquement plats, en montrant une rugosité de l'ordre du paramètre de maille, même des films d'épaisseur 75nm. En outre, des images STM sur des surfaces plus petites (500x500nm^2) montrent la présence de terrasses de largeur environ 80 nm.

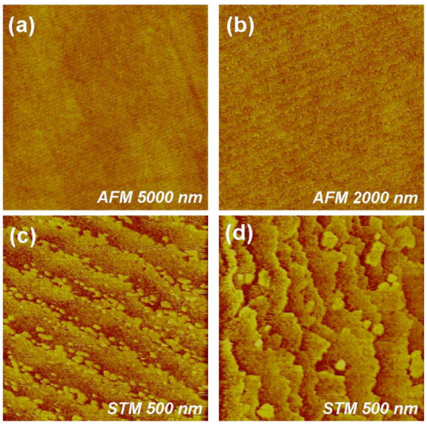

Figure 5 : Images AFM et STM de couches minces de LSMO (d'épaisseur 75nm) déposées sur STO (001).

Propriétés de transport

La figure 6 présente le comportement de la résistance et de l'aimantation en fonction de la température pour trois échantillons sélectionnés de LSMO déposés sur un substrat de STO (001) obtenus par pulvérisation cathodique, PLD et PLD assistée de RHEED. Ces films montrent des valeurs très faibles de résistivité résiduelles et une température de Curie toujours au-dessus de la température ambiante, qui indiquent la très grande qualité des films.

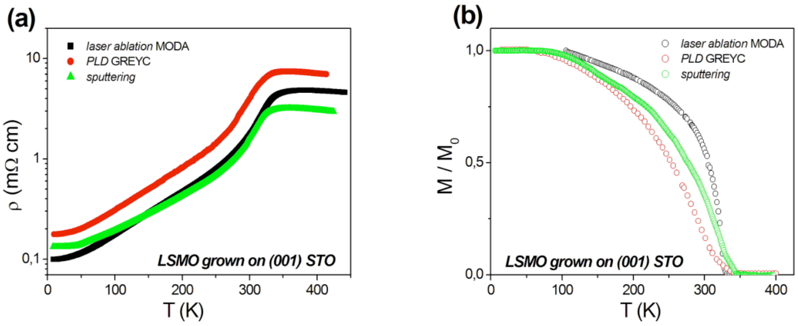

Figure 6 : Caractéristiques typiques de résistance R(T) et d'aimantation M (T) en fonction de la température pour des films de LSMO déposés sur STO (001) par les 3 techniques de dépôt.

Couches minces de LSMO déposées sur des substrats de silicium

Pour répondre à l'exigence industrielle d'une technologie à bas coût et pour permettre l'intégration avec l'électronique conventionnelle, la réalisation de films minces de LSMO sur des substrats de silicium est indispensable. Le dépôt de films d'oxyde épitaxiés sur des substrats de silicium est difficile à cause de la présence d'oxyde de silicium amorphe à la surface du Si, de la diffusion d'oxygène aux hautes températures de dépôt de LSMO et des différences de coefficients de dilatation thermique entre le silicium et LSMO. Pour résoudre ces problèmes, il est possible d'utiliser des couches tampons afin de créer une barrière de diffusion entre Si et LSMO. La technique de PLD est particulièrement bien indiquée pour réaliser ces structures multicouches. J'ai réalisé 2 multicouches différentes : LSMO/$Bi_4Ti_3O_{12}$(BTO)/CeO_2/YSZ/Si et LMSO/$SrTiO_3$/CeO_2/YSZ/Si, que j'appellerai par la suite respectivement « BTO-based » et « STO-based ». J'ai optimisé les conditions de croissance pour chaque couche afin d'obtenir des films de LSMO de grande qualité cristallographique, de faible rugosité et des températures de Curie élevées.

La figure 7 présente les diffractogrammes de rayons X en configuration θ-2θ des deux types de multicouches décrites ci-dessus. Dans chaque cas, une orientation de chaque couche dans la direction (001) a été obtenue.

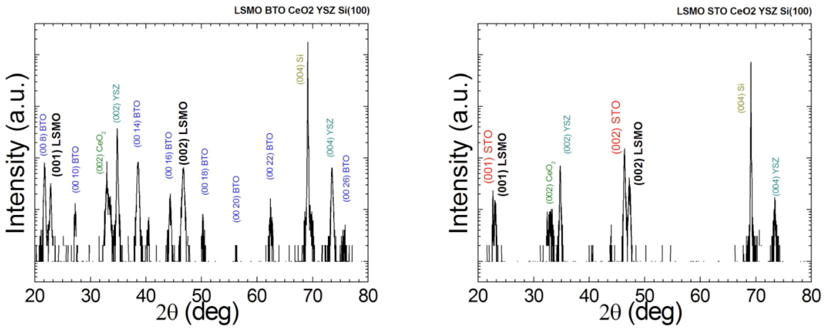

Figure 7 : Diffractogrammes de rayons X en configuration θ-2θ des multicouches BTO-based (à gauche) et STO-based (à droite).

La figure 8 rassemble les courbes de résistivité en fonction de la température des 2 multicouches comparées avec celle obtenue sur une couche de LSMO déposée sur un monocristal de STO (001).

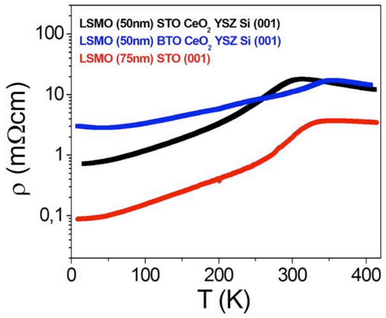

Figure 8 : Résistivité en fonction de la température des 2 multicouches BTO- et STO-based comparées avec celle de LSMO sur STO (001)

Propriétés de transport et magnétiques de couches minces de LSMO

L'objet de ce chapitre est d'étudier les propriétés de transport et magnétiques des films de LSMO dans les différentes phases qui caractérisent ces matériaux en fonction de la température. J'ai alors considéré la transition métal-isolant (MIT) et la séparation (PS) entre la phase ferromagnétique et la phase paramagnétique. La figure 9 représente les courbes de résistivité en fonction de la température des 2 échantillons de LSMO déposés sur STO (001) et sur STO (110).

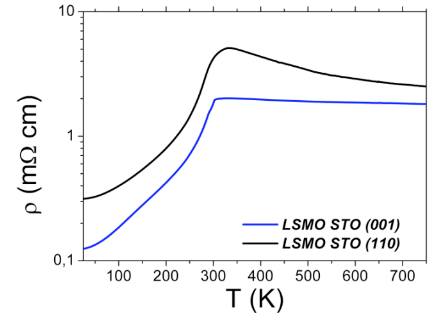

Figure 9 : Résistivité en fonction de la température de couches minces de LSMO déposées sur STO (001) et sur STO (110).

Pour interpréter ces propriétés de transport, j'ai considéré un modèle basé sur la séparation de phase:

$$\rho = \rho_{FM} \cdot f + \rho_{PI} \cdot (1 - f)$$

où $\rho_{FM} = \rho_0 + A \cdot T^{\alpha}$ avec $\alpha \approx 2.5$

et $\rho_{PI} = \sqrt{T} \exp\left\{ E_0 / k_B T \right\}$ avec $E_0 \approx 65 meV$ l'énergie d'activation.

La fonction f représente la fraction de volume des régions FM du système alors que (1-f) représente la fraction de volume des régions paramagnétiques.

La contrainte induite par le substrat agit fortement sur les propriétés de transport du LSMO. Pour cette raison, il s'avère important d'étudier la relation entre la température de Curie et la contrainte. Dans la suite, j'interprète ces relations en me basant sur la théorie proposée par Millis *et al*. L'équation qui relie T_C à la contrainte de volume (ε_B) et à la contrainte biaxiale (ε*) est :

$$T_C(\varepsilon) = T_0 \cdot (1 - a\varepsilon_B - b\varepsilon^{*2})$$

où T_0 est la température de Curie de LSMO non contraint. Dans tous les cas, la température de Curie est évaluée par des mesures d'aimantation en température.

La figure 10 rassemble les valeurs de contrainte en volume et de contrainte biaxiale dûes à l'effet Jahn- Teller sur l'axe de gauche, et la température de Curie sur l'axe de droite en fonction de l'épaisseur des films de LSMO déposés sur des substrats de STO (001). La température de Curie a été déterminée par ajustement avec T_0=363K, $a = \frac{1}{T_0}\frac{dT_C}{d\varepsilon_B} \approx 12$ e $b = \frac{1}{T_0}\frac{d^2T_C}{d\varepsilon^{*2}} \approx 1000$.

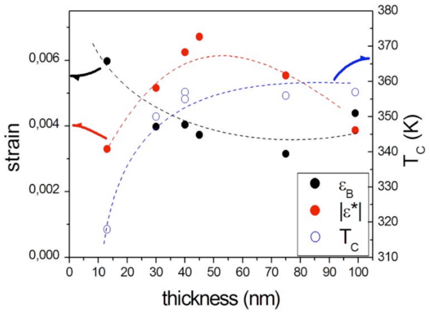

Figure 10 : Evolution de la contrainte de volume (ε_B), de la contrainte biaxiale (ε*), et de la température de Curie en fonction de l'épaisseur des couches minces de LSMO sur STO (001).

Dispositifs spintroniques basés sur des couches minces de LSMO

Les effets de CMR et d'AMR dans les manganites existent sous l'application de champs magnétiques assez grands (de l'ordre du Tesla). Pour réaliser des applications exploitant des effets magnétorésistifs pour des applications de faible champ magnétique, il est nécessaire de réaliser des dispositifs tels que des vannes de spin et des jonctions magnétiques.

Dans cette thèse, je présente trois exemples de dispositifs. Le premier concerne des jonctions Permalloy(Py)/LSMO déposées sur STO (110) qui exploitent la couche morte, c'est-à-dire une couche non magnétique qui se forme à la surface de chaque matériau ferromagnétique, comme espaceur entre les 2 couches ferromagnétiques. La figure 11 présente la magnétorésistance tunnel mesurée sur ce type de dispositif.

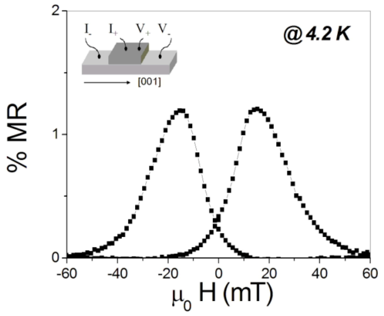

Figure 11 : MR du dispositif LSMO/Py.

Le second dispositif utilise des films de LSMO déposés sur des substrats vicinaux de STO (001). Grâce aux marches créées par la vicinalité du film qui induisent une anisotropie uniaxiale, on peut amplifier l'effet magnétostrictive en appliquant des champs magnétiques faibles parallèlement et perpendiculairement aux marches (fig. 12).

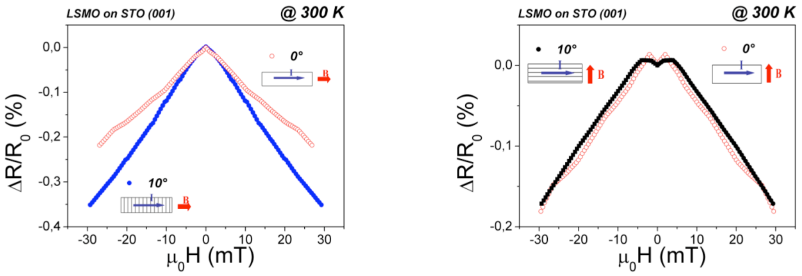

Figure 12 : MR de couches minces de LSMO déposées sur un substrat vicinaux STO (001) d’angle 10°.

Le dernier dispositif est constitué de jonctions magnétiques réalisées en créant des nanoconstrictions dans des films de LSMO déposés sur des substrats de (110). La courbe de MR obtenue est rapportée dans la figure 13.

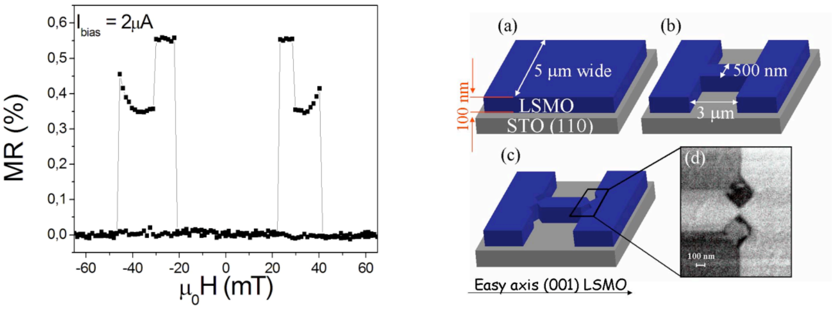

Figure 13 : MR d'un dispositif à double paroi de domaine réalisé avec des nanoconstrictions sur une couche mince de LSMO déposée sur STO (110).

Manganites à magnétorésistance colossale pour la réalisation de capteurs

Résumé: La croissance de couches minces épitaxiées de La0.7Sr0.3MnO3 a été réalisée sur différents substrats, dont SrTiO3 (001), (110), vicinal et Si. La conception de bolomètres et de dispositifs spintroniques est donc envisageable. Différentes techniques de dépôt ont été utilisées: la pulvérisation cathodique, l'ablation laser pulsée, assistée ou non par RHEED (Reflection High Energy Electron Diffraction). Les échantillons ont été caractérisés par diffraction de rayon X, en étudiant particulièrement l'épitaxie et la contrainte dans les couches. Des analyses complémentaires de RHEED, de LEED (Low Energy Electron Diffraction), et de STM/AFM (Scanning Tunneling/Atomic Force Microscopies) ont été également réalisées, ainsi que des mesures de résistivité et d'aimantation en fonction de la température. L'effet de l'orientation du substrat SrTiO3 a ainsi été montré. Trois dispositifs spintroniques utilisant une couche morte, des surfaces vicinales ou l'injection de spin sont finalement présentés.

Mots-clés: oxydes de manganese, couches minces, dépôt par ablation laser pulsé, dépôts physiques, rayons X – diffraction, magnétorésistance, microcapteurs

Colossal magnetoresistive manganites for sensing applications

Abstract: The growth of high quality epitaxial La0.7Sr0.3MnO3 thin films was controlled on various substrates, including SrTiO3 (001), (110), vicinal substrates and Si. The design and development of applications such as uncooled bolometers and spintronic devices could then be considered. In this work, different deposition techniques were used: sputtering, pulsed laser deposition, assisted or not by RHEED (Reflection High Energy Electron Diffraction). The samples were characterized by X-ray diffraction, particularly studying epitaxy and strain in the layers. Further analyzes using RHEED, LEED (Low Energy Electron Diffraction), and STM/AFM (Scanning Tunneling and Atomic Force Microscopies) were also conducted, as well as resistivity and magnetization measurements as a function of the temperature. The effect of the orientation of the SrTiO3 substrate has been demonstrated. Finally, three examples of spintronic devices based on dead layer, vicinal surfaces or spin injection are presented.

Keywords: manganese oxides, thin films, pulsed laser deposition, x-rays – diffraction, magnetoresistance

Discipline: Milieux denses, matériaux et composants

Laboratoires: GREYC-ENSICAEN (CNRS UMR 6072) – Bd. Du Maréchal Juin 14032 Caen France; LAM Università di Cassino – Via G. Di Biasio 43, 03043 Cassino (FR) Italy; CNR-INFM Coherentia Naples – Dip. Scienze Fisiche Compl. Univ. Monte Sant'Angelo Via Cintia 80126 Napoli Italy